

COMPUTATIONAL SCREENING OF MBENES AS ANODE MATERIALS
OF METAL-ION BATTERIES



LAPPAWAT NGAMWONGWAN

A Thesis Submitted in Partial Fulfillment of the Requirements for the
Degree of Doctor of Philosophy in Physics
Suranaree University of Technology
Academic Year 2025

การคัดกรองวัสดุเอ็มปิ่นด้วยวิธีการคำนวณสำหรับใช้เป็นวัสดุแอโนด
ของแบตเตอรี่ชนิดโลหะไอออน



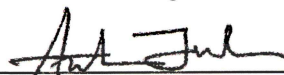
นายลาภวัต งามวงศ์วาน

วิทยานิพนธ์นี้เป็นส่วนหนึ่งของการศึกษาตามหลักสูตรปริญญาปรัชญาดุษฎีบัณฑิต
สาขาวิชาฟิสิกส์
มหาวิทยาลัยเทคโนโลยีสุรนารี
ปีการศึกษา 2568

COMPUTATIONAL SCREENING OF MBENES AS ANODE MATERIALS
OF METAL-ION BATTERIES

Suranaree University of Technology has approved this thesis submitted in partial fulfillment of the requirements for the Degree of Doctor of Philosophy.

Thesis Examining Committee



(Dr. Anchalee Junkaew)

Chairperson



(Assoc. Prof. Dr. Suwit Suthirakun)

Member (Thesis Advisor)



(Asst. Prof. Dr. Ittipon Fongkaew)

Member (Thesis Co-Advisor)



(Asst. Prof. Dr. Nongnuch Artrith)

Member (Thesis Co-Advisor)



(Assoc. Prof. Dr. Sirichok Jungthawan)

Member



(Assoc. Prof. Dr. Wittawat Saenrang)

Member



(Dr. Monchai Jitvisate)

Member


(Assoc. Prof. Dr. Yupaporn Ruksakulpiwat)

Acting Vice Rector for Academic Affairs
and Quality Assurance

(Prof. Dr. Santi Maensiri)

Acting Dean of the Institute of Science

ลาภวัต งามวงศ์วาน : การคัดกรองวัสดุเอ็มบีบีด้วยวิธีการคำนวณสำหรับใช้เป็นวัสดุแอโนด
ของแบตเตอรี่ชนิดโลหะไอออน (COMPUTATIONATIONAL SCREENING OF MBENES
AS ANODE MATERIALS OF METAL-ION BATTERIES).

อาจารย์ที่ปรึกษา : รองศาสตราจารย์ ดร.สุวิทย์ สุธีรากุล, 126 หน้า.

คำสำคัญ: แบตเตอรี่ชนิดโลหะไอออน วัสดุสองมิติ โลหะทรานซิชันโบโรด์ ทฤษฎีฟังก์ชันนอลความ
หนาแน่น โลหะทรานซิชัน

โลหะทรานซิชันโบโรด์แบบสองมิติหรือเอ็มบีบีเป็นวัสดุที่มีศักยภาพสูงสำหรับใช้เป็นแอโนด
ในแบตเตอรี่ชนิดโลหะไอออน เนื่องจากมีคุณสมบัติในการนำไฟฟ้าที่ดีและโครงสร้างที่สามารถ
ปรับแต่งได้ อย่างไรก็ตามงานวิจัยที่ผ่านมาเน้นเพียงองค์ประกอบ วัสดุภาค และโลหะไอออนบางกลุ่ม
เท่านั้น โดยขาดการเปรียบเทียบอย่างเป็นระบบและครอบคลุมกลุ่มโลหะทรานซิชันทั้งหมด งานวิจัย
นี้จึงนำเสนอการศึกษาคัดกรองเชิงคำนวณอย่างเป็นระบบของวัสดุเอ็มบีบี M_2B_2 โดย M คือโลหะ
ทรานซิชัน ภายใต้วัสดุภาค ได้แก่ ออร์โธโรมบิก เฮกซะโกนัล ไตรโกนัล และเตตระโกนัล โดยอาศัย
ทฤษฎีฟังก์ชันนอลความหนาแน่น และแบบจำลองเชิงอธิบายด้วยการเรียนรู้ของเครื่อง เพื่อวิเคราะห์
ความสัมพันธ์ระหว่างโครงสร้างกับคุณสมบัติเชิงฟิสิกส์และเคมีไฟฟ้า โดยกระบวนการคัดกรอง
เบื้องต้นซึ่งพิจารณาความเสถียรทางโครงสร้าง การเคลื่อนที่ได้เร็วของอิเล็กตรอนและโลหะไอออน
สามารถลดจำนวนวัสดุที่มีคุณสมบัติเหมาะสมไว้เพียงครึ่งหนึ่ง จากนั้นจึงประเมินคุณสมบัติเคมีไฟฟ้า
เพิ่มเติม ได้แก่ ความจุจำเพาะและแรงดันไฟฟ้าเปิดวงจร ซึ่งนำไปสู่วัสดุที่มีศักยภาพ 2 กลุ่ม ได้แก่ (1)
วัสดุออร์โธโรมบิกและเฮกซะโกนัลของ Sc, Ti และ Y ซึ่งให้ความจุสูงและแรงดันไฟต่ำ และ (2)
วัสดุไตรโกนัลและเตตระโกนัลของ V, Cr, Mn และ Fe ซึ่งแม้มีความจุต่ำกว่าเล็กน้อย แต่โลหะ
ไอออนเคลื่อนที่ได้เร็วเหมาะสำหรับการประจุไฟฟ้าเร็ว โดย Mn และ Fe ยังมีข้อได้เปรียบด้านต้นทุน
ราคาอีกด้วย นอกจากนี้ แบบจำลองเชิงอธิบายด้วยการเรียนรู้ของเครื่องยังช่วยให้เข้าใจความสัมพันธ์
ระหว่างโครงสร้างและสมบัติเชิงประสิทธิภาพได้มากขึ้น โดยเฉพาะในแง่ของพลังงานยึดเหนี่ยวและ
แรงดันไฟฟ้า ผลลัพธ์จากงานวิจัยนี้ชี้ให้เห็นถึงศักยภาพของวัสดุ M_2B_2 สำหรับการพัฒนาแอโนด
แบตเตอรี่ชนิดโลหะไอออนในอนาคต และยังนำเสนอชุดข้อมูลและชุดความเข้าใจที่มีประโยชน์ต่อ
แนวทางการออกแบบวัสดุอย่างมีหลักการ

สาขาวิชาฟิสิกส์

ปีการศึกษา 2568

ลายมือชื่อนักศึกษา ลาภวัต งามวงศ์วาน

ลายมือชื่ออาจารย์ที่ปรึกษา Dr. Suwit

ลายมือชื่ออาจารย์ที่ปรึกษาร่วม Dr. Su.

ลายมือชื่ออาจารย์ที่ปรึกษาร่วม M. A. Truth

LAPPAWAT NGAMWONGWAN : COMPUTATIONTATIONAL SCREENING OF MBENES
AS ANODE MATERIALS OF METAL-ION BATTERIES.

THESIS ADVISOR : ASSOC. PROF. SUWIT SUTHIRAKUN, Ph.D. 126 PP.

Keyword: Metal-ion batteries, 2D materials, Transition metal borides (MBenes),
Density functional theory (DFT), Transition metal

Two-dimensional transition metal borides (MBenes) have emerged as promising anode materials for metal-ion batteries due to their intrinsic conductivity and structural tunability. However, most existing studies focus on a limited set of compositions, phases, and charge carriers, lacking a systematic and comparable assessment across the full transition metal series. To address this gap, this thesis presents a comprehensive computational screening of M_2B_2 monolayers, where M spans 26 transition metals across four crystal phases, using density functional theory. A consistent computational framework, combined with interpretable machine learning, was employed to evaluate structural, electronic, and electrochemical properties. Pre-screening based on cohesive energy, phonon stability, electronic conductivity, and ion diffusion narrowed the candidate pool by half. Further electrochemical analysis identified two promising groups: (1) Sc-, Ti-, and Y-based phases with high gravimetric capacity and low open-circuit voltage (OCV); and (2) V-, Cr-, Mn-, and Fe-based phases with low diffusion barriers and moderate OCVs. Interpretable ML models were used to better understand the structure–property relationships governing cohesive energy and OCV, revealing key performance descriptors. These findings demonstrate the potential of M_2B_2 MBenes for next-generation battery anodes and provide data-driven guidelines for their rational design.

School of Physics
Academic Year 2025

Student's Signature ลพาวัต งามวงศ์วาน
Advisor's Signature Assoc. Prof. Suwit Suthirakun
Co-Advisor's Signature Dr. M. Suthirakun
Co-Advisor's Signature M. Suthirakun

ACKNOWLEDGEMENTS

I want to express my sincere gratitude to everyone who made this Ph.D. journey and thesis possible.

First and foremost, my deepest thanks go to my advisor, Assoc. Prof. Dr. Suwit Suthirakun, and my co-advisors, Asst. Prof. Dr. Ittipon Fongkaew and Asst. Prof. Dr. Nongnuch Artrith. Their continuous support, invaluable guidance, thoughtful discussions, and unwavering encouragement were absolutely essential to the success of this research. I also extend my sincere appreciation to my thesis committee members: Dr. Anchalee Junkaew, Assoc. Prof. Dr. Sirichok Jungthawan, Assoc. Prof. Dr. Wittawat Saenrang, and Dr. Monchai Jitvisate. Their expertise and feedback significantly enhanced the quality of this work.

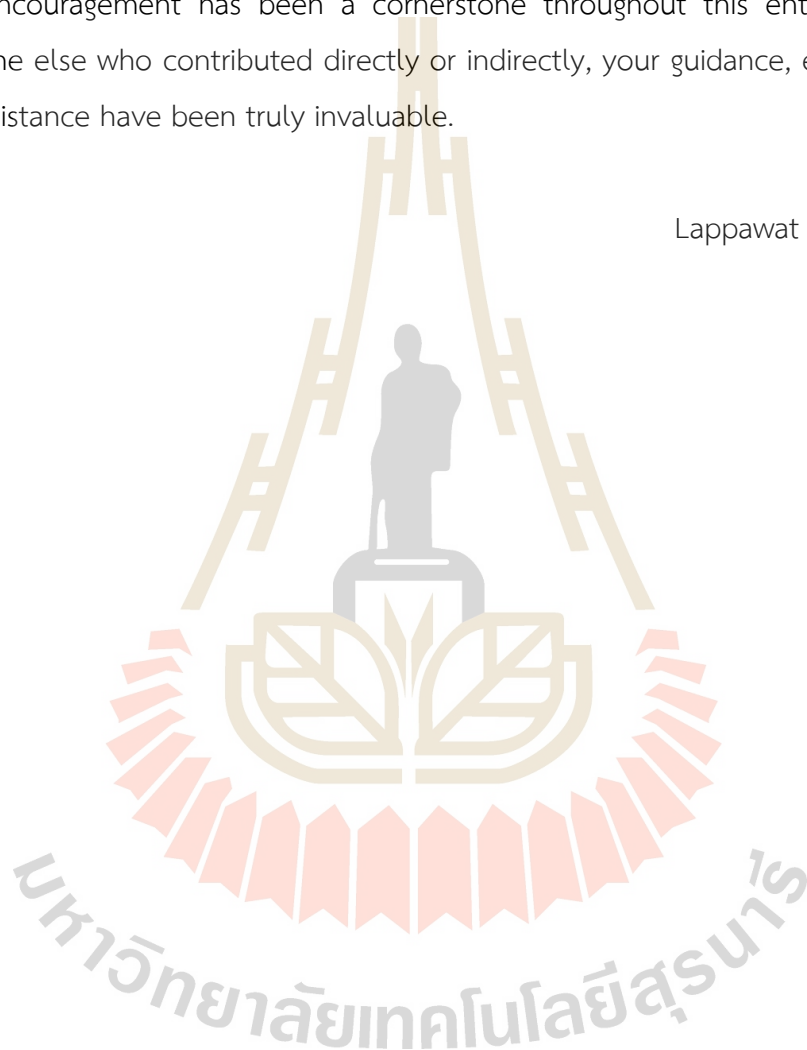
I am incredibly grateful for the financial support provided by the Development and Promotion of Science and Technology Talents Project (DPST, Thailand), which made my Ph.D. studies possible. I also appreciate the assistance from Suranaree University of Technology (SUT) for completing this research. My thanks also go to the faculty and staff of the School of Physics, Institute of Science, Suranaree University of Technology, for their consistent support and encouragement throughout my academic journey. Computational resources were vital, and I thank the NSTDA Supercomputer Center (ThaiSC), the Institute of Science, Suranaree University of Technology, and the Fugaku supercomputer at Riken Center for Computational Science for their provision.

My research visit to the Materials Chemistry and Catalysis group at the Debye Institute for Nanomaterials Science, Utrecht University, was an incredibly valuable experience. I am grateful to Asst. Prof. Nongnuch Artrith and my colleagues there (Rodrigo, Qijun, Masoud, Hendrik, and others) for this eye-opening opportunity. It significantly broadened my academic and personal horizons, providing access to High-Performance Computing (HPC) facilities and allowing me to participate in various schools and workshops focused on frontier research topics. I particularly appreciate the support from DPST, Thailand, which made this visit possible.

To my friends and colleagues, both current and former, in the Computational Materials Science and Catalysis (COMSCAT) Group namely Apinya, Bunrat, Athis, Maneerat, Sirisak, Panupol, Wongsathorn, Pariwut, Arisa, and others, thank you for your support, teamwork, and for making my academic life both productive and enjoyable.

Finally, to my family and my girlfriend, thank you for your constant support. Your encouragement has been a cornerstone throughout this entire process. To everyone else who contributed directly or indirectly, your guidance, encouragement, and assistance have been truly invaluable.

Lappawat Ngamwongwan



CONTENTS

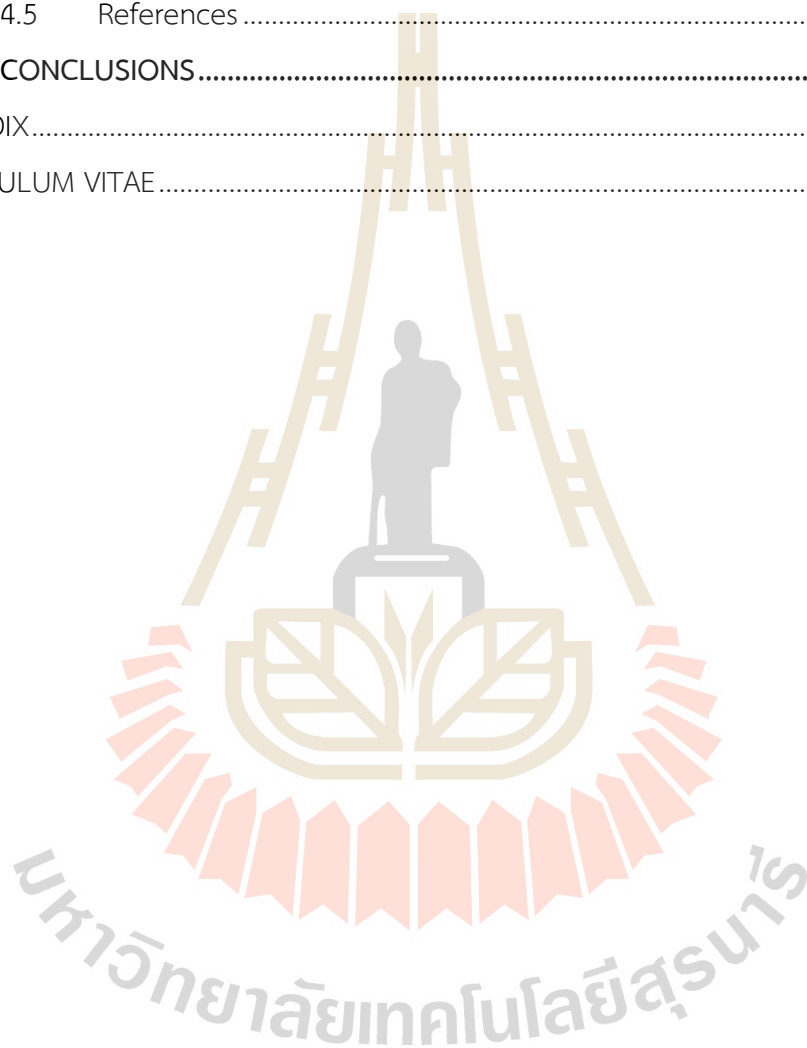
| | Page |
|---|-----------|
| ABSTRACT IN THAI..... | I |
| ABSTRACT IN ENGLISH..... | II |
| ACKNOWLEDGEMENTS | III |
| CONTENTS..... | V |
| LIST OF TABLES | VIII |
| LIST OF FIGURES | IX |
| LIST OF ABBREVIATIONS | XII |
| CHAPTER | |
| I INTRODUCTION | 1 |
| 1.1 Research background and significance | 1 |
| 1.2 Research objectives | 5 |
| 1.3 Scope and limitations..... | 5 |
| 1.4 References | 8 |
| II LITERATURE REVIEW..... | 13 |
| 2.1 Overview of metal-ion batteries | 13 |
| 2.2 Anode materials..... | 15 |
| 2.3 MBenes as emerging anode materials | 18 |
| 2.4 Computational studies on MBene anodes | 22 |
| 2.5 Summary of literature gap | 35 |
| 2.6 Reference | 37 |
| III RESEARCH METHODOLOGY | 50 |
| 3.1 Overview | 50 |
| 3.2 Density functional theory | 50 |
| 3.2.1 Many-body problems in material systems..... | 51 |
| 3.2.2 Concept of density functional theory | 51 |
| 3.2.3 Exchange-correlation energy functional..... | 53 |

CONTENTS (Continued)

| | | Page |
|-----------|--|-----------|
| | 3.2.4 Self-consistent field method..... | 53 |
| | 3.2.5 Pseudopotentials..... | 55 |
| | 3.2.6 Dispersion correction: DFT-D3..... | 56 |
| | 3.2.7 Geometry optimization..... | 58 |
| | 3.2.8 Phonon dispersion calculation..... | 60 |
| | 3.2.9 Climbing image nudged elastic band (CI-NEB) method..... | 60 |
| 3.3 | Machine learning..... | 61 |
| | 3.3.1 Regression models..... | 62 |
| | 3.3.2 Model evaluation..... | 64 |
| | 3.3.3 Model interpretation..... | 65 |
| | 3.3.4 SHAP technique..... | 67 |
| 3.4 | Research methodology..... | 69 |
| | 3.4.1 Workflow..... | 69 |
| | 3.4.2 Computational setup and model..... | 70 |
| | 3.4.3 Calculated material properties..... | 70 |
| | 3.4.4 Material features..... | 73 |
| | 3.4.5 Model construction and interpretation..... | 75 |
| 3.5 | References..... | 76 |
| IV | RESULTS AND DISCUSSION..... | 80 |
| | 4.1 Overview..... | 80 |
| | 4.2 Geometry, stability, and electronic properties of M_2B_2 | 80 |
| | 4.2.1 Crystal structure of M_2B_2 | 80 |
| | 4.2.2 Energetic stability: cohesive energy..... | 83 |
| | 4.2.3 Dynamical stability: phonon dispersion..... | 89 |
| | 4.2.4 Electronic structure..... | 91 |
| | 4.3 Electrochemical properties..... | 92 |
| | 4.3.1 Adsorption of carrier species and theoretical capacity..... | 92 |
| | 4.3.2 Open-circuit voltage (OCV)..... | 97 |

CONTENTS (Continued)

| | Page |
|---|------------|
| 4.3.3 Ionic conductivity: diffusion barriers and pathways | 107 |
| 4.4 Promising M_2B_2 anode candidates | 111 |
| 4.5 References | 115 |
| V CONCLUSIONS..... | 119 |
| APPENDIX..... | 121 |
| CURRICULUM VITAE..... | 126 |



LIST OF TABLES

| Table | Page |
|---|------|
| 2.1 Comprehensive review of computational studies on MBenes-based anode for MIBs..... | 26 |
| 3.1 The elemental and structural parameters used as features for machine learning model training..... | 74 |
| 4.1 Comparison of Li diffusion barriers (in eV) on ort- M_2B_2 from this study and literature value..... | 111 |
| 4.2 Performance comparison of selected M_2B_2 monolayers with commercial graphite and Ti_3C_2 MXene benchmark as Li-ion battery anodes..... | 115 |

LIST OF FIGURES

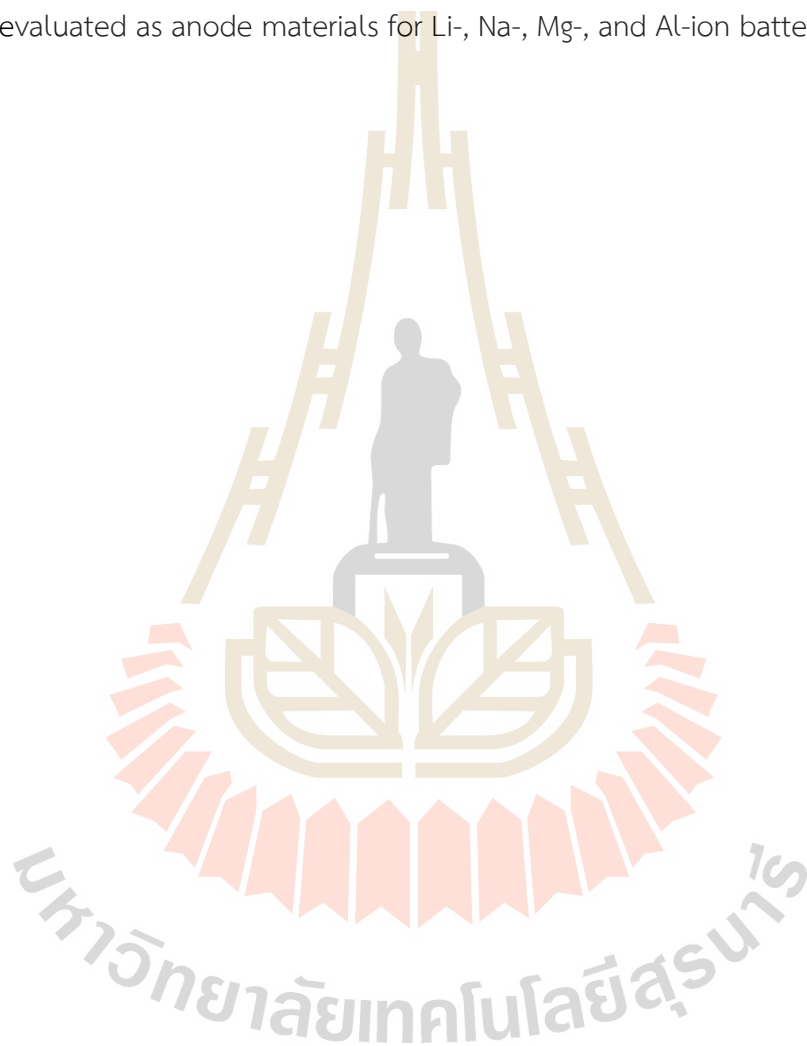
| Figure | Page |
|---|------|
| 1.1 Schematic illustration of the components and operating principles of a lithium-ion battery during (A) charging and (B) discharging..... | 2 |
| 1.2 Comparison of crystal structures between a typical MXene and various MBene phases..... | 4 |
| 1.3 Scope of the computational screening in this thesis..... | 7 |
| 2.1 Schematic illustration of the working principles of a lithium-ion battery, showing the directions of lithium-ion and electron flow during discharge (top panel) and charge (bottom panel) processes..... | 14 |
| 2.2 Possible compositions and structures of MBenes | 19 |
| 2.3 Timeline highlighting key discoveries in MBene research..... | 20 |
| 2.4 Different visualizations of previous computational studies in Table 2.1..... | 33 |
| 2.5 Computational screening of MB ₂ for lithium-ion batteries..... | 35 |
| 3.1 The scheme of self-consistent field iterations for solving the Kohn-Sham equation and obtaining total energy and other physical properties..... | 54 |
| 3.2 Schematic illustration of a real (blue) and a pseudo (red) potential and their corresponding wavefunctions. The cutoff radius r_c is the position where both values are matched..... | 56 |
| 3.3 The scheme of configuration updating iterations for geometry optimization | 59 |
| 3.4 Illustration of regression model concepts: linear regression, decision tree, random forest, and gradient boosting, each showing how models build predictions from data..... | 63 |
| 3.5 Illustration of (a) a decision tree and (b) a linear model used to predict loan approval outcomes based on applicant age and salary. Red stars indicate approved loan, while blue circles represent rejected applications | 66 |
| 4.1 Optimized crystal structures of M ₂ B ₂ MBenes in four distinct phases: orthorhombic, hexagonal, trigonal, and tetragonal..... | 81 |

LIST OF FIGURES (Continued)

| Figure | Page |
|---|------|
| 4.2 Principal component analysis (PCA) of SOAP-derived structural descriptors for M_2B_2 MBenes..... | 83 |
| 4.3 Cohesive energy per atom of M_2B_2 MBenes across 3d, 4d, and 5d transition metals (M) for different crystal phases..... | 84 |
| 4.4 Machine learning prediction and SHAP-based interpretation of cohesive energy for M_2B_2 MBenes..... | 86 |
| 4.5 Dynamical stability of M_2B_2 MBenes evaluated using phonon dispersion calculations..... | 90 |
| 4.6 Projected density of states of ort- Mo_2B_2 , representative of M_2B_2 MBenes..... | 92 |
| 4.7 Layer-by-layer adsorption of Li and Na on representative ort- Cr_2B_2 MBene and the associated consecutive adsorption energy per atom. The adsorption begins with the bare monolayer, followed by the stepwise addition of carrier atoms on both sides of the surface to form the first, second, and third adsorption layers..... | 93 |
| 4.8 Consecutive adsorption energies of Li, Na, Mg, and Al on representative ort- M_2B_2 monolayers up to three layers (1L–3L)..... | 95 |
| 4.9 Gravimetric capacity and maximum number of adsorption layers for Li, Na, Mg, and Al adsorption on M_2B_2 across different transition metals and phases. | 96 |
| 4.10 Open-circuit voltage profile of Mg adsorption on representative ort- Mo_2B_2 | 98 |
| 4.11 Open-circuit voltage values corresponding to the first layer adsorption of Li, Na, Mg, and Al on various M_2B_2 MBenes..... | 100 |
| 4.12 Distribution of open-circuit voltage values at first-layer adsorption on M_2B_2 MBenes, grouped by carrier species (A = Li, Na, Mg, Al)..... | 101 |
| 4.13 Machine learning prediction and SHAP-based interpretation of open-circuit voltage values at first-layer adsorption on various M_2B_2 | 101 |
| 4.14 Decomposed adsorption energy components for different carriers on M_2B_2 | 103 |
| 4.15 Phase dependent on lateral interaction energies of various carrier species. | 106 |

LIST OF FIGURES (Continued)

| Figure | | Page |
|--------|--|------|
| 4.16 | Diffusion barriers of Li, Na, Mg, and Al on M_2B_2 monolayers | 108 |
| 4.17 | Gravimetric capacity versus open-circuit voltage for M_2B_2 monolayers evaluated as anode materials for Li-, Na-, Mg-, and Al-ion batteries..... | 113 |



LIST OF ABBREVIATIONS

| | |
|----------|--|
| LIB | = Lithium-ion battery |
| MIB | = Metal-ion battery |
| SIB | = Sodium-ion battery |
| Li | = Lithium |
| Na | = Sodium |
| Mg | = Magnesium |
| Al | = Aluminium |
| 2D | = Two-dimensional |
| MXene | = Two-dimensional transition metal carbide/nitride |
| MBene | = Two-dimensional transition metal boride |
| M_2B_2 | = Two-dimensional transition metal boride in M_2B_2 composition |
| M | = Transition metal species in M_2B_2 |
| ort | = Orthorhombic (crystal phase) |
| hex | = Hexagonal (crystal phase) |
| tri | = Trigonal (crystal phase) |
| tetr | = Tetragonal (crystal phase) |
| P | = Crystal phases of M_2B_2 |
| A | = Carrier species such as Li, Na, Mg, and Al |
| 0L | = bare M_2B_2 monolayer (no adsorption of carrier species) |
| 1L | = First layer adsorption of carrier species on M_2B_2 monolayer |
| 2L | = Second layer adsorption of carrier species on M_2B_2 monolayer |
| 3L | = Third layer adsorption of carrier species on M_2B_2 monolayer |
| DFT | = Density Functional Theory |
| vdW | = Van der Waals |
| PBE | = Perdew-Burke-Ernzerhof (exchange-correlation functional) |
| GGA | = Generalized Gradient Approximation |
| SCF | = Self-consistent field |

LIST OF ABBREVIATIONS (Continued)

| | |
|------------|---------------------------------------|
| VASP | = Vienna Ab initio Simulation Package |
| NEB | = Nudged Elastic Band |
| CI-NEB | = Climbing Image Nudged Elastic Band |
| DOS | = Density of states |
| PDOS | = Projected density of states |
| SOAP | = Smooth Overlap of Atomic Positions |
| ML | = Machine learning |
| LR | = Linear regression |
| DT | = Decision tree |
| RF | = Random forest |
| GB | = Gradient boosting |
| XG/XGBoost | = Extreme gradient boosting |
| PCA | = Principal Component Analysis |
| MAE | = Mean Absolute Error |
| RMSE | = Root Mean Square Error |
| R^2 | = Coefficient of determination |
| SHAP | = SHapley Additive exPlanations |
| OCV | = Open-circuit voltage |

CHAPTER I

INTRODUCTION

1.1 Research background and significance

Energy storage has become increasingly important due to the rising demand for portable electronic devices, electric vehicles, and the growing use of renewable energy sources such as solar and wind, which require storage systems to manage their intermittent supply. To support these needs, battery technology must be efficient, high-performing, and cost-effective, making them a key part of technological progress across many industries (Ding et al., 2019; dos Reis et al., 2021). Among various battery types, lithium-ion batteries (LIBs) have become the most widely used because of their high energy density and well-developed technology. LIBs are currently the most advanced option and come closest to meeting global requirements for energy density, power output, and lifespan, although further improvements are still needed (Aricò et al., 2005; Armand and Tarascon, 2008; Cheng et al., 2021; Dubal et al., 2015; Niu et al., 2024; Tarascon and Armand, 2001; Weiss et al., 2021).

The working principle of LIBs involves the reversible movement of Li-ions between the anode and cathode during charge and discharge cycles, as illustrated in **Figure 1.1**. While Li-ions migrate through the electrolyte and separator, electrons flow through an external circuit to power devices. These processes are driven by redox reactions at both electrodes (Goodenough and Park, 2013). The effectiveness of this process, and performance of LIBs, depends largely on the electrode materials, especially the anode. An ideal anode should offer high Li-ion capacity, fast Li-ions and electrons transport, structural stability over repeated charge–discharge cycles, and chemical compatibility with the electrolyte. In addition, the anode's electrochemical potential strongly influences the overall cell voltage and energy density of the battery (Landi et al., 2009). Therefore, optimizing anode materials remains crucial for advancing the performance and cost-effectiveness of next-generation LIBs.

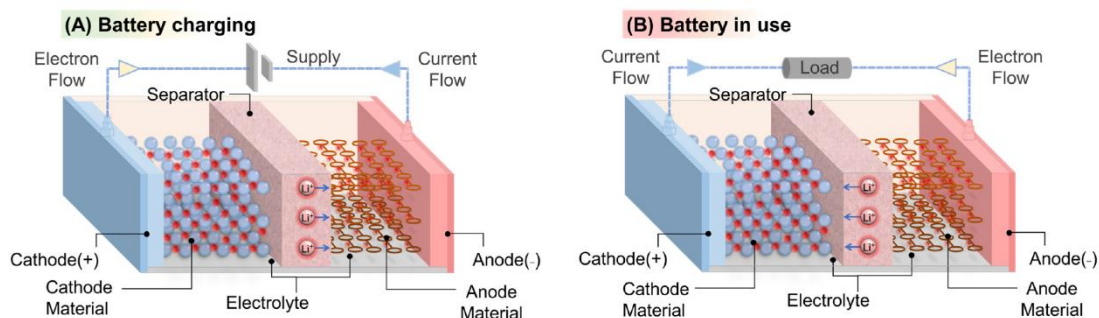


Figure 1.1 Schematic illustration of the components and operating principles of a lithium-ion battery during (A) charging and (B) discharging (Menye et al., 2025).

Despite continuous advancement over the past several decades, commercial LIBs still face inherent limitations. Graphite is widely used as the standard anode material in current LIBs due to its excellent electrical conductivity, structural stability, and low cost (Dahn et al., 1995; Endo et al., 2000). However, its relatively low theoretical capacity of 372 mAh/g and sluggish Li-ion intercalation kinetics hinder fast-charging performance and limit rate capability (Armand and Tarascon, 2008). Beyond LIBs, alternative metal-ion batteries (MIBs) using carrier species such as Na, Mg, Al, or Ca have attracted growing attention due to concerns over the rising cost and uneven distribution of lithium resources (Delmas, 2018; F. Liu et al., 2021; Taylor, 1964). These systems also offer potential advantages in energy density, for example, Mg-ion batteries, as the Mg-ion can transfer two electrons per ion, enabling higher charge storage compared to monovalent ions. However, graphite is generally incompatible with these ions due to poor intercalation behavior, resulting from size mismatch and strong electrostatic interactions (DiVincenzo and Mele, 1985). These challenges highlight the urgent need for new anode materials that combine high capacity, fast ion transport, structural stability, and compatibility with a broader range of carrier species to support the development of next-generation, high-performance, and cost-effective batteries.

Two-dimensional (2D) materials have garnered significant attention as promising anode materials for MIBs due to their high surface area, short ion diffusion paths, and excellent electronic conductivity (Bahari et al., 2021). Examples include graphene and its derivatives (Kucinskis et al., 2013; Liang and Zhi, 2009; Ling and Mizuno, 2014), borophene (Jiang et al., 2016; Zhang et al., 2016), transition metal dichalcogenides

(Hwang et al., 2011; Jing et al., 2013; Yang et al., 2015), and transition metal carbides/nitrides known as MXenes (Ghidiu et al., 2014; Tang et al., 2012; Xie et al., 2014; D. Xiong et al., 2018). Among these, MXenes stand out due to their metallic conductivity, high ion mobility, suitable operating voltage, and tunable composition and surface chemistry (Tang et al., 2012). MXenes are one of the few 2D materials that have been both synthesized and tested as anodes in LIB systems (Aghamohammadi and Khazaeli, 2024; Chy et al., 2024; D. Xiong et al., 2018). Their layered structure and tunable surface chemistry also make them suitable for alternative metal-ion systems like Mg-ion batteries (Zhao et al., 2019). These advantages, along with their ability to form stable composites, contribute to their strong electrochemical performance.

A newly emerging class of 2D materials known as MBenes has attracted attention as promising candidates. MBenes share a similar concept with MXenes as 2D layered transition metal compounds, but are composed of metal borides instead of carbides or nitrides (Bandaru et al., 2023; Guo et al., 2017). The substitution of lighter boron atoms in place of carbon or nitrogen is expected to provide higher theoretical capacities due to a lower atomic weight. The unique bonding nature of boron enables MBenes to form a wide range of complex crystal structures, often more diverse than MXenes (Braunschweig and Colling, 2001; Sun et al., 2017) **Figure 1.2** illustrates the structural comparison between a representative hexagonal MXene (M_3C_2) and MBenes (M_2B_2) across different crystal phases, highlighting the structural diversity of MBenes (Bo et al., 2018, 2019; Guo et al., 2017; Tang et al., 2012). In addition, experimental studies have reported encouraging performance for Mo_2B_2 MBene, showing good Li storage capacity and cycling stability, in some cases outperforming MXenes (Miao et al., 2023; W. Xiong et al., 2022). However, experimental studies on MBenes remain limited, primarily due to challenges in synthesis and scalable production of these materials.

To accelerate the discovery and support experimental research on MBenes, Density Function Theory (DFT) has become an indispensable tool for predicting material properties at the quantum mechanical level. It offers fast and reliable estimates of anode properties, including structural stability, electronic structure, storage capacity, open-circuit voltage, and ion diffusion barrier (Bahari et al., 2021). At the initial stage of computational research on MBenes, orthorhombic Mo_2B_2 and Fe_2B_2

(Guo et al., 2017) and hexagonal Ti_2B_2 (Bo et al., 2018), were suggested as promising candidates for MIB anodes due to their favorable calculated properties. Subsequent computational screening of hexagonal M_2B_2 compounds ($\text{M} = 3\text{d}$ and 4d transition metals), suggested that hexagonal Sc_2B_2 possesses favorable anode characteristics, including high capacity, low reaction voltage, and good electronic conductivity (He et al., 2021). In addition to orthorhombic and hexagonal M_2B_2 , many computational studies have investigated other MBene compositions and phases—including M_2B , MB_2 , MB_3 , MB_4 , and MB_6 —demonstrating a wide range of structural and electronic properties with potential for MIB applications (more details in Section 2.4).

Despite over 40 computational studies in the past eight years, most research has focused on individual compositions without establishing clear trends or generalizable structure-properties relationships. Moreover, variations in computational setups, such as differences in functionals, supercell size, and adsorption models, introduce inconsistencies that can make direct comparisons across studies challenging and often unreliable. As a result, it remains challenging to build a unified understanding of MBene behavior across different compositions and crystal phases. There is a need for systematic screening using consistent computational setups. A homogenous database would allow fair comparison across compositions and phases, while also support the development of statistical models to reveal key structure-property trends.

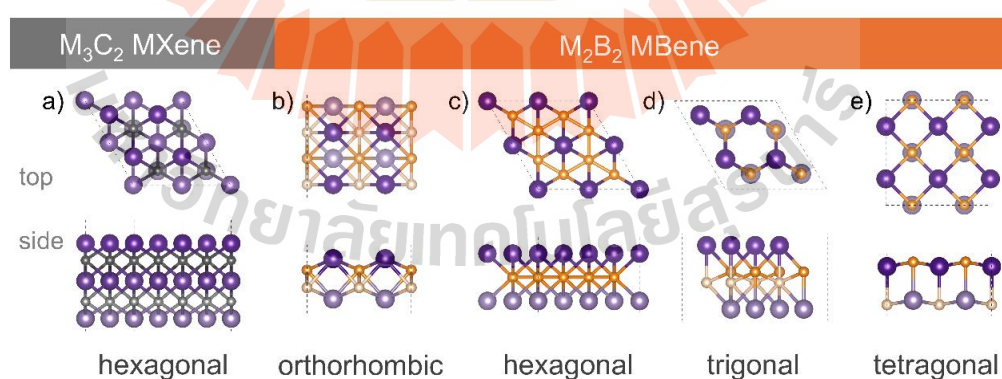


Figure 1.2 Comparison of crystal structures between a typical MXene and various MBene phases. a) M_3C_2 MXene in hexagonal phase (Tang et al., 2012). b-e) M_2B_2 MBenes in orthorhombic, hexagonal, trigonal, and tetragonal phases (Bo et al., 2018, 2019; Guo et al., 2017). Transition metal (M), boron (B), and carbon (C) atoms are shown in purple, orange, and gray, respectively. Slight color shading is used to enhance visual clarity.

To address these challenges, this study systematically screens a wide range of MBenes with the M_2B_2 composition as potential anode materials for MIBs. Transition metals from the 3d, 4d, and 5d series are considered across four crystal phases. By applying a consistent DFT-based workflow, the study evaluates structural and electrochemical properties. These results are used to suggest promising MBene candidates for storing carrier species ions and to develop a structure–property model that can support the rational design of next-generation MBene-based anodes. The specific objectives and scope are described in the following sections.

1.2 Research objectives

- I. To systematically screen M_2B_2 MBenes with varied compositions and crystal phases as potential anode materials for metal-ion batteries using DFT, and to suggest promising candidates based on their predicted anode properties.
- II. To develop statistical or machine learning models for better understanding some material-property relationship and identifying the important descriptors from the computed dataset.

1.3 Scope and limitations

This thesis focuses on the computational screening of MBene materials with the M_2B_2 chemical composition, where M represents a transition metal from the 3d (Sc, Ti, V, Cr, Mn, Fe, Co, Ni, Cu), 4d (i.e., Y, Zr, Nb, Mo, Tc, Ru, Rh, Pd, Ag), or 5d (i.e., Hf, Ta, W, Re, Os, Ir, Pt, Au) series. M_2B_2 is selected as the representative system due to its frequent appearance in literature and demonstrated feasibility of synthesis. For each selected element, four different crystal phases (orthorhombic, hexagonal, trigonal, and tetragonal) are explored based on Mo_2B_2 prototype structure.

The anode performance of these M_2B_2 MBenes is evaluated for four carrier species namely Li, Na, Mg and Al. Two broad categories of properties are assessed. The first includes fundamental material characteristics such as structural stability evaluated through cohesive energy and phonon band structure (to confirm the absence of imaginary frequencies) and electronic conductivity, determined by the presence or

absence of an electronic band gap. The second category comprises properties associated with metal-ion interaction: theoretical capacity is estimated by incrementally adsorbing up to three layers of ions on both top and bottom sides of the monolayer; open-circuit voltage (OCV) is calculated using the average voltage of the first adsorption layer; and ion diffusion is analyzed using the climbing image nudged elastic band (CI-NEB) method to identify energy barriers for ion migration between adjacent adsorption sites. These descriptors provide a reliable and computationally efficient framework for comparing and screening M_2B_2 MBenes.

All calculations are carried out using Density Functional Theory (DFT) as implemented in the Vienna Ab initio Simulation Package (VASP) (Kresse and Furthmüller, 1996a, 1996b; Kresse and Hafner, 1993). The modellings employ a plane-wave basis set along with projector augmented-wave (PAW) pseudopotentials (Blöchl, 1994; Kresse and Joubert, 1999). The exchange–correlation energy is treated using the Perdew–Burke–Ernzerhof (PBE) functional within the generalized gradient approximation (GGA) (Perdew et al., 1996). Standard parameters settings are applied, with further computational details provided in section 3.4.2.

This thesis has two primary limitations. First, the storage of carrier species is modeled using a surface adsorption mechanism on monolayer M_2B_2 structures. Although intercalation between layers could occur in multilayer systems, it is not considered here due to the focus on single-layer MBenes. Additionally, it is assumed that adsorption of carrier species does not alter the lattice parameters of the M_2B_2 monolayer during relaxation. Second, all calculations are conducted under vacuum conditions, meaning that potential interactions between the electrode material and the electrolyte (solvent) are neglected. These simplifications may limit the accuracy of predicted performance metrics when compared to real-world battery conditions, where factors such as multilayer intercalation and electrolyte interactions can significantly influence material behavior.

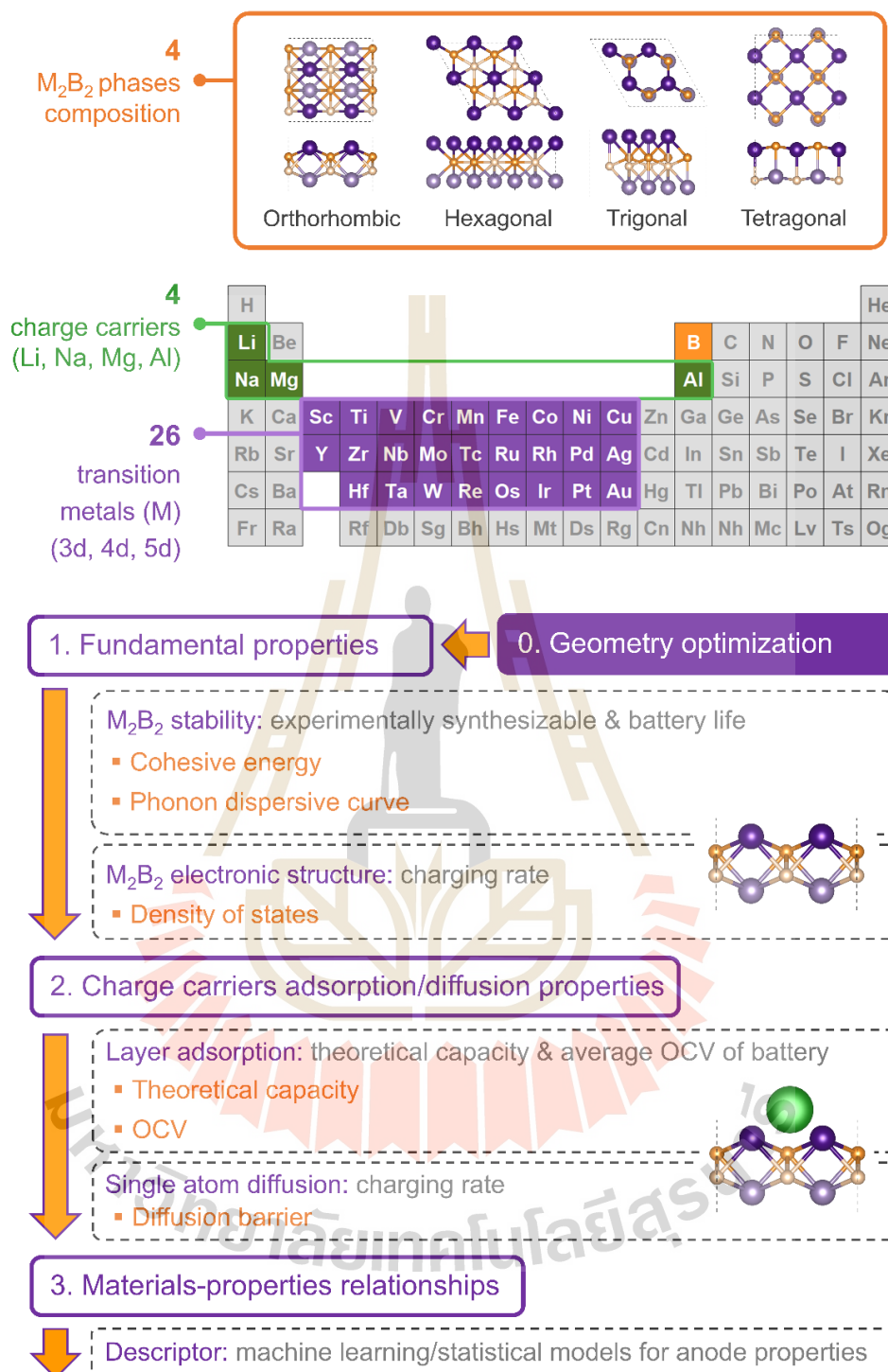


Figure 1.3 Scope of the computational screening in this thesis.

1.4 References

- Aghamohammadi, H., and Khazaeli, A. (2024). Recent advances in the development of the MXenes/Ti-based nanocomposite anode materials for Li-ion batteries: A review study. *Journal of Energy Storage*, *101*, 113851.
- Aricò, A. S., Bruce, P., Scrosati, B., Tarascon, J.-M., and van Schalkwijk, W. (2005). Nanostructured materials for advanced energy conversion and storage devices. *Nature Materials*, *4*(5), 366–377.
- Armand, M., and Tarascon, J.-M. (2008). Building better batteries. *Nature*, *451*(7179), 652–657.
- Bahari, Y., Mortazavi, B., Rajabpour, A., Zhuang, X., and Rabczuk, T. (2021). Application of two-dimensional materials as anodes for rechargeable metal-ion batteries: A comprehensive perspective from density functional theory simulations. *Energy Storage Materials*, *35*, 203–282.
- Bandaru, S., Jastrzebska, A. M., and Birowska, M. (2023). Recent progress in thermoelectric MXene-based structures versus other 2D materials. *Applied Materials Today*, *34*, 101902.
- Blöchl, P. E. (1994). Projector augmented-wave method. *Physical Review B*, *50*(24), 17953–17979.
- Bo, T., Liu, P.-F., Xu, J., Zhang, J., Chen, Y., Eriksson, O., Wang, F., and Wang, B.-T. (2018). Hexagonal Ti₂B₂ monolayer: a promising anode material offering high rate capability for Li-ion and Na-ion batteries. *Physical Chemistry Chemical Physics*, *20*(34), Article 34.
- Bo, T., Liu, P.-F., Zhang, J., Wang, F., and Wang, B.-T. (2019). Tetragonal and trigonal Mo₂B₂ monolayers: two new low-dimensional materials for Li-ion and Na-ion batteries. *Physical Chemistry Chemical Physics*, *21*(9), Article 9.
- Braunschweig, H., and Colling, M. (2001). Transition metal complexes of boron — synthesis, structure and reactivity. *Coordination Chemistry Reviews*, *223*(1), 1–51.
- Cheng, H., Shapter, J. G., Li, Y., and Gao, G. (2021). Recent progress of advanced anode materials of lithium-ion batteries. *Journal of Energy Chemistry*, *57*, 451–468.

- Chy, M. N. U., Rahman, M. A., Kim, J.-H., Barua, N., and Dujana, W. A. (2024). MXene as Promising Anode Material for High-Performance Lithium-Ion Batteries: A Comprehensive Review. *Nanomaterials*, 14(7), Article 7.
- Dahn, J. R., Zheng, T., Liu, Y., and Xue, J. S. (1995). Mechanisms for Lithium Insertion in Carbonaceous Materials. *Science*, 270(5236), 590–593.
- Delmas, C. (2018). Sodium and Sodium-Ion Batteries: 50 Years of Research. *Advanced Energy Materials*, 8(17), 1703137.
- Ding, Y., Cano, Z. P., Yu, A., Lu, J., and Chen, Z. (2019). Automotive Li-Ion Batteries: Current Status and Future Perspectives. *Electrochemical Energy Reviews*, 2(1), 1–28.
- DiVincenzo, D. P., and Mele, E. J. (1985). Cohesion and structure in stage-1 graphite intercalation compounds. *Physical Review B*, 32(4), 2538–2553.
- dos Reis, G., Strange, C., Yadav, M., and Li, S. (2021). Lithium-ion battery data and where to find it. *Energy and AI*, 5, 100081.
- Dubal, D. P., Ayyad, O., Ruiz, V., and Gómez-Romero, P. (2015). Hybrid energy storage: the merging of battery and supercapacitor chemistries. *Chemical Society Reviews*, 44(7), 1777–1790.
- Endo, M., Kim, C., Nishimura, K., Fujino, T., and Miyashita, K. (2000). Recent development of carbon materials for Li ion batteries. *Carbon*, 38(2), 183–197.
- Ghidiu, M., Lukatskaya, M. R., Zhao, M.-Q., Gogotsi, Y., and Barsoum, M. W. (2014). Conductive two-dimensional titanium carbide ‘clay’ with high volumetric capacitance. *Nature*, 516(7529), 78–81.
- Goodenough, J. B., and Park, K.-S. (2013). The Li-Ion Rechargeable Battery: A Perspective. *Journal of the American Chemical Society*, 135(4), Article 4.
- Guo, Z., Zhou, J., and Sun, Z. (2017). New two-dimensional transition metal borides for Li ion batteries and electrocatalysis. *Journal of Materials Chemistry A*, 5(45), Article 45.
- He, Q., Li, Z., Xiao, W., Zhang, C., and Zhao, Y. (2021). Computational investigation of 2D 3d/4d hexagonal transition metal borides for metal-ion batteries. *Electrochimica Acta*, 384, 138404.

- Hwang, H., Kim, H., and Cho, J. (2011). MoS₂ Nanoplates Consisting of Disordered Graphene-like Layers for High Rate Lithium Battery Anode Materials. *Nano Letters*, 11(11), 4826–4830.
- Jiang, H. R., Lu, Z., Wu, M. C., Ciucci, F., and Zhao, T. S. (2016). Borophene: A promising anode material offering high specific capacity and high rate capability for lithium-ion batteries. *Nano Energy*, 23, 97–104.
- Jing, Y., Zhou, Z., Cabrera, C. R., and Chen, Z. (2013). Metallic VS₂ Monolayer: A Promising 2D Anode Material for Lithium Ion Batteries. *The Journal of Physical Chemistry C*, 117(48), 25409–25413.
- Kim, D. J., Yoo, D.-J., Otley, M. T., Prokofjevs, A., Pezzato, C., Owczarek, M., Lee, S. J., Choi, J. W., and Stoddart, J. F. (2019). Rechargeable aluminium organic batteries. *Nature Energy*, 4(1), 51–59.
- Kresse, G., and Furthmüller, J. (1996a). Efficiency of ab-initio total energy calculations for metals and semiconductors using a plane-wave basis set. *Computational Materials Science*, 6(1), 15–50.
- Kresse, G., and Furthmüller, J. (1996b). Efficient iterative schemes for ab initio total-energy calculations using a plane-wave basis set. *Physical Review B*, 54(16), 11169–11186.
- Kresse, G., and Hafner, J. (1993). Ab initio molecular dynamics for liquid metals. *Physical Review B*, 47(1), 558–561.
- Kresse, G., and Joubert, D. (1999). From ultrasoft pseudopotentials to the projector augmented-wave method. *Physical Review B*, 59(3), 1758–1775.
- Kucinskis, G., Bajars, G., and Kleperis, J. (2013). Graphene in lithium ion battery cathode materials: A review. *Journal of Power Sources*, 240, 66–79.
- Landi, B. J., Ganter, M. J., Cress, C. D., DiLeo, R. A., and Raffaele, R. P. (2009). Carbon nanotubes for lithium ion batteries. *Energy & Environmental Science*, 2(6), 638–654.
- Li, H., Wang, Z., Chen, L., and Huang, X. (2009). Research on Advanced Materials for Li-ion Batteries. *Advanced Materials*, 21(45), 4593–4607.
- Liang, M., and Zhi, L. (2009). Graphene-based electrode materials for rechargeable lithium batteries. *Journal of Materials Chemistry*, 19(33), 5871–5878.

- Ling, C., and Mizuno, F. (2014). Boron-doped graphene as a promising anode for Na-ion batteries. *Physical Chemistry Chemical Physics*, 16(22), 10419–10424.
- Liu, F., Wang, T., Liu, X., and Fan, L.-Z. (2021). Challenges and Recent Progress on Key Materials for Rechargeable Magnesium Batteries. *Advanced Energy Materials*, 11(2), 2000787.
- Menye, J. S., Camara, M.-B., and Dakyo, B. (2025). Lithium Battery Degradation and Failure Mechanisms: A State-of-the-Art Review. *Energies*, 18(2), Article 2.
- Miao, N., Gong, Y., Zhang, H., Shen, Q., Yang, R., Zhou, J., Hosono, H., and Wang, J. (2023). Discovery of Two-dimensional Hexagonal MBene HfBO and Exploration on its Potential for Lithium-Ion Storage. *Angewandte Chemie International Edition*, 62(36), e202308436.
- Niu, H., Zhang, N., Lu, Y., Zhang, Z., Li, M., Liu, J., Zhang, N., Song, W., Zhao, Y., and Miao, Z. (2024). Strategies toward the development of high-energy-density lithium batteries. *Journal of Energy Storage*, 88, 111666.
- Perdew, J. P., Burke, K., and Ernzerhof, M. (1996). Generalized Gradient Approximation Made Simple. *Physical Review Letters*, 77(18), 3865–3868.
- Sun, X., Liu, X., Yin, J., Yu, J., Li, Y., Hang, Y., Zhou, X., Yu, M., Li, J., Tai, G., and Guo, W. (2017). Two-Dimensional Boron Crystals: Structural Stability, Tunable Properties, Fabrications and Applications. *Advanced Functional Materials*, 27(19), 1603300.
- Tang, Q., Zhou, Z., and Shen, P. (2012). Are MXenes Promising Anode Materials for Li Ion Batteries? Computational Studies on Electronic Properties and Li Storage Capability of Ti₃C₂ and Ti₃C₂X₂ (X = F, OH) Monolayer. *Journal of the American Chemical Society*, 134(40), 16909–16916.
- Tarascon, J.-M., and Armand, M. (2001). Issues and challenges facing rechargeable lithium batteries. *Nature*, 414(6861), 359–367.
- Taylor, S. R. (1964). Abundance of chemical elements in the continental crust: a new table. *Geochimica et Cosmochimica Acta*, 28(8), 1273–1285.
- Weiss, M., Ruess, R., Kasnatscheew, J., Levartovsky, Y., Levy, N. R., Minnmann, P., Stolz, L., Waldmann, T., Wohlfahrt-Mehrens, M., Aurbach, D., Winter, M., Ein-Eli, Y., and Janek, J. (2021). Fast Charging of Lithium-Ion Batteries: A Review of Materials Aspects. *Advanced Energy Materials*, 11(33), 2101126.

- Xie, Y., Naguib, M., Mochalin, V. N., Barsoum, M. W., Gogotsi, Y., Yu, X., Nam, K.-W., Yang, X.-Q., Kolesnikov, A. I., and Kent, P. R. C. (2014). Role of Surface Structure on Li-Ion Energy Storage Capacity of Two-Dimensional Transition-Metal Carbides. *Journal of the American Chemical Society*, 136(17), 6385–6394.
- Xiong, D., Li, X., Bai, Z., and Lu, S. (2018). Recent Advances in Layered Ti₃C₂T_x MXene for Electrochemical Energy Storage. *Small*, 14(17), 1703419.
- Xiong, W., Feng, X., Xiao, Y., Huang, T., Li, X., Huang, Z., Ye, S., Li, Y., Ren, X., Wang, X., Ouyang, X., Zhang, Q., and Liu, J. (2022). Fluorine-free prepared two-dimensional molybdenum boride (MBene) as a promising anode for lithium-ion batteries with superior electrochemical performance. *Chemical Engineering Journal*, 446, 137466.
- Yang, E., Ji, H., and Jung, Y. (2015). Two-Dimensional Transition Metal Dichalcogenide Monolayers as Promising Sodium Ion Battery Anodes. *The Journal of Physical Chemistry C*, 119(47), 26374–26380.
- Zhang, Y., Wu, Z.-F., Gao, P.-F., Zhang, S.-L., and Wen, Y.-H. (2016). Could Borophene Be Used as a Promising Anode Material for High-Performance Lithium Ion Battery? *ACS Applied Materials & Interfaces*, 8(34), 22175–22181.
- Zhao, M.-Q., Ren, C. E., Alhabeab, M., Anasori, B., Barsoum, M. W., and Gogotsi, Y. (2019). Magnesium-Ion Storage Capability of MXenes. *ACS Applied Energy Materials*, 2(2), 1572–1578.

CHAPTER II

LITERATURE REVIEW

2.1 Overview of metal-ion batteries

Metal-ion batteries (MIBs) encompass a broad category of rechargeable batteries that store and deliver energy through the reversible transport of metal carriers between two electrodes. Among them, lithium-ion batteries (LIBs) represent the most established and commercially mature system. A conventional LIB comprises four essential components: anode, cathode, electrolyte, and separator (see **Figure 2.1**). The cathode typically consists of Li-based transition metal compounds, such as lithium cobalt oxide (LiCoO_2), which acts as a Li source. The anode is commonly graphite, serving as the host material for Li-ions during charging. The electrolyte comprises Li salt dissolved in an organic solvent, enabling ion conduction between the electrodes. A porous polymer separator electrically isolates the electrodes while allowing ion conduction, thereby preventing short circuits and ensuring battery safety.

The operation of LIBs governed by interconversion of chemical and electrical energy through redox reactions occurring at the electrodes during the charge and discharge processes (Deng, 2015). Upon charging, Li-ions (Li^+) are extracted from the cathode (e.g., LiCoO_2) and inserted into the anode host (typically graphite), where they are stored as Li_xC_6 . This process is driven by an externally applied potential, which forces electrons to flow from the cathode to the anode through external circuit, while Li^+ migrates through the electrolyte across the separator to maintain charge neutrality. When the battery is discharged, such as when powering an electronic device, the stored Li^+ are released from the anode and travel back through the electrolyte toward cathode, propelled by the electrochemical potential difference between the electrodes. Simultaneously, electrons flow from the anode to the cathode through the external circuit, performing useful electrical work. This coupling of ionic and electronic motion enables continuous current generation until the electrochemical potentials of the electrodes equalize. The process is reversible: applying a charging

voltage once again drives Li^+ ions back into the anode and restores the battery to its high-energy state. The fundamental half-cell reactions at each electrode are as follows (Goodenough and Park, 2013):



While charging, both reactions proceed from left to right: Li^+ are extracted from LiCoO_2 and intercalated into graphite. During discharging, the reactions proceed from right to left: Li^+ de-intercalate from graphite and return to the LiCoO_2 structure. The overall cell voltage arises from the difference in redox potential between the cathode and anode reactions, which defines the energy storage and delivery mechanism of LIBs.

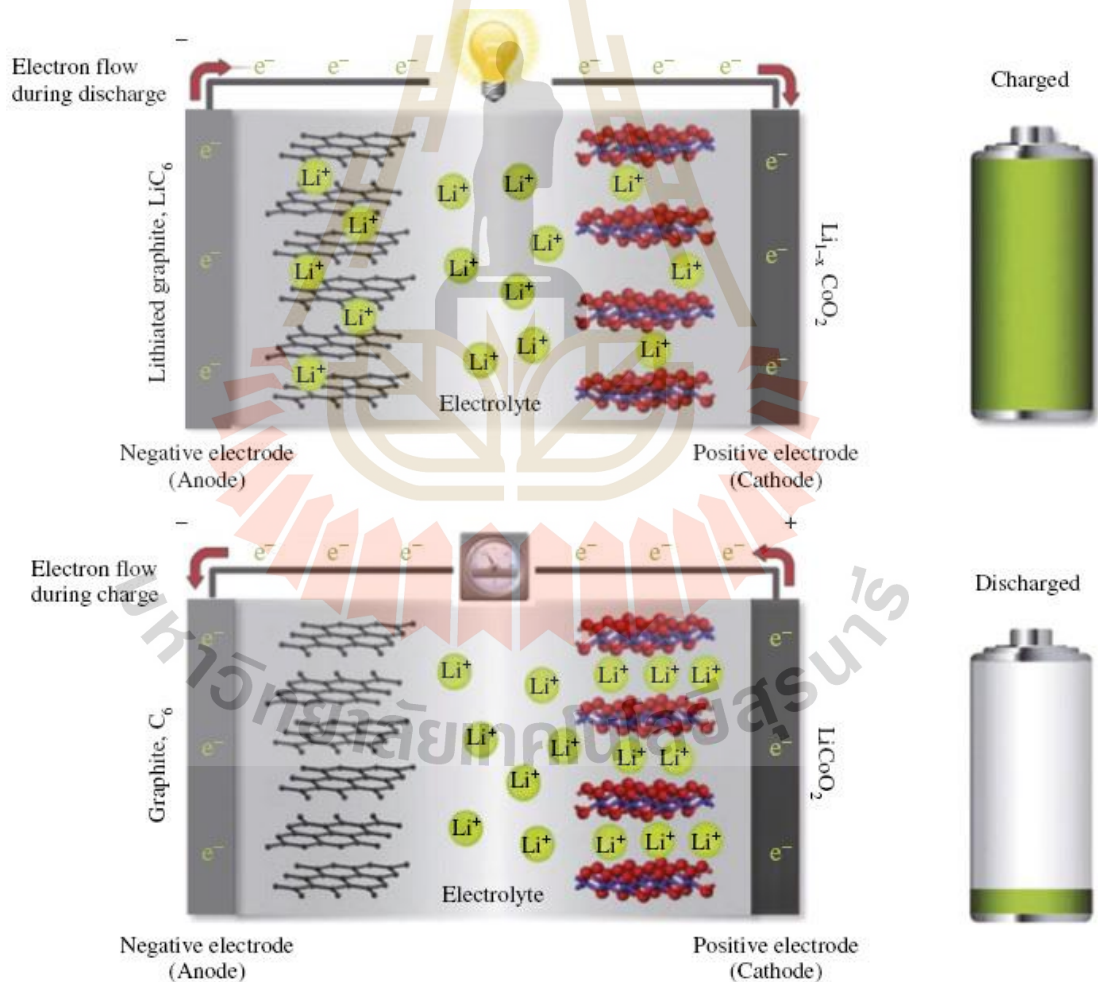


Figure 2.1 Schematic illustration of the working principles of a lithium-ion battery, showing the directions of lithium-ion and electron flow during discharge (top panel) and charge (bottom panel) processes (Michael M. Thackeray et al., 2012).

As the demand for LIBs continues to grow, especially in electric vehicles and renewable energy storage, it is expected that current LIB technology will soon reach its energy density limit and may no longer be able to meet future needs (Berg et al., 2015). Another important issue is the limited amount and uneven distribution of lithium resources in the world. This can lead to higher prices and possible shortages as more batteries are needed (Delmas, 2018; F. Liu et al., 2021; Taylor, 1964). Because of these problems, researchers are looking for new types of batteries that are more sustainable and affordable.

One important direction is the development of alternative MIBs. These batteries work in a similar way to LIBs, using the movement of metal ions between the anode and cathode during charging and discharging. However, instead of Li^+ , they use other metal ions, such as Na^+ , Mg^{2+} , or Al^{3+} , which are more widely available and cheaper. For example, sodium-ion batteries (SIBs) are seen as good options for large-scale energy storage, such as power grids, because Na is much more common and less expensive than Li. They also have good performance and a long cycle life (Chayambuka et al., 2020; Yabuuchi et al., 2014). In addition, SIBs also have similar electrochemical properties and can share the same manufacturing processes and protocols as LIBs, which is beneficial for commercialization (Chayambuka et al., 2020). Other types of MIBs use multivalent ions, like Mg^{2+} or Al^{3+} . These ions can carry more than one electron, which means they could store more energy in the same space (Canepa et al., 2017; Guo et al., 2020; Jayaprakash et al., 2011). The lower reactivity of Mg and Al and their compatibility with non-flammable aqueous electrolytes also make these batteries much safer than Li-based ones (Matsui, 2011; F. Wang et al., 2017).

These alternative MIBs hold the promise of overcoming some of the limitations of LIBs, thereby playing a crucial role in the future of energy storage technologies. However, substantial research and development efforts are still required to address their respective challenges and bring these technologies to commercial viability.

2.2 Anode materials

Anode materials play a crucial role in the operation of MIBs by serving as the host for metal-ion intercalation and de-intercalation during charge and discharge

cycles. Their properties significantly influence key battery performance, alongside cathode materials and electrolytes. To be effective, an anode material must meet several important criteria: 1) **high reversible capacity** to store a large number of metal ions in a limited weight and space; 2) **fast ionic and electronic conductivity** to support rapid fast charging and deliver high power density during discharging; 3) **high structural stability** over multiple charge and discharge cycles to ensure that the framework remains unchanged and prolongs battery lifespan; 4) **suitable operating potential** that not only contributes to a high overall cell voltage, which is determined by the difference between the cathode and anode potentials but also falls within the stable voltage window of the electrolyte. Typically, operating potential of 0–1 V is favorable for maximizing cell voltage and enhancing energy density for LIBs. It also helps reduce safety risks by lowering the potential for electrolyte decomposition and dendrite formation during cycling; and 5) **cost-effectiveness and environmental safety** to ensure sustainable large-scale application (Xu et al., 2023). Therefore, optimizing electrode materials is imperative for developing high-performance and cost-effective batteries.

The ideal anode material for MIBs is metal itself, since it offers the highest theoretical capacity and lowest reduction potential. For example, metallic Li delivers extremely high theoretical specific and volumetric capacities of 3860 mAh/g and 2061 mAh/cm³, respectively, along with a low reduction potential of -3.04 V vs. standard hydrogen electrode, resulting in extremely high energy density (Tarascon and Armand, 2001). However, the use of Li metal poses serious safety risk during the charge process, particularly in organic electrolytes. The metallic Li tends to deposit in the form of high-surface-area dendrites rather than homogeneously, which can grow toward the cathode and cause short circuits, potentially leading to fires or explosions. As a result, safer alternatives have been developed to replace Li metal anodes in commercial batteries.

Currently, graphite is the most widely used anode material in commercial LIBs due to its excellent electronic conductivity, high coulombic efficiency, low cost, and natural abundance (Dahn et al., 1995; Endo et al., 2000). However, graphite also has significant drawbacks. Its theoretical specific and volumetric capacities are limited to 372 mAh/g and 735 mAh/cm³, respectively, and its Li-ions intercalation kinetics are

relatively slow, which restrict the rate capability and limit further increases in energy densities for commercial LIBs (Armand and Tarascon, 2008). In addition, graphite performs poorly with larger ions like Na-ions, which do not intercalate effectively into its layered structure but instead mostly deposit over the anode surface by weak interaction (DiVincenzo and Mele, 1985; Stevens and Dahn, 2001). These limitations have motivated the search for alternative anode materials, especially for MIBs.

Beyond graphite, silicon and various alloy-based materials have been investigated as high-capacity anode candidates for MIBs (Nzereogu et al., 2022). Silicon anodes offer an extremely high theoretical capacity of 3579 mAh/g for LIB and is both earth-abundant and environmentally friendly (Chan et al., 2008). However, it suffers from significant volume expansion and contraction up to 300% during lithiation and de-lithiation, leading to mechanical stress, cracking, and capacity fading. Alloy anodes such as germanium, tin, and phosphorus offer moderate theoretical capacities and improved safety but face challenges from low electronic conductivity and high volume changes up to 100% during cycling (Lao et al., 2017; Park et al., 2010).

Two-dimensional (2D) materials have attracted considerable attention as promising anode materials for MIBs. Their atomically thin structures provide large surface areas, short diffusion paths, and superior electronic conductivity, which are advantageous for achieving fast charging and high power density (Bahari et al., 2021; Lin et al., 2020; Mukherjee et al., 2018). Unlike bulk materials that rely on intercalation, many 2D materials enable surface adsorption of metal-ions, which helps maintain structural integrity over repeated cycles. Examples of 2D anode materials include graphene and its derivatives (Kucinskis et al., 2013; M. Liang and Zhi, 2009; Ling and Mizuno, 2014), silicene (Tritsaris et al., 2013), germanene (Sharma et al., 2018), stanene (Wu et al., 2018), phosphorene (S. Zhao et al., 2014), borophene (Jiang et al., 2016; Y. Zhang et al., 2016), transition metal oxides, transition metal dichalcogenides (Hwang et al., 2011; Jing et al., 2013; E. Yang et al., 2015), and transition metal carbides/nitrides known as MXenes (Ghidu et al., 2014; Tang et al., 2012; Xie et al., 2014; D. Xiong et al., 2018).

Among these, MXenes have been extensively studied as MIB anodes due to their unique combination of high electronic conductivity, excellent mechanical

properties, chemical stability, and tunable properties by surface termination (Tang et al., 2012; D. Xiong et al., 2021; Y. Zhang et al., 2024). Their 2D layered structure also facilitates ion transport and surface adsorption. MXenes have shown potential for various carrier species, including Li^+ , Na^+ , K^+ , Mg^{2+} , and Al^{3+} , making them suitable for different MIB systems (Y. Zhang et al., 2024). However, they still face challenges such as structural restacking, limited cycling stability, and the need for deeper understanding of their working mechanisms (Aghamohammadi et al., 2022; Y. Zhang et al., 2024).

Inspired by the success of MXenes, a newly emerging class of 2D materials called MBenes has attracted growing attention as promising candidates for MIBs. Similar to MXenes, MBenes are layered transition metal compounds, but instead of carbides or nitrides, they are composed of borides (Bandaru et al., 2023; Guo et al., 2017). The substitution of lighter boron atoms in place of carbon or nitrogen is expected to result in higher theoretical capacities due to the reduced atomic mass. While early studies have shown promising electrochemical properties, fundamental understanding of their synthesis, structure, and performance as anode materials is still in the early stages.

2.3 MBenes as emerging anode materials

MBenes, derived from layered transition metal borides, are an emerging class of materials known for their unique properties and versatile applications. Thanks to the characteristics of boron, transition metal borides showcase a diverse range of structures and properties. Boron is a semi-metallic element with electronegativity of 2.04, considered as intermediate between metal and non-metal. Due to the small size of boron, three valence electrons are tightly bound to its nucleus and overcome its electron deficiency. As a result, transition metal borides feature various types of bonds, including covalent B–B bonds, metallic M–M and M–B bonds, and ionic M–B bonds. This variety in bonding allows borides to form numerous complex lattice crystal structures with unique covalent boron arrangements that are not typically seen in sulfides, nitrides, or oxides (Braunschweig and Colling, 2001; X. Sun et al., 2017). Among these complex structures, a notable subset includes the layered ternary borides known as MAB phases.

MAB phases were first reported in 1942 (Halla and Thury, 1942) and include materials such as Fe_2AlB_2 , and MoAlB , as well as a series of chromium-containing phases with varied stoichiometries (Cr_2AlB_2 , Cr_3AlB_4 , and Cr_4AlB_6) (Ade and Hillebrecht, 2015). These ternary compounds consist of an early transition metal (M), a main group element (A, typically from groups 13-15), and boron (B). MAB phases generally crystallize in either orthorhombic or hexagonal symmetry, featuring alternating stacks of transition metal-boride (M-B) layers and mono- or bi-layers of A atoms (Khazaei et al., 2019; Y. Liu et al., 2020), as illustrated in Figure 2.2.

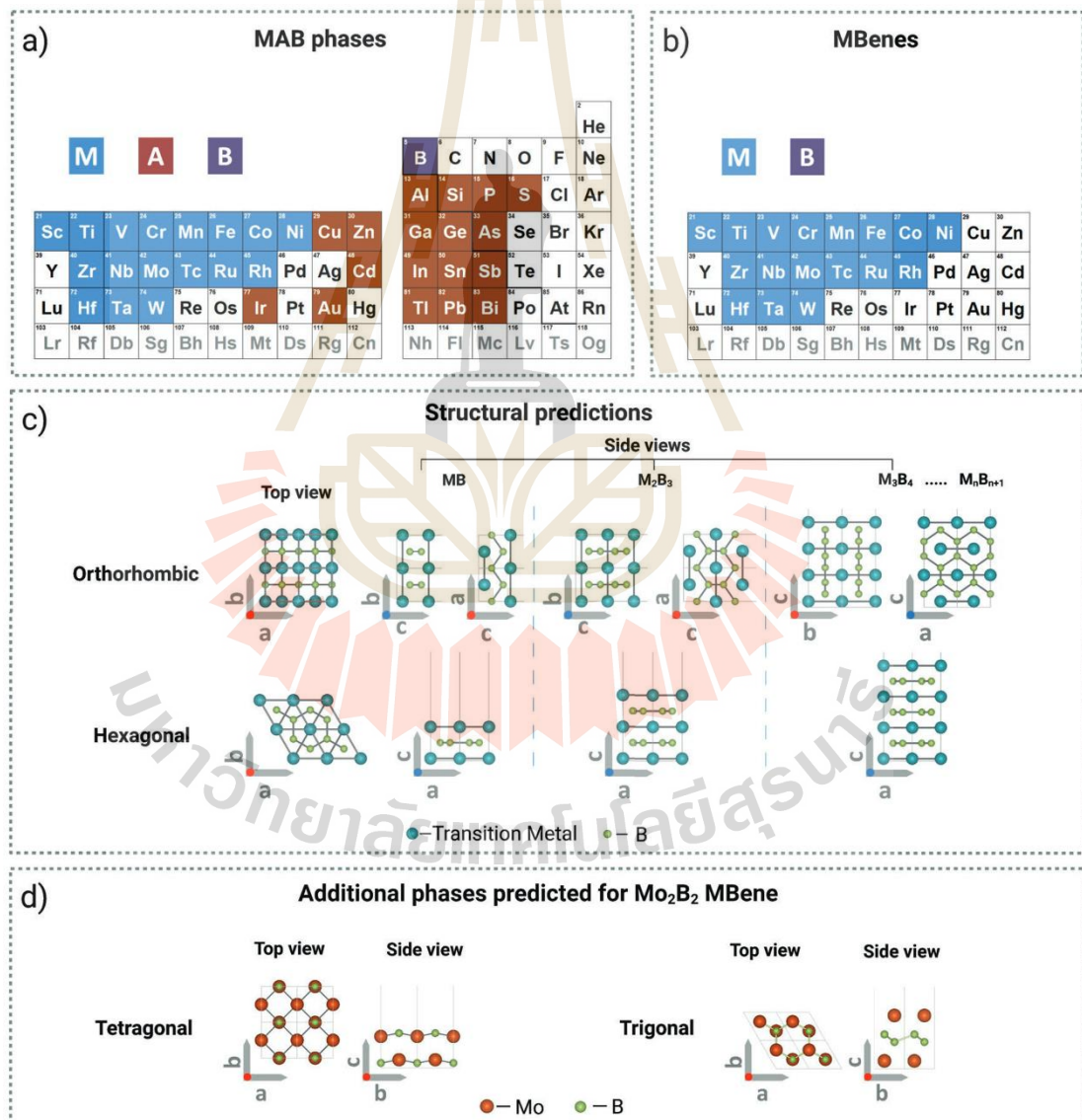


Figure 2.2 Possible compositions and structures of MBenes (Nair et al., 2022).

MBenes were first proposed in 2017 by a computational study (Guo et al., 2017), which laid the foundation for subsequent theoretical and experimental investigation, illustrated in **Figure 2.3**. In this pioneering work, Guo et al. demonstrated that 2D MBenes can be obtained by selectively removing the A-layers from MAB phases. Building on this concept, a common synthesis approach now involves using MAB phases as precursors and selectively breaking the weaker M–A bonds to isolate the M–B layers. This is typically achieved through hydrothermal etching in acid solutions such as HF or HCl (J. Wang et al., 2019; H. Zhang et al., 2018) or via topochemical intercalation using NaOH (Alameda et al., 2018; Z. Li et al., 2023). This delamination yields 2D M-B sublattices. This chemical treatment could unintentionally leave surface functional groups such as -F, -Cl, -O, or -OH. The resulting MBenes vary in lattice symmetry (e.g., orthorhombic, hexagonal) and stoichiometry (e.g., MB_2 , M_2B_2 , M_2B_3 , M_3B_4), depending on the precursor MAB phases as shown in **Figure 2.2c** (Nair et al., 2022). Moreover, recent computational studies suggest lower-energy trigonal and tetragonal phases of Mo_2B_2 as shown in **Figure 2.2d**, which could form via structural reorganization of orthorhombic or hexagonal Mo_2B_2 upon exfoliation (Bo et al., 2019). Compared to MXenes, which typically adopt hexagonal symmetry, MBenes, exhibit greater structural diversity, which could lead to completely different properties and applications (J. Chen et al., 2025).

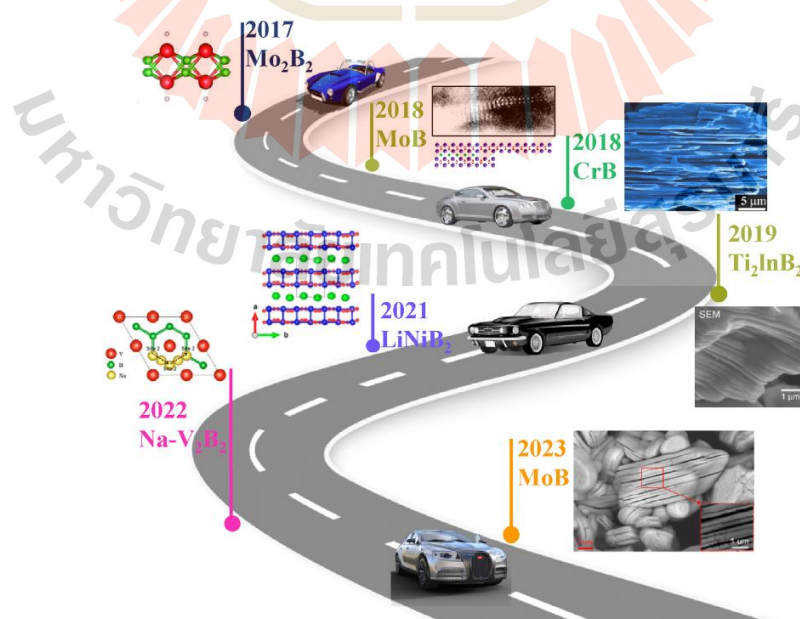


Figure 2.3 Timeline highlighting key discoveries in MBene research (Javed et al., 2024).

MBenes exhibit a range of properties that make them highly suitable for applications in electrocatalysis and energy storage. These include a large specific surface area, high electrical conductivity, hydrophilicity, and robust mechanical and thermal stability. Their performance can be further optimized by tuning their composition and surface functionalization, enabling tailored structure-property relationships (Javed et al., 2024). Such tunability makes MBenes promising candidates for electrochemical applications. For instance, Cr_4B_6 has demonstrated superior hydrogen evolution reactions performance, with overpotentials lower than that of Pt (B. Zhang et al., 2020). $\text{Cu}@\text{Mo}_2\text{B}_2$ shows lower overpotentials for bifunctional electrocatalysis for oxygen evolution and reduction reactions compared to IrO_2 and Pt (T. Zhang et al., 2021). Fe_2B_2 have also shown potential in nitrogen reduction reactions (Cheng et al., 2021). Beyond electrocatalysts, multilayer MBenes have been successfully applied as electrode materials for supercapacitors (S. Wei et al., 2023). Additionally, surface-functionalized Mo_2B_2 has been used to improve lithium-sulfur battery performance by effectively anchoring lithium polysulfides, thereby mitigating the shuttle effect (Xiao et al., 2021).

In addition to their applications in electrocatalysis and capacitive energy storage, MBenes have also emerged as promising candidates for anode materials in LIBs, offering distinct advantages over many other 2D materials due to their structural versatility, high conductivity, and abundant active sites (Xu et al., 2023). This potential is increasingly supported by experimental evidence demonstrating their electrochemical performance in Li- and Na-ion systems.

For LIBs, Xiong et al. reported the electrochemical performance of 2D Mo_2B_2 as an anode, achieving a specific capacity of 671.6 mAh/g after 50 cycles at 50 mA/g and a stable capacity of 144.2 mAh/g after 1,000 cycles at 2 A/g, confirming the structural stability of the material during long-term cycling (W. Xiong et al., 2022). Similarly, Varma et al. synthesized TiB_2 -based hierarchical nanosheets that delivered a reversible capacity of 350 mAh/g at 0.025 A/g and ultrafast charge/discharge times with 80% capacity retention over 10,000 cycles (Akash Varma et al., 2022). Miao et al. demonstrated the synthesis of 2D hexagonal $\text{Hf}_2\text{B}_2\text{O}_2$ via selective etching of In from $\text{Hf}_2\text{In}_2\text{B}_2$, reporting a capacity of 420 mAh/g as an anode (Miao et al., 2023). Chen et al.

prepared Mo_xB_y MBenes with an accordion-like structure from MoAlB using a molten salt method. It exhibited a high specific capacity of approximately 645.6 mAh/g after 100 cycles at 0.1 A/g and retained 207 mAh/g even at 4 A/g in LIBs (Y.-Z. Chen et al., 2024). Recently, Khan et al. synthesized $\text{Mo}_{4/3}\text{B}_2\text{T}_x$ MBenes via fluoride salt etching and achieved specific capacities of 283 mAh/g, along with 91.96% coulombic efficiency and stable cycling over 100 cycles (Khan et al., 2025).

For SIBs, Suriyakumar et al. explored TiB_2 -derived nanosheets as anode materials, achieving an initial discharge capacity of 252 mAh/g at 0.1 A/g and significant cycling stability at 1 A/g. In their Na-ion full cell, the anode delivered an energy density of 111 Wh/kg at a power density of 500 W/kg (Suriyakumar et al., 2022). Xiong et al. introduced a microwave-assisted hydrothermal etching process to exfoliate MoAlB into Mo_2B_2 MBenes, which delivered a reversible capacity of 196.5 mAh/g for Na-ion storage at 50 mA/g, maintaining 138.6 mAh/g after 500 cycles at 0.5 A/g (W. Xiong et al., 2025).

While these experimental results demonstrate the promising potential of MBenes as anode materials, research in this area remains in its early stages. The number of studies is still limited, with most efforts focused on a narrow range of compositions and structures. This may be partly due to the challenges of synthesizing MBenes with controlled phases and surface terminations. To advance their practical application, further work is needed to improve synthesis methods, explore broader compositional spaces, and better understand their electrochemical behavior, long-term cycling stability, and full-cell performance. In this context, computational screening offers a powerful approach to accelerate discovery by identifying promising MBene candidates and helping prioritize experimental efforts.

2.4 Computational studies on MBene anodes

Density Functional Theory (DFT) is a first-principles quantum mechanical method used to investigate the electronic structure and atomic-scale behavior of materials. In the field of energy storage, DFT has become an essential tool for accelerating materials discovery, enabling cost-effective and reliable predictions of key material properties prior to experimental synthesis and testing. In the context of MIBs, the key properties of high-performance anode materials are high reversible capacity,

good ionic and electronic conductivity, structural stability, suitable operating potential, and long-term safety as outlined in Section 2.2. DFT provides a practical and systematic framework to evaluate or screen many of these essential characteristics, thus facilitating the rational design of advanced anode materials. The methodologies for computing these properties using DFT have been well established in prior studies (He et al., 2019; Lin et al., 2020; Xu et al., 2023). In brief, the following parameters can be estimated:

- **Structural stability:** evaluated using cohesive energy, formation energy, phonon dispersion, and molecular dynamics simulations. Cohesive energy measures the bonding strength within the crystal. Formation energy quantifies the energy required to form the compound from its elemental components. Phonon dispersion analysis confirms dynamic stability by ensuring the absence of imaginary vibrational modes. Molecular dynamics simulations assess thermal stability by tracking atomic trajectories at finite temperatures.
- **Electronic properties:** assessed through density of states (DOS) and band structure calculations. DOS and Band structure reveals the distribution of electronic states near the Fermi level and identifies whether the material is metallic or semiconducting, which directly affects its ability to conduct electrons during charge and discharge.
- **Charge storage behavior:** evaluated using adsorption energy of metal ions and theoretical capacity. Adsorption energy measures the interaction strength between metal ions and the anode surface. The number of ions that can be adsorbed per formula unit is converted to capacity using simple stoichiometric formulas.
- **Open-circuit voltage (OCV):** calculated from the total energy difference between pristine and ion-inserted structures. OCV provides an estimate of the anode's average operating potential and is critical for determining the overall energy density and voltage safety margin of the battery.
- **Ion transport kinetics:** determined by calculating the diffusion barrier using the climbing image nudged elastic band (CI-NEB) method. The diffusion barrier

represents the energy required for ion migration between neighboring adsorption sites and influences rate performance and ionic conductivity.

By simulating these properties, DFT enables high-throughput screening of candidate materials and reveals trends across different compositions and structures. This not only reduces experimental trial-and-error but also supports the development of machine learning models for materials informatics. For novel systems like MBenes, where experimental data remain limited, DFT serves as a predictive tool to assess feasibility, guide synthetic efforts, and uncover structure–property relationships central to rational anode design.

The first theoretical investigation proposing MBenes as anode materials was reported by Guo et al. in 2017, marking a key milestone in MBene research (see **Figure 2.3**). In this study, the authors used DFT calculations to propose that 2D MBene could be obtained by selectively removing the A-site elements from layered MAB phases, yielding 2D transition metal borides with structural similarity to MXenes. The orthorhombic Mo_2B_2 and Fe_2B_2 MBenes were predicted to exhibit metallic electronic character, high thermal stability, and promising electrochemical properties for LIBs. Specifically, the calculated specific capacities for Mo_2B_2 and Fe_2B_2 are 444 and 665 mAh/g, respectively, while the diffusion barrier for single-atom Li ranged from 0.24 to 0.29 eV. These values compare favorably with conventional anode like graphite (372 mAh/g and ~0.3 - 0.4 eV) (Persson et al., 2010), and typical MXenes like Ti_3C_2 , (320 mAh/g and 0.28 eV) (Tang et al., 2012; Xie et al., 2014), indicating the potential of MBenes over conventional anode materials.

Since the pioneering work by Guo et al., more than 50 computational studies have been conducted to investigate MBenes as anode materials for LIBs (see **Table 2.1**). Early research mainly focused on M_2B_2 -type MBenes, inspired by the initial proposal of Mo_2B_2 and Fe_2B_2 pioneer study. These M_2B_2 structures typically crystallize in orthorhombic (ort) or hexagonal (hex) symmetries. In terms of Li storage capacity, they have been shown to offer high theoretical capacities for Li storage, ranging from 265 to 969 mAh/g, depending on the number of Li layers that can be stably accommodated. For instance, both ort- Ti_2B_2 and hex- Ti_2B_2 can adsorb one Li layer per side, corresponding to a moderate capacity of 456 mAh/g (Bo et al., 2018; J. Wang et

al., 2019). In contrast, structures such as *ort*-Cr₂B₂, *ort*-Mn₂B₂, *ort*-Fe₂B₂, *ort*-Mo₂B₂, and *hex*-Hf₂B₂ can adsorb up to two Li layers per side, resulting in significantly higher specific capacity (Jia et al., 2019; Miao et al., 2020; X. Sun et al., 2017). Surprisingly, *ort*-V₂B₂, *hex*-Y₂B₂, and *hex*-Zr₂B₂ can even adsorb up to three Li layers without significant structural distortion, reaching substantial capacities of up to 969, 806 and 654 mAh/g, respectively (Gao et al., 2021; Jia et al., 2019; Miao et al., 2020). These results suggest that the choice of transition metal significantly influences the number of Li layers that can be adsorbed, thereby affecting the overall capacity. In addition, crystal symmetry also plays an important role. For example, two lower-energy Mo₂B₂ phases, i.e., trigonal (*tri*) and tetragonal (*tetr*), identified through global structure searching method, exhibit lower theoretical capacities compared to the *ort*-phase (Bo et al., 2019).

Another key performance factor is the charge/discharge rate, which can be implied from the diffusion barrier of Li atom on the MBene material surface. Several *hex*-M₂B₂ structures have demonstrated exceptionally low diffusion barriers, including 0.017 eV for *hex*-Ti₂B₂ (Bo et al., 2018), 0.013 eV for *hex*-Y₂B₂ (Gao et al., 2021), and 0.017-0.018 eV for *hex*-Zr₂B₂ (Miao et al., 2020; Yuan et al., 2019), respectively. These values are significantly lower than those reported for most *ort*-M₂B₂ structures, which typically fall in the range of 0.21–0.29 eV (Guo et al., 2017; Jia et al., 2019).

As summarized in recent reviews (Akgul et al., 2024; Xu et al., 2023), most M₂B₂ MBenes generally offer both higher theoretical capacities and lower diffusion barriers compared to conventional anodes such as graphite and Ti₃C₂ MXene. Furthermore, the average open-circuit voltage (OCV) of *hex*-Y₂B₂ has been calculated to range from 0.43 to 0.24 V, which is lower than that of Ti₃C₂ MXene (0.62 V) and comparable to graphite (~0.2 V). This combination of high capacity, fast ion mobility, and favorable voltage characteristics highlights the strong potential of *hex*-M₂B₂ MBenes—particularly *hex*-Y₂B₂—as next-generation anode materials for LIBs (Gao et al., 2021).

While most early computational studies on MBenes focused on LIBs, recent efforts have extended their evaluation to alternative charge carriers such as Na⁺, Mg²⁺, and Al³⁺. These systems are of increasing interest due to the limited Li supply and the potential of multivalent ions to offer higher charge storage per ion, potentially increasing energy density.

Table 2.1 Comprehensive review of computational studies on MBenes-based anode for MIBs.

| Composition | Phase | M | Charge carrier | Modification | Reference |
|-------------|-----------|----------------------------------|----------------|--------------|-----------------------------|
| M_2B_2 | ort | Mo, Fe | Li | - | (Guo et al., 2017) |
| M_2B_2 | hex | Ti | Li, Na | - | (Bo et al., 2018) |
| M_2B_2 | tri, tetr | Mo | Li, Na | - | (Bo et al., 2019) |
| M_2B_2 | ort | V, Cr, Mn | Li, Na | - | (Jia et al., 2019) |
| M_2B_2 | ort | Ti | Li, Na | - | (J. Wang et al., 2019) |
| M_2B_2 | hex | Zr | Li | - | (Yuan et al., 2019) |
| MB_3 | - | Ti | Li, Na | - | (R. Li, Wang, et al., 2020) |
| M_2B_2 | ort | Cr, Mo | Mg | - | (R. Li, Liu, et al., 2020) |
| M_2B_2 | ort | Sc, Ti, V, Cr, Mn, Fe, Co, Mo | Na | - | (Z. Ma et al., 2020) |
| M_2B_2 | hex | Zr, Hf | Li, Na | - | (Miao et al., 2020) |
| M_2B | - | Mo | Li, Na | - | (Z. Wang et al., 2020) |
| M_2B | - | Mo | Li | - | (Zha et al., 2020) |
| M_2B_2 | hex | Y | Li, Na | - | (Gao et al., 2021) |
| M_2B_2 | hex | Sc, Ti, V, Cr, Zr, Nb, Mo | Li, Mg, Al | - | (He et al., 2021) |

Table 2.1 (Cont.) Comprehensive review of computational studies on MBenes-based anode for MIBs.

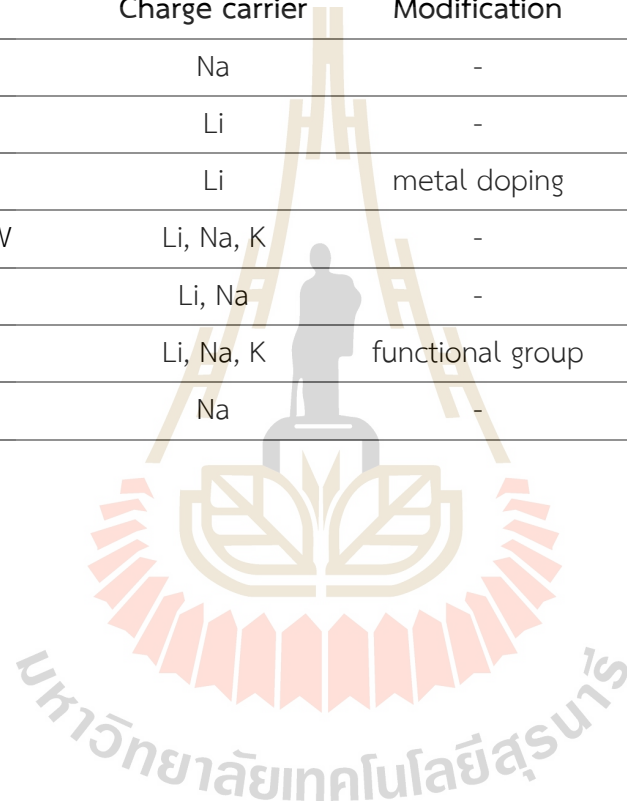
| Composition | Phase | M | Charge carrier | Modification | Reference |
|-------------|-------|-----------|----------------|------------------|-----------------------------------|
| M_2B_2 | ort | Mo | Na, K | functional group | (K. Liu et al., 2021) |
| M_2B | - | Ti | Li, Na | - | (S.-F. Wang et al., 2021) |
| MB_3 | - | V, Nb, Ta | Li | - | (Jiahui Wang et al., 2022) |
| M_2B_2 | tetr | Mo | Li | - | (Jin and Schwingenschlöggl, 2022) |
| MB_3 | - | Mo | Li | - | (Jin and Schwingenschlöggl, 2022) |
| M_2B_2 | ort | Sc, Ti, V | Li, Na | - | (Y. Li et al., 2022) |
| M_2B | - | Ti | Li, Na, K | functional group | (B. Liang et al., 2022) |
| M_2B | - | Sc, Ti, V | Li, Na, Mg | - | (N. Ma et al., 2022) |
| M_2B | - | Mo | Mg | - | (Mei et al., 2022) |
| M_2B_2 | hex | Sc, Ti | Li | alloy | (J. Wang et al., 2022) |
| M_2B | - | Ti | Li, Na | functional group | (Y. Wang et al., 2022) |
| M_2B_2 | hex | V | Na | - | (F. Wei et al., 2022) |
| M_2B_2 | hex | Sn | Na, K, Mg | - | (Yue Kuai et al., 2022) |
| MB_2 | - | Mo | Li | - | (Barik and Pal, 2023) |
| MB_6 | - | Ti | Na | - | (R. Li et al., 2023) |
| MB_4 | - | Ti | Li, Na, K | - | (Y. Li et al., 2023) |

Table 2.1 (Cont.) Comprehensive review of computational studies on MBenes-based anode for MIBs.

| Composition | Phase | M | Charge carrier | Modification | Reference |
|-------------|-------|----------------------|-------------------|------------------|--------------------------------|
| M_2B_2 | ort | Fe | Li | functional group | (Y. Liu et al., 2023) |
| MB_2 | - | Fe | Li, Na, K, Mg, Ca | - | (Luo et al., 2023) |
| MB_4 | - | Ti | Li, Na | - | (S. Ma et al., 2023) |
| M_2B_2 | ort | Fe | Li, Al | heterostructure | (Pang et al., 2023) |
| M_2B | - | V | Na | functional group | (Y. Wang, Huang, et al., 2023) |
| M_2B | - | V | Li | functional group | (Y. Wang, Ma, et al., 2023) |
| MB_2 | - | Sc, Ti, V, Nb, Mo, W | Li | - | (Han et al., 2024) |
| M_2B_3 | - | V | Li, Na | functional group | (S. Li et al., 2024) |
| M_2B_2 | hex | Ti | Li | functional group | (Lu, Kang, et al., 2024) |
| MB_4 | - | Cr, Mo, W | Mg | - | (Masood et al., 2024) |
| M_2B_2 | ort | Cr | Li, Na | functional group | (Nirjhar et al., 2024) |
| M_2B_2 | ort | Cr, Mn, Fe | Li, Na, K, Mg, Ca | - | (Y. Wang et al., 2024) |
| M_2B | - | V | Li, Ca | functional group | (Jadav et al., 2024) |
| M_2B_2 | ort | Mo | Li | functional group | (W. Zhang et al., 2024) |
| M_2B_2 | hex | Nb | Li, Na | functional group | (X. Li et al., 2024) |
| MB_2 | - | Ti | Li, Na, Mg | - | (Y. Zhao et al., 2024) |

Table 2.1 (Cont.) Comprehensive review of computational studies on MBenes-based anode for MIBs.

| Composition | Phase | M | Charge carrier | Modification | Reference |
|-------------|-------|-----------|----------------|------------------|-------------------------|
| MB_4 | - | Ti | Na | - | (J. Yang et al., 2024) |
| M_2B | - | Be | Li | - | (Lu, Liu, et al., 2024) |
| M_2B_2 | ort | Mo | Li | metal doping | (Shi et al., 2024) |
| MB_4 | - | Cr, Mo, W | Li, Na, K | - | (Masood et al., 2024) |
| M_2B_2 | hex | Mg, Ca | Li, Na | - | (Y. Sun et al., 2024) |
| M_2B | - | Mo | Li, Na, K | functional group | (Ahmad et al., 2024) |
| M_2B_2 | ort | Mo | Na | - | (W. Xiong et al., 2025) |



For SIBs, Jia et al. reported that *ort*-V₂B₂ can adsorb up to three Na layers, achieving an extreme specific capacity of 614 mAh/g without structural degradation. The calculated diffusion barrier for Na on *ort*-V₂B₂ surface was also found to be relatively low, indicating favorable ion mobility (Jia et al., 2019). Similarly, *hex*-Ti₂B₂, *hex*-Y₂B₂, and *hex*-Zr₂B₂ have been suggested as promising candidates for Na storage. Although these materials typically exhibit lower specific capacities due to the higher atomic mass of Na compared to Li, they may benefit from enhanced diffusion kinetics, as weaker Na-surface interactions (Bo et al., 2018; Gao et al., 2021; Miao et al., 2020).

For multivalent-ion batteries, Li et al. investigated Mg-ion storage on *ort*-Cr₂B₂ and *ort*-Mo₂B₂ (R. Li, Liu, et al., 2020). The reported theoretical capacities were 853.4 and 502.1 mAh/g, respectively, with corresponding diffusion barriers of 0.38 eV and 0.81 eV, and average OCVs of 0.53 V and 0.67 V. Although these values are promising, the higher diffusion barriers reflect the larger ionic radius and stronger interaction of multivalent ions with the MBene surface, which could limit their rate performance. Further systematic screening by He et al. (He et al., 2021) on seven *hex*-M₂B₂ systems for multivalent-ion batteries showed similar trends. MBenes containing heavier transition metals generally demonstrated stronger bonding to the carrier species, lower reaction voltages, and higher dynamic stability. Adsorption energies across different carrier species followed the trend Al > Mg > Li, reflecting increased binding strength with higher charge and smaller ionic radius. These results suggest that while MBenes are promising multivalent-ion storage, performance trade-offs must be considered, particularly in balancing ion mobility and adsorption strength.

In addition to the widely studied M₂B₂-type MBenes, a growing number of theoretical studies have explored MBenes with other stoichiometries, such as M₂B, MB₂, MB₃, MB₄, and MB₆. These studies aim to expand the MBene design space and discover structures with optimized performance for anode applications. Unlike M₂B₂ structures, which are typically derived from known layered MAB phases, many of the alternative stoichiometries have been proposed through global structure prediction methods. For example, Jin et al. used structure searching and phonon calculations to assess the stability of Mo-based MBenes including Mo₂B₂, MoB₂, MoB₃, and MoB₄ (Jin and Schwingenschlöggl, 2022). Among them, only Mo₂B₂ and MoB₃ were identified as

dynamically stable and potentially suitable for anode applications, whereas MoB_2 and MoB_4 showed structural instabilities. Other stoichiometries and compositions such as M_2B (N. Ma et al., 2022; S.-F. Wang et al., 2021; Z. Wang et al., 2020), MB_2 (Han et al., 2024; Luo et al., 2023), MB_3 (Jiahui Wang et al., 2022; R. Li, Wang, et al., 2020), and MB_4 (Y. Li et al., 2023; S. Ma et al., 2023), have been computationally screened. These materials exhibit a wide range of structural configurations and electrochemical behaviors, with some showing high theoretical capacities and reasonable ion diffusion barriers. However, their stabilities and synthesis feasibility remain less understood compared to the M_2B_2 -type MBenes.

This section presents a statistical analysis of computational studies on MBene anode materials, focusing on publication trends and identifying areas that remain underexplored. The analysis includes works published between 2017 and 2025, based on the dataset summarized in **Table 2.1** and visualized in **Figure 2.4**.

As shown in **Figure 2.4a**, the number of publications has steadily increased since the first computational report in 2017, with a marked rise beginning in 2020. This upward trend reflects growing interest in the potential of MBenes for metal-ion battery applications and underscores the need for a broader and more systematic exploration of their compositional and structural diversity. Among the compositions studied, M_2B_2 type MBenes dominate the field, accounting for approximately 60% of all structures reported (**Figure 2.4b**). These are followed by M_2B and MB_2 stoichiometries, while MB_3 , MB_4 , and other less conventional forms remain relatively rare in the literature. Within the M_2B_2 family, most studies have focused on *ort*- and *hex*-phases, which are directly derived from layered MAB precursors. Although lower-energy *tri*- and *tetr*-phases variants have been predicted especially for Mo_2B_2 , these alternative phases have not yet been widely explored for other transition metals (**Figure 2.4b**).

Regarding elemental composition, research has primarily concentrated on early transition metals such as Ti, V, and Mo (**Figure 2.4c**). In contrast, MBenes containing late 3d elements (e.g., Fe, Co, Ni, Cu), many 4d elements (beyond Mo), and nearly all 5d elements remain largely uninvestigated. **Figure 2.4d** shows that Li is the most extensively studied charge carrier in MBene anode, followed by Na and Mg. Studies involving other carrier species such as K, Al, and Ca are scarce.

At the earlier, while most screening efforts focus on bare (unfunctionalized) MBene surfaces, recent studies consider surface terminations (e.g., $-O$, $-OH$, $-F$) result from either chemical treatments or intentional modification and likely to form under realistic synthesis conditions. In this thesis, we focus on bare M_2B_2 because the M_2B_2 stoichiometry is the most widely studied and well-characterized and bare surfaces allow for direct evaluation of intrinsic material properties without the added complexity and variability introduced by surface terminations. **Figures 2.4e-f** present a consistent pattern: most studies have concentrated on a limited group of early transition metals (e.g., Ti, V, Mo) and carrier species (primarily Li, followed by Na and Mg), while other potentially promising carrier species remain largely unexplored.

This narrow research focus highlights an imbalance in current computational screening efforts. To develop a more comprehensive understanding of MBene anode behavior, future studies should expand to include underexplored compositions, diverse crystal phases, and multivalent carriers. Broadening this scope will help capture more complete structure–property relationships and may uncover new candidates with superior electrochemical performance for next-generation MIBs.

Despite the increasing number of computational studies on MBene anodes (see **Table 2.1**), comparing their predicted electrochemical performance remains challenging due to methodological inconsistencies. Variations in computational setups, such as the choice of exchange–correlation functional, treatment of van der Waals (vdW) interactions, supercell size, convergence criteria, and definitions of performance metrics, can lead to significant discrepancies in the reported results. For example, Fe_2B_2 has been studied by three independent groups (Guo et al., 2017; Y. Liu et al., 2023; Y. Wang et al., 2024), with notable variations in key performance. Although two studies reported the same Li diffusion barrier of 0.24 eV, the third reported a significantly higher value of 0.37 eV, likely due to the inclusion of DFT-D2 vdW corrections. Reported average open-circuit voltages (OCVs) are varied from 0.33, 1.08, and 4.7 V, while gravimetric capacities span from 665, 364, and 804 mAh/g, depending on the number of adsorbed Li layers and the formulas used to compute these values. These inconsistencies limit the ability to draw meaningful comparisons across studies or identify generalizable structure–property relationships. To improve data reliability

and support reproducible screening, future studies should adopt standardized methodologies and report key computational parameters in a transparent manner. Such practices are critical for building high-quality databases and enabling the use of data-driven approaches, including machine learning, in MBene-based anode design.

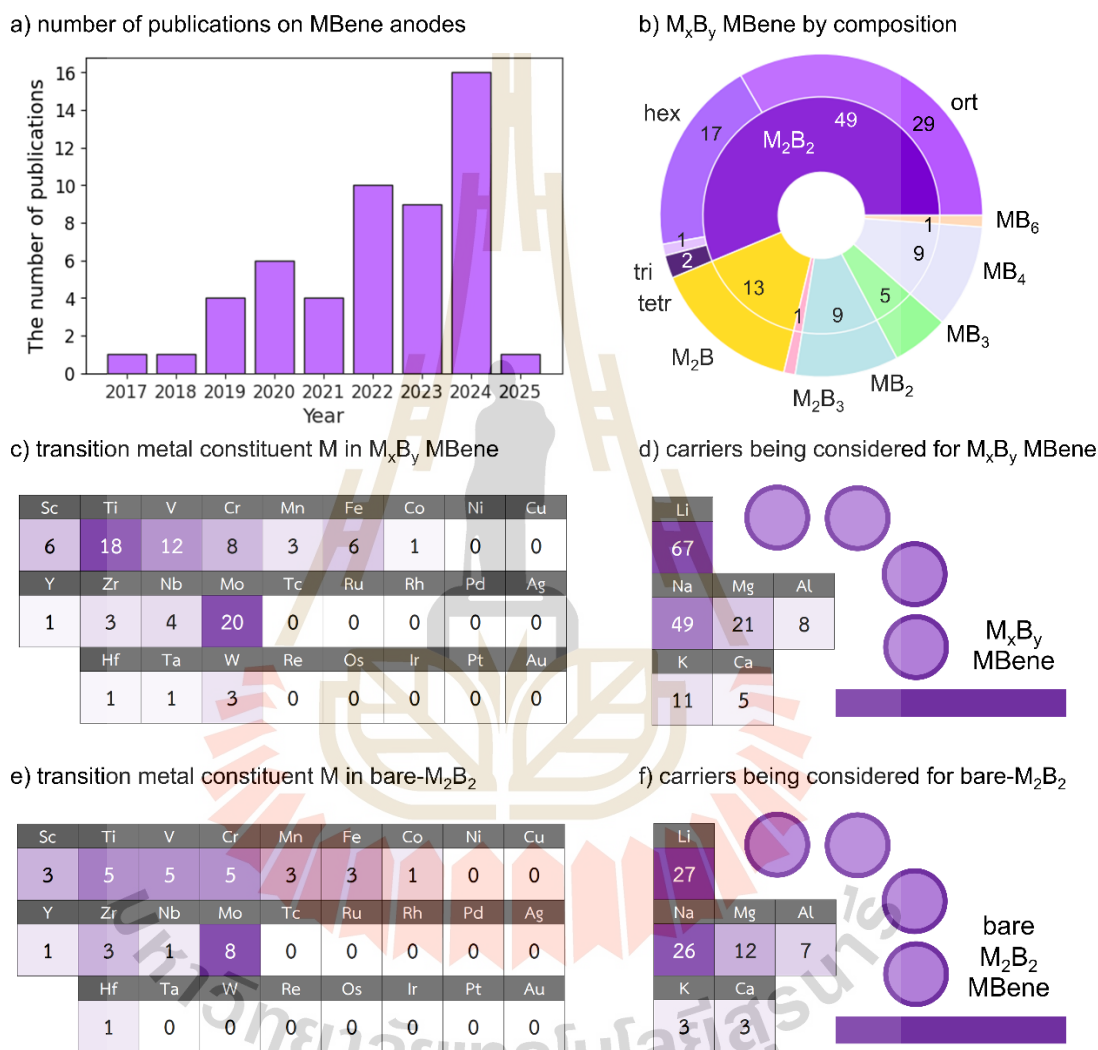


Figure 2.4 Different visualizations of previous computational studies in Table 2.1. a) number of publications each year from 2017 to 2025; b-d) number of M_xB_y MBene structures being considered as MIB anode b) based on compositions and phases (ort-, hex-, tri-, and tetra- M_2B_2); c) based on different constituent metal M; and d) based on different carriers. e-f) number of bare- M_2B_2 MBene structures being considered for MIB anodes e) based on different constituent metal M; and f) based on different carriers.

Recent advances in high-throughput DFT and data-driven approaches have enabled more systematic screening of MBene materials, supporting both synthesis planning and performance prediction. These efforts rely on consistent, high-quality computational databases that reveal correlations between composition, structure, and electrochemical behavior.

One application of this approach is in guiding the synthesis of MAB phases, the precursors to MBenes. Using DFT calculations combined with machine learning, several studies have proposed synthesizable MAB compositions (S. Li et al., 2024; Miao et al., 2020; Y. Sun et al., 2023). For instance, Hf_2InB_2 was computationally predicted as a viable precursor for Hf_2B_2 , and its successful experimental synthesis later confirmed the model (Miao et al., 2023). This illustrates the value of computational screening in bridging theoretical design and experimental realization.

In addition, several studies have focused on uncovering chemically intuitive trends to explain the electrochemical behavior of MBenes through analysis of their electronic and structural properties, providing valuable insight grounded in physical chemistry. He et al. (He et al., 2021) examined seven hex- M_2B_2 systems composed of 3d and 4d transition metals and identified the important descriptor. Within each period, heavier transition metals correlated with greater dynamic stability, stronger binding to carrier species, and lower reaction voltages. The study also found that electronegativity of carrier species influenced its behavior: more electronegative carrier showed stronger adsorption but reduced diffusion, highlighting a trade-off between carrier retention and mobility. In a related study, Han et al. (Han et al., 2024) investigated MB_2 MBenes and identified electronic structure features that correlate with Li adsorption and diffusion behavior. They observed that the shift of the B p-band center closer to the Fermi level led to stronger Li adsorption (**Figure 2.5b**), attributed to enhanced hybridization between metal and boron orbitals (**Figure 2.5a**). Additionally, systems with greater charge transfer from Li to the MBene surface tended to exhibit higher diffusion barriers (**Figure 2.5c**). These findings demonstrate how electronic features can help explain observed performance trends and offer useful guidance for rational MBene design.

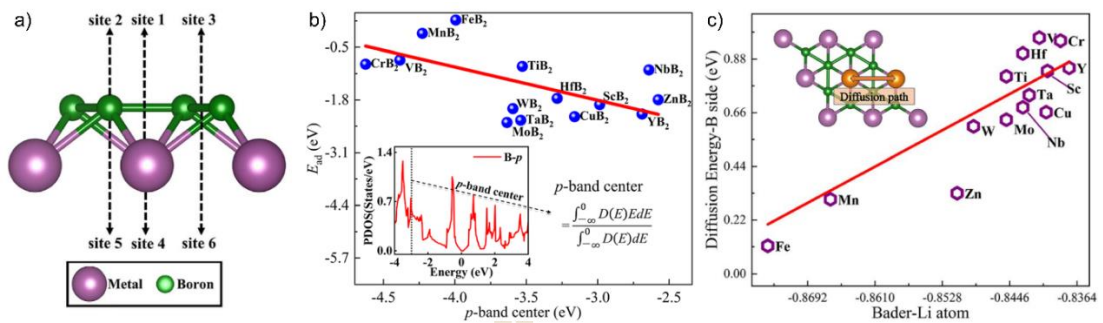


Figure 2.5 Computational screening of MB₂ for lithium-ion batteries. a) crystal structure of MB₂. b) correlation between adsorption energy of single atom Li on MB₂ (E_{ad}) and the p-band center of B atoms. c) correlation between diffusion barrier of single atom Li on B-side of MB₂ and Bader charge of the Li atom. (Han et al., 2024).

Together, these studies underscore the role of data-driven methods in uncovering meaningful structure–property relationships. As emphasized by Ghiringhelli et al. (Ghiringhelli et al., 2015), a key challenge in materials informatics lies in identifying physically interpretable features that connect atomic-scale interactions with macroscopic performance. In the context of MBenes, such descriptors are essential for understanding carrier adsorption, optimizing anode behavior, and accelerating the discovery of next-generation battery materials.

2.5 Summary of literature gap

The search for high-performance anode materials for MIBs has led to increasing interest in 2D materials, particularly MBenes. Despite their potential, current studies remain fragmented and limited in scope. Experimental work on MBenes is still in its infancy due to synthetic challenges, with only a few compositions such as Mo₂B₂, Hf₂B₂, and TiB₂ explored to date. From a computational perspective, most studies have focused on a narrow subset of MBenes, specifically bare M₂B₂ structures composed of a small group of transition metals (Ti, V, Cr, Mo) and evaluated primarily for Li and Na storage. Other promising transition elements, alternative phases, and multivalent ions such as Mg and Al remain largely unexplored. Furthermore, inconsistent use of computational parameters—such as supercell size, vdW corrections, and capacity or voltage formulas—has made it difficult to compare results across different studies or extract general trends.

Although some studies have proposed candidate materials and observed property trends, few have systematically explored how structural or compositional features influence anode performance across the MBene family. In particular, there remains a lack of studies aiming to identify important descriptors and explain their effects from a chemical perspective. As a result, much of the existing work is limited to isolated case studies, and the design of new MBene anodes lacks general guidance based on structure–property understanding.

To address these limitations, this thesis undertakes a comprehensive and consistent computational screening of bare- M_2B_2 MBenes as potential anode materials for MIBs. This study is designed with the following objectives:

- Systematically explore bare- M_2B_2 structures across various crystal phases: ort, hex, tri, and tetr;
- Expand the compositional space by considering transition metals from 3d, 4d, and 5d;
- Evaluate various carrier species: Li, Na, Mg, and Al;
- Apply a unified DFT framework to consistently calculate key anode-relevant properties: structural stability, electronic structure, adsorption capacity, open-circuit voltage, and diffusion barrier;
- Identify performance trends and suggest promising candidates beyond those previously studied;
- Propose physically interpretable structure–property relationships to support rational material design and deepen understanding of carrier species and MBene interactions.

By addressing both the methodological inconsistencies and the limited chemical and structural scope in existing studies, this research seeks to provide a clearer understanding of MBene performance and offers practical insights for the development of next-generation anode materials.

2.6 References

- Ade, M., and Hillebrecht, H. (2015). Ternary Borides Cr₂AlB₂, Cr₃AlB₄, and Cr₄AlB₆: The First Members of the Series (CrB₂)_nCrAl with n = 1, 2, 3 and a Unifying Concept for Ternary Borides as MAB-Phases. *Inorganic Chemistry*, 54(13), 6122–6135.
- Aghamohammadi, H., Eslami-Farsani, R., and Castillo-Martinez, E. (2022). Recent trends in the development of MXenes and MXene-based composites as anode materials for Li-ion batteries. *Journal of Energy Storage*, 47, 103572.
- Ahmad, S., Xu, H., Chen, L., Din, H. U., and Zhou, Z. (2024). Functionalized MBenes as promising anode materials for high-performance alkali-ion batteries: a first-principles study. *Nanotechnology*, 35(28), 285401.
- Akash Varma, Badam, R., Asha Liza James, Koichi Higashimine, Jasuja, K., and Matsumi, N. (2022). Titanium Diboride-Based Hierarchical Nanosheets as Anode Material for Li-Ion Batteries. *ACS Applied Nano Materials*.
- Akgul, E. T., Altinci, O. C., Umay, A., Aghamohammadi, P., Farghaly, A. A., Ma, P., Chen, Y., and Demir, M. (2024). Nanoengineering of 2D MBenes for energy storage applications: A review. *Journal of Energy Storage*, 84, 110882.
- Alameda, L. T., Moradifar, P., Metzger, Z. P., Alem, N., and Schaak, R. E. (2018). Topochemical Deintercalation of Al from MoAlB: Stepwise Etching Pathway, Layered Intergrowth Structures, and Two-Dimensional MBene. *Journal of the American Chemical Society*, 140(28), Article 28.
- Armand, M., and Tarascon, J.-M. (2008). Building better batteries. *Nature*, 451(7179), 652–657.
- Bahari, Y., Mortazavi, B., Rajabpour, A., Zhuang, X., and Rabczuk, T. (2021). Application of two-dimensional materials as anodes for rechargeable metal-ion batteries: A comprehensive perspective from density functional theory simulations. *Energy Storage Materials*, 35, 203–282.
- Bandaru, S., Jastrzebska, A. M., and Birowska, M. (2023). Recent progress in thermoelectric MXene-based structures versus other 2D materials. *Applied Materials Today*, 34, 101902.

- Barik, G., and Pal, S. (2023). Monolayer molybdenum diborides containing flat and buckled boride layers as anode materials for lithium-ion batteries. *Physical Chemistry Chemical Physics*, 25(26), 17667–17679.
- Berg, E. J., Villevieille, C., Streich, D., Trabesinger, S., and Novák, P. (2015). Rechargeable Batteries: Grasping for the Limits of Chemistry. *Journal of The Electrochemical Society*, 162(14), A2468.
- Bo, T., Liu, P.-F., Xu, J., Zhang, J., Chen, Y., Eriksson, O., Wang, F., and Wang, B.-T. (2018). Hexagonal Ti₂B₂ monolayer: a promising anode material offering high rate capability for Li-ion and Na-ion batteries. *Physical Chemistry Chemical Physics*, 20(34), Article 34.
- Bo, T., Liu, P.-F., Zhang, J., Wang, F., and Wang, B.-T. (2019). Tetragonal and trigonal Mo₂B₂ monolayers: two new low-dimensional materials for Li-ion and Na-ion batteries. *Physical Chemistry Chemical Physics*, 21(9), Article 9.
- Braunschweig, H., and Colling, M. (2001). Transition metal complexes of boron — synthesis, structure and reactivity. *Coordination Chemistry Reviews*, 223(1), 1–51.
- Canepa, P., Sai Gautam, G., Hannah, D. C., Malik, R., Liu, M., Gallagher, K. G., Persson, K. A., and Ceder, G. (2017). Odyssey of Multivalent Cathode Materials: Open Questions and Future Challenges. *Chemical Reviews*, 117(5), 4287–4341.
- Chan, C. K., Peng, H., Liu, G., McIlwrath, K., Zhang, X. F., Huggins, R. A., and Cui, Y. (2008). High-performance lithium battery anodes using silicon nanowires. *Nature Nanotechnology*, 3(1), 31–35.
- Chayambuka, K., Mulder, G., Danilov, D. L., and Notten, P. H. L. (2020). From Li-Ion Batteries toward Na-Ion Chemistries: Challenges and Opportunities. *Advanced Energy Materials*, 10(38), 2001310.
- Chen, J., Zhang, W., Chen, R., Dai, Y., Zhang, J., Yang, H., Zong, W., Jiang, Z., Zhong, Y., Wang, J., Zhang, X., and He, G. (2025). From Synthesis to Energy Storage, The Microchemistry of MXene and MBene. *Advanced Energy Materials*, 15(17), 2403757.

- Chen, Y.-Z., Mao, T.-T., Liao, S.-Y., Yao, S. X., and Min, Y.-G. (2024). Layered MoxBy (MBenes) derived by a molten-salt method and their application in advanced LIB anodes. *Journal of Materials Chemistry A*, 12(20), 12163–12172.
- Cheng, Y., Mo, J., Li, Y., Zhang, Y., and Song, Y. (2021). A systematic computational investigation of the water splitting and N₂ reduction reaction performances of monolayer MBenes. *Physical Chemistry Chemical Physics*, 23(11), Article 11.
- Dahn, J. R., Zheng, T., Liu, Y., and Xue, J. S. (1995). Mechanisms for Lithium Insertion in Carbonaceous Materials. *Science*, 270(5236), 590–593.
- Delmas, C. (2018). Sodium and Sodium-Ion Batteries: 50 Years of Research. *Advanced Energy Materials*, 8(17), 1703137.
- Deng, D. (2015). Li-ion batteries: basics, progress, and challenges. *Energy Science & Engineering*, 3(5), 385–418.
- DiVincenzo, D. P., and Mele, E. J. (1985). Cohesion and structure in stage-1 graphite intercalation compounds. *Physical Review B*, 32(4), 2538–2553.
- Endo, M., Kim, C., Nishimura, K., Fujino, T., and Miyashita, K. (2000). Recent development of carbon materials for Li ion batteries. *Carbon*, 38(2), 183–197.
- Gao, S., Hao, J., Zhang, X., Li, L., Zhang, C., Wu, L., Ma, X., Lu, P., and Liu, G. (2021). Two dimension transition metal boride Y₂B₂ as a promising anode in Li-ion and Na-ion batteries. *Computational Materials Science*, 200, 110776.
- Ghidiu, M., Lukatskaya, M. R., Zhao, M.-Q., Gogotsi, Y., and Barsoum, M. W. (2014). Conductive two-dimensional titanium carbide ‘clay’ with high volumetric capacitance. *Nature*, 516(7529), 78–81.
- Ghiringhelli, L. M., Vybiral, J., Levchenko, S. V., Draxl, C., and Scheffler, M. (2015). Big Data of Materials Science: Critical Role of the Descriptor. *Physical Review Letters*, 114(10), 105503.
- Goodenough, J. B., and Park, K.-S. (2013). The Li-Ion Rechargeable Battery: A Perspective. *Journal of the American Chemical Society*, 135(4), Article 4.
- Guo, Z., Zhao, S., Li, T., Su, D., Guo, S., and Wang, G. (2020). Recent Advances in Rechargeable Magnesium-Based Batteries for High-Efficiency Energy Storage. *Advanced Energy Materials*, 10(21), 1903591.

- Guo, Z., Zhou, J., and Sun, Z. (2017). New two-dimensional transition metal borides for Li ion batteries and electrocatalysis. *Journal of Materials Chemistry A*, 5(45), Article 45.
- Halla, F., and Thury, W. (1942). Über Boride von Molybdän und Wolfram. *Zeitschrift Für Anorganische Und Allgemeine Chemie*, 249(3), 229–237.
- Han, Y., Wang, L., Zheng, B., Wang, J., Zhang, L., and Xiao, B. (2024). Exploring the potential of MB₂ MBene family as promising anodes for Li-ion batteries. *RSC Advances*, 14(16), 11112–11120.
- He, Q., Li, Z., Xiao, W., Zhang, C., and Zhao, Y. (2021). Computational investigation of 2D 3d/4d hexagonal transition metal borides for metal-ion batteries. *Electrochimica Acta*, 384, 138404.
- He, Q., Yu, B., Li, Z., and Zhao, Y. (2019). Density Functional Theory for Battery Materials. *ENERGY & ENVIRONMENTAL MATERIALS*, 2(4), 264–279.
- Hwang, H., Kim, H., and Cho, J. (2011). MoS₂ Nanoplates Consisting of Disordered Graphene-like Layers for High Rate Lithium Battery Anode Materials. *Nano Letters*, 11(11), 4826–4830.
- Jadav, R. P., Singh, D., Ahuja, R., and Sonvane, Y. (2024). Harnessing MBene termination for superior anode interfaces in Li/Ca-ion batteries. *Journal of Energy Storage*, 101, 113995.
- Javed, M. S., Zhang, X., Ahmad, T., Usman, M., Shah, S. S. A., Ahmad, A., Hussain, I., Majeed, S., Khawar, M. R., Choi, D., Xia, C., Al Zoubi, W., Assiri, M. A., Hassan, A. M., Ali, S., and Han, W. (2024). MXenes to MBenes: Latest development and opportunities for energy storage devices. *Materials Today*, 74, 121–148.
- Jayaprakash, N., Das, S. K., and Archer, L. A. (2011). The rechargeable aluminum-ion battery. *Chemical Communications*, 47(47), 12610–12612.
- Jia, J., Li, B., Duan, S., Cui, Z., and Gao, H. (2019). Monolayer MBenes: prediction of anode materials for high-performance lithium/sodium ion batteries. *Nanoscale*, 11(42), Article 42.
- Jiahui Wang, Lina Bai, Xiangru Zhao, Gao, H., and Li Niu. (2022). A DFT prediction of two-dimensional MB₃ (M = V, Nb, and Ta) monolayers as excellent anode materials for lithium-ion batteries. *RSC Advances*, 12(44), 28525–28532.

- Jiang, H. R., Lu, Z., Wu, M. C., Ciucci, F., and Zhao, T. S. (2016). Borophene: A promising anode material offering high specific capacity and high rate capability for lithium-ion batteries. *Nano Energy*, *23*, 97–104.
- Jin, J., and Schwingenschlögl, U. (2022). Exploration of two-dimensional molybdenum-borides and potential applications. *Npj 2D Materials and Applications*, *6*(1), Article 1.
- Jing, Y., Zhou, Z., Cabrera, C. R., and Chen, Z. (2013). Metallic VS₂ Monolayer: A Promising 2D Anode Material for Lithium Ion Batteries. *The Journal of Physical Chemistry C*, *117*(48), 25409–25413.
- Khan, M. U., Du, L., San, X., Zhou, Y., Jiang, M., Chu, L., Feng, Q., and Hu, C. (2025). Synthesis and electrochemical properties of Mo₄/3B₂T_x MBene as an anode material for lithium-ion batteries. *Journal of Applied Electrochemistry*.
- Khazaei, M., Wang, J., Estili, M., Ranjbar, A., Suehara, S., Arai, M., Esfarjani, K., and Yunoki, S. (2019). Novel MAB phases and insights into their exfoliation into 2D MBenes. *Nanoscale*, *11*(23), Article 23.
- Kim, D. J., Yoo, D.-J., Otley, M. T., Prokofjevs, A., Pezzato, C., Owczarek, M., Lee, S. J., Choi, J. W., and Stoddart, J. F. (2019). Rechargeable aluminium organic batteries. *Nature Energy*, *4*(1), 51–59.
- Kucinskis, G., Bajars, G., and Kleperis, J. (2013). Graphene in lithium ion battery cathode materials: A review. *Journal of Power Sources*, *240*, 66–79.
- Lao, M., Zhang, Y., Luo, W., Yan, Q., Sun, W., and Dou, S. X. (2017). Alloy-Based Anode Materials toward Advanced Sodium-Ion Batteries. *Advanced Materials*, *29*(48), 1700622.
- Li, H., Wang, Z., Chen, L., and Huang, X. (2009). Research on Advanced Materials for Li-ion Batteries. *Advanced Materials*, *21*(45), 4593–4607.
- Li, R., Liu, Y., Deng, H., Yu, C., and Liu, Z. (2020). A First-Principles Study of MBene as Anode Material for Mg-Ion Battery. *Journal of Electrochemical Energy Conversion and Storage*, *17*(4), Article 4.
- Li, R., Wang, Y., Xu, L.-C., Shen, J., Zhao, W., Yang, Z., Liu, R., Shao, J.-L., Guo, C., and Li, X. (2020). A boron-exposed TiB₃ monolayer with a lower electrostatic-potential

- surface as a higher-performance anode material for Li-ion and Na-ion batteries. *Physical Chemistry Chemical Physics*, 22(39), Article 39.
- Li, R., Wang, Y., Yang, Z., and Xu, L.-C. (2023). Unveiling the Potential of Boron-Rich Two-Dimensional TiB₆ Monolayer as a High-Performance Anode Material for Sodium-Ion Batteries: Insights into Correlation Mechanisms for Multi-Ion Migration. *Crystal Growth & Design*.
- Li, S., Sun, W., Zhu, T., Wang, S., Zhang, J., Yu, J., Zheng, W., Ying, G., Sun, L., and Geng, H. (2024). Top-down design of high-performance V-based MBene anode for Li/Na-ion batteries. *Physical Chemistry Chemical Physics*, 26(7), 6396–6409.
- Li, X., Liu, Y., Wang, H., Yu, W., Fu, Y., Wu, Q., Hu, Q., and Zhou, A. (2024). Theoretical investigation of NbB as an electrode material for Li/Na-ion batteries. *Physica Scripta*, 99(6), 0659a4.
- Li, Y., Yang, W., Yu, F., Huang, R., and Wen, Y. (2023). Computational determination of a graphene-like TiB₄ monolayer for metal-ion batteries and a nitrogen reduction electrocatalyst. *Physical Chemistry Chemical Physics*, 25(10), Article 10.
- Li, Y., Zhao, T., Li, L., Huang, R., and Wen, Y. (2022). Computational evaluation of ScB and TiB MBenes as promising anode materials for high-performance metal-ion batteries. *Physical Review Materials*, 6(4), Article 4.
- Li, Z., Zeng, Q., Yu, Y., Liu, Y., Chen, A., Guan, J., Wang, H., Liu, W., Liu, X., Liu, X., and Zhang, L. (2023). Application of transition metal boride nanosheet as sulfur host in high loading Li-S batteries. *Chemical Engineering Journal*, 452, 139366.
- Liang, B., Ma, N., Wang, Y., Wang, T., and Fan, J. (2022). N-functionalized Ti₂B MBene as high-performance anode materials for sodium-ion batteries: A DFT study. *Applied Surface Science*, 599, 153927.
- Liang, M., and Zhi, L. (2009). Graphene-based electrode materials for rechargeable lithium batteries. *Journal of Materials Chemistry*, 19(33), 5871–5878.
- Lin, J., Yu, T., Han, F., and Yang, G. (2020). Computational predictions of two-dimensional anode materials of metal-ion batteries. *WIREs Computational Molecular Science*, 10(5), e1473.

- Ling, C., and Mizuno, F. (2014). Boron-doped graphene as a promising anode for Na-ion batteries. *Physical Chemistry Chemical Physics*, 16(22), 10419–10424.
- Liu, F., Wang, T., Liu, X., and Fan, L.-Z. (2021). Challenges and Recent Progress on Key Materials for Rechargeable Magnesium Batteries. *Advanced Energy Materials*, 11(2), 2000787.
- Liu, K., Zhang, B., Chen, X., Huang, Y., Zhang, P., Zhou, D., Du, H., and Xiao, B. (2021). Modulating the Open-Circuit Voltage of Two-Dimensional MoB MBene Electrode via Specific Surface Chemistry for Na/K Ion Batteries: A First-Principles Study. *The Journal of Physical Chemistry C*, 125(33), Article 33.
- Liu, Y., Jiang, Z., Jiang, X., and Zhao, J. (2020). New refractory MAB phases and their 2D derivatives: insight into the effects of valence electron concentration and chemical composition. *RSC Advances*, 10(43), 25836–25847.
- Liu, Y., Wang, H., Fu, Y., Li, D., Wei, M., Wu, Q., and Hu, Q. (2023). Functionalized two-dimensional iron boride compounds as novel electrode materials in Li-ion batteries. *Physical Chemistry Chemical Physics*, 25(34), 23133–23140.
- Lu, Z., Kang, Y., Du, Y., Ma, X., Ma, W., and Zhang, J. (2024). Functionalizing Janus-structured Ti₂B₂ unveils exceptional capacity and performance in lithium-ion battery anodes. *Journal of Colloid and Interface Science*, 661, 662–670.
- Lu, Z., Liu, C.-S., and Ye, X.-J. (2024). Be₂B monolayer as a well-balanced performance anode for lithium-ion batteries with ultrahigh theoretical capacity and low diffusion barrier. *Journal of Applied Physics*, 136(22), 225001.
- Luo, S., Zhao, J., Wang, Y., Zhang, Y., Xiong, Y., Ma, N., and Fan, J. (2023). First-Principles Study of FeB₂ Monolayers as High-Capacity Electrode Materials for Mg-Ion Batteries. *The Journal of Physical Chemistry C*, 127(26), 12484–12491.
- Ma, N., Wang, T., Li, N., Li, Y., and Fan, J. (2022). New phases of MBenes M₂B (M = Sc, Ti, and V) as high-capacity electrode materials for rechargeable magnesium ion batteries. *Applied Surface Science*, 571, 151275.
- Ma, S., Zhang, H., Cheng, Z., Xie, X., Zhang, X., Liu, G., and Chen, G. (2023). A novel two-dimensional whorled TiB₄ as a high-performance anode material for Li-ion and Na-ion batteries. *Applied Surface Science*, 639, 158083.

- Ma, Z., Sun, F., Dou, M., Yao, Q., Liu, Y., and Wu, F. (2020). Are transition-metal borides promising for Na ion batteries? A first-principles study on transition-metal boride monolayer. *Physics Letters A*, 384(14), Article 14.
- Masood, M. K., Wang, J., Song, J., and Liu, Y. (2024). A novel two-dimensional monolayer MB₄(M = Cr, Mo, W) MBenes as a high-performance anode material for Mg-ion batteries. *Journal of Energy Storage*, 86, 111370.
- Matsui, M. (2011). Study on electrochemically deposited Mg metal. *Journal of Power Sources*, 196(16), 7048–7055.
- Mei, T., Wu, J., Lu, S., Wang, B., Zhao, X., Wang, L., and Yin, Z. (2022). First-principles investigations to evaluate Mo₂B monolayers as promising two-dimensional anode materials for Mg-ion batteries. *Journal of Physics: Energy*, 4(3), Article 3.
- Miao, N., Gong, Y., Zhang, H., Shen, Q., Yang, R., Zhou, J., Hosono, H., and Wang, J. (2023). Discovery of Two-dimensional Hexagonal MBene HfBO and Exploration on its Potential for Lithium-Ion Storage. *Angewandte Chemie International Edition*, 62(36), e202308436.
- Miao, N., Wang, J., Gong, Y., Wu, J., Niu, H., Wang, S., Li, K., Oganov, A. R., Tada, T., and Hosono, H. (2020). Computational Prediction of Boron-Based MAX Phases and MXene Derivatives. *Chemistry of Materials*, 32(16), Article 16.
- Mukherjee, S., Ren, Z., and Singh, G. (2018). Beyond Graphene Anode Materials for Emerging Metal Ion Batteries and Supercapacitors. *Nano-Micro Letters*, 10(4), 70.
- Nair, V. G., Birowska, M., Bury, D., Jakubczak, M., Rosenkranz, A., and Jastrzebska, A. M. (2022). 2D MBenes: A Novel Member in the Flatland. *Advanced Materials*, 34(23), Article 23.
- Nirjhar, A. R., Tan-Ema, S. J., Sahriar, M. A., Dipon, Md. N. A., Hasan Abed, Mohd. R., Shorowordi, K. Md., and Ahmed, S. (2024). Tuning the electrochemical performance of Cr₂B₂ MBene anodes for Li and Na-ion batteries through F and Cl-functionalization: A DFT and AIMD study. *Colloids and Surfaces A: Physicochemical and Engineering Aspects*, 684, 133194.

- Nzereogu, P. U., Omah, A. D., Ezema, F. I., Iwuoha, E. I., and Nwanya, A. C. (2022). Anode materials for lithium-ion batteries: A review. *Applied Surface Science Advances*, 9, 100233.
- Pang, J., Jin, W., Kuang, X., and Lu, C. (2023). Interlayer electronic coupling regulates the performance of FeN MXenes and Fe₂B₂ MBenes as high-performance Li- and Al-ion batteries. *Nanoscale*, 15(41), 16715–16726.
- Park, C.-M., Kim, J.-H., Kim, H., and Sohn, H.-J. (2010). Li-alloy based anode materials for Li secondary batteries. *Chemical Society Reviews*, 39(8), 3115–3141.
- Persson, K., Sethuraman, V. A., Hardwick, L. J., Hinuma, Y., Meng, Y. S., van der Ven, A., Srinivasan, V., Kostecki, R., and Ceder, G. (2010). Lithium Diffusion in Graphitic Carbon. *The Journal of Physical Chemistry Letters*, 1(8), 1176–1180.
- Sharma, D. K., Kumar, S., Laref, A., and Auluck, S. (2018). Mono and bi-layer germanene as prospective anode material for Li-ion batteries: A first-principles study. *Computational Condensed Matter*, 16, e00314.
- Shi, J., Yu, C., Kang, W., Xiao, X., and Sun, X. (2024). First-Principles Studies on Transition Metal Doped Mo₂B₂ as Anode Material for Li-Ion Batteries. *ChemistryOpen*, 13(8), e202300313.
- Stevens, D. A., and Dahn, J. R. (2001). The Mechanisms of Lithium and Sodium Insertion in Carbon Materials. *Journal of The Electrochemical Society*, 148(8), A803.
- Sun, X., Liu, X., Yin, J., Yu, J., Li, Y., Hang, Y., Zhou, X., Yu, M., Li, J., Tai, G., and Guo, W. (2017). Two-Dimensional Boron Crystals: Structural Stability, Tunable Properties, Fabrications and Applications. *Advanced Functional Materials*, 27(19), 1603300.
- Sun, Y., Li, K., Wang, B., Zhang, W., Wang, E., Zhou, J., and Sun, Z. (2024). Hexagonal Mg₂B₂ and Ca₂B₂ monolayers as promising anode materials for Li-ion and Na-ion batteries. *Nanoscale*, 16(33), 15699–15712.
- Sun, Y., Wang, G., Li, K., Peng, L., Zhou, J., and Sun, Z. (2023). Accelerating the Discovery of Transition Metal Borides by Machine Learning on Small Data Sets. *ACS Applied Materials & Interfaces*, 15(24), 29278–29286.
- Suriyakumar, S., Varma, A., Surendran, V., Jasuja, K., and Shaijumon, M. M. (2022). Nanosheets Derived through Dissolution-Recrystallization of TiB₂ as Efficient Anode for Sodium-Ion Batteries. *Batteries & Supercaps*, 5(2), e202100243.

- Tang, Q., Zhou, Z., and Shen, P. (2012). Are MXenes Promising Anode Materials for Li Ion Batteries? Computational Studies on Electronic Properties and Li Storage Capability of Ti_3C_2 and $Ti_3C_2X_2$ ($X = F, OH$) Monolayer. *Journal of the American Chemical Society*, 134(40), 16909–16916.
- Tarascon, J.-M., and Armand, M. (2001). Issues and challenges facing rechargeable lithium batteries. *Nature*, 414(6861), 359–367.
- Taylor, S. R. (1964). Abundance of chemical elements in the continental crust: a new table. *Geochimica et Cosmochimica Acta*, 28(8), 1273–1285.
- Tritsaris, G. A., Kaxiras, E., Meng, S., and Wang, E. (2013). Adsorption and Diffusion of Lithium on Layered Silicon for Li-Ion Storage. *Nano Letters*, 13(5), 2258–2263.
- Wang, F., Fan, X., Gao, T., Sun, W., Ma, Z., Yang, C., Han, F., Xu, K., and Wang, C. (2017). High-Voltage Aqueous Magnesium Ion Batteries. *ACS Central Science*, 3(10), 1121–1128.
- Wang, J., Bai, L., Wu, L., and Niu, L. (2022). Ordered double transition metal MBene: the hexagonal $ScTiB_2$ monolayer as a superior anode material for lithium-ion batteries. *Computational Materials Science*, 214, 111736.
- Wang, J., Ye, T.-N., Gong, Y., Wu, J., Miao, N., Tada, T., and Hosono, H. (2019). Discovery of hexagonal ternary phase Ti_2InB_2 and its evolution to layered boride TiB . *Nature Communications*, 10(1), 2284.
- Wang, S.-F., Wang, B.-T., Bo, T., Zhang, J.-R., and Wang, F.-W. (2021). Theoretical investigation of Ti_2B monolayer as powerful anode material for Li/Na batteries with high storage capacity. *Applied Surface Science*, 538, 148048.
- Wang, Y., Huang, R., Zhang, Q., Ma, Y., Gao, B., and Li, Z. (2023). Theoretical investigation of the V_2BX_2 ($X = S, Se, and Te$) monolayers as anode materials for Na-ion batteries. *Materials Today Communications*, 35, 105923.
- Wang, Y., Ma, N., Liang, B., and Fan, J. (2022). Exploring the potential of Ti_2BT_2 ($T = F, Cl, Br, I, O, S, Se$ and Te) monolayers as anode materials for lithium and sodium ion batteries. *Applied Surface Science*, 596, 153619.
- Wang, Y., Ma, N., Zhang, Y., Liang, B., Zhao, J., and Fan, J. (2023). S-functionalized 2D V_2B as a promising anode material for rechargeable lithium ion batteries. *Physical Chemistry Chemical Physics*, 25(5), Article 5.

- Wang, Y., Wang, S., Song, N., Wu, X., Xu, J., Luo, S., Xu, B., and Wang, F. (2024). On two-dimensional metal borides (MBenes) as anode materials for metal-ion batteries: A first-principles study. *Computational Materials Science*, *233*, 112710.
- Wei, F., Xu, S., Li, J., Yuan, S., Jia, B., Gao, S., Liu, G., and Lu, P. (2022). Computational Investigation of Two-Dimensional Vanadium Boride Compounds for Na-Ion Batteries. *ACS Omega*, *7*(17), Article 17.
- Wei, S., Lai, X., and Kale, G. M. (2023). Exploring the Potential of MBenes Supercapacitors: Fluorine-Free Synthesized $\text{MoAl}_{1-x}\text{B}$ with Ultrahigh Conductivity and Open Space. *ACS Applied Materials & Interfaces*, *15*(28), 33560–33570.
- Wu, L., Lu, P., Quhe, R., Wang, Q., Yang, C., Guan, P., and Yang, K. (2018). Stanene nanomeshes as anode materials for Na-ion batteries. *Journal of Materials Chemistry A*, *6*(17), 7933–7941.
- Xie, Y., Naguib, M., Mochalin, V. N., Barsoum, M. W., Gogotsi, Y., Yu, X., Nam, K.-W., Yang, X.-Q., Kolesnikov, A. I., and Kent, P. R. C. (2014). Role of Surface Structure on Li-Ion Energy Storage Capacity of Two-Dimensional Transition-Metal Carbides. *Journal of the American Chemical Society*, *136*(17), 6385–6394.
- Xiong, D., Li, X., Bai, Z., and Lu, S. (2018). Recent Advances in Layered $\text{Ti}_3\text{C}_2\text{Tx}$ MXene for Electrochemical Energy Storage. *Small*, *14*(17), 1703419.
- Xiong, D., Shi, Y., and Yang, H. Y. (2021). Rational design of MXene-based films for energy storage: Progress, prospects. *Materials Today*, *46*, 183–211.
- Xiong, W., Feng, X., Huang, T., Huang, Z., He, X., Liu, J., Xiao, Y., Wang, X., and Zhang, Q. (2025). Rapid synthesis of two-dimensional MoB MBene anodes for high-performance sodium-ion batteries. *Journal of Materials Science & Technology*, *212*, 67–76.
- Xiong, W., Feng, X., Xiao, Y., Huang, T., Li, X., Huang, Z., Ye, S., Li, Y., Ren, X., Wang, X., Ouyang, X., Zhang, Q., and Liu, J. (2022). Fluorine-free prepared two-dimensional molybdenum boride (MBene) as a promising anode for lithium-ion batteries with superior electrochemical performance. *Chemical Engineering Journal*, *446*, 137466.

- Xu, T., Wang, Y., Xiong, Z., Wang, Y., Zhou, Y., and Li, X. (2023). A Rising 2D Star: Novel MBenes with Excellent Performance in Energy Conversion and Storage. *Nano-Micro Letters*, 15(1), Article 1.
- Yabuuchi, N., Kubota, K., Dahbi, M., and Komaba, S. (2014). Research Development on Sodium-Ion Batteries. *Chemical Reviews*, 114(23), 11636–11682.
- Yang, E., Ji, H., and Jung, Y. (2015). Two-Dimensional Transition Metal Dichalcogenide Monolayers as Promising Sodium Ion Battery Anodes. *The Journal of Physical Chemistry C*, 119(47), 26374–26380.
- Yang, J., Li, R., Wang, J., Wen, J., Ye, J., Huang, G., Wang, J., and Pan, F. (2024). First-Principles Calculations of TiB₄ and TiB₅ as Anodes with High Capacity for Na-Ion Batteries. *Langmuir*, 40(28), 14540–14547.
- Yuan, G., Bo, T., Qi, X., Liu, P.-F., Huang, Z., and Wang, B.-T. (2019). Monolayer Zr₂B₂: A promising two-dimensional anode material for Li-ion batteries. *Applied Surface Science*, 480, 448–453.
- Yue Kuai, Chen, C., Elyas Abduryim, Shuli Gao, Wen Chen, Ge Wu, Liyuan Wu, Chao Dong, Weixia Zou, and Pengfei Lu. (2022). Two-Dimensional Metallic SnB Monolayer as an Anode Material for Non-lithium-ion Batteries. *Physical Chemistry Chemical Physics*.
- Z. Wang, Zizhao, W., Fan, S. W., Piao, H.-G., H.G. Piao, H.G. Piao, and Lu, Z. (2020). Monolayer Mo₂B: A non-magnetic metal and potential application as anode material for ion batteries and catalyst for hydrogen evolution. *Applied Surface Science*, 538, 148026.
- Zha, X.-H., Xu, P., Huang, Q., Du, S., and Zhang, R.-Q. (2020). Mo₂B, an MBene member with high electrical and thermal conductivities, and satisfactory performances in lithium ion batteries. *Nanoscale Advances*, 2(1), Article 1.
- Zhang, B., Zhou, J., Guo, Z., Peng, Q., and Sun, Z. (2020). Two-dimensional chromium boride MBenes with high HER catalytic activity. *Applied Surface Science*, 500, 144248.
- Zhang, H., Xiang, H., Dai, F., Zhang, Z., and Zhou, Y. (2018). First demonstration of possible two-dimensional MBene CrB derived from MAB phase Cr₂AlB₂. *Journal of Materials Science & Technology*, 34(11), Article 11.

- Zhang, T., Zhang, B., Peng, Q., Zhou, J., and Sun, Z. (2021). Mo₂B₂ MBene-supported single-atom catalysts as bifunctional HER/OER and OER/ORR electrocatalysts. *Journal of Materials Chemistry A*, 9(1), Article 1.
- Zhang, W., Li, L., Zhang, J., Liu, D., Wang, Q., Ren, J., Li, J., Guo, X., and Lu, X. (2024). Electrochemical performance of janus MoB as lithium-ion battery anode by bifunctional group O and S strategy. *Journal of Energy Storage*, 100, 113681.
- Zhang, Y., Lu, Q., Zhang, L., Zhang, L., Shao, G., and Zhang, P. (2024). Adjustable MXene-Based Materials in Metal-Ion Batteries: Progress, Prospects, and Challenges. *Small Structures*, 5(1), 2300255.
- Zhang, Y., Wu, Z.-F., Gao, P.-F., Zhang, S.-L., and Wen, Y.-H. (2016). Could Borophene Be Used as a Promising Anode Material for High-Performance Lithium Ion Battery? *ACS Applied Materials & Interfaces*, 8(34), 22175–22181.
- Zhao, S., Kang, W., and Xue, J. (2014). The potential application of phosphorene as an anode material in Li-ion batteries. *Journal of Materials Chemistry A*, 2(44), 19046–19052.
- Zhao, Y., Chen, D., Zheng, Y., and Sun, Y. (2024). Ab Initio Prediction and Characterization of TiB₂ as a Two-Dimensional Dirac Anode for Metal (Li/Na/Mg) Ion Batteries. *Energy & Fuels*, 38(17), 17064–17075.

CHAPTER III

RESEARCH METHODOLOGY

3.1 Overview

This chapter outlines the theoretical background and research methodology used to explore the potential of M_2B_2 MBene as anode materials for metal-ion batteries (MIBs). The study integrates density functional theory (DFT) calculations with machine learning (ML) techniques to pursue two main goals: (1) systematically screen M_2B_2 compounds across various compositions and crystal phases to suggest promising anode candidates, and (2) reveal key relationships between material features and anode-relevant properties using statistical and ML analyses.

Section 3.2 introduces the theoretical concepts of DFT and related computational techniques used to perform geometry optimization, phonon dispersion calculation, and transition state finding. These methods are central to computing the intrinsic and electrochemical properties of candidate materials.

Section 3.3 presents the ML approaches used to construct descriptive models and extract insights into the relationships between material descriptors and anode properties.

Section 3.4 summarizes the complete computational workflow, combining DFT and ML methods to meet the research objectives.

3.2 Density Functional Theory (DFT)

Density Functional Theory (DFT) is a powerful computational approach based on quantum mechanics for modelling materials at the atomic level. In materials science community, it has become a standard approach to describe materials properties such as electronic, optic, energetic, and magnetic character, which are dominated by behaviour of electrons. The propose of this section is to provide a brief overview of the fundamental concepts underlying DFT. The content presented here is

primarily summarized from a textbook by Sholl and Steckel (Sholl and Steckel, 2009). The more in-depth theoretical details are encouraged to consult the reference textbook or other comprehensive DFT resources.

3.2.1 Many-body problems in material systems

In quantum mechanics, the fundamental behaviour of a material system, e.g., containing N interacting electrons and M nuclei, is governed by the time-independent Schrodinger equation:

$$\hat{H}\psi(r_1, \dots, r_N) = E\psi(r_1, \dots, r_N).$$

The total Hamiltonian (\hat{H}) includes the kinetic energy of electrons and nuclei, the Coulomb interaction between all particles, and the external potential arising from the nuclei. Solving this system exactly is infeasible due to the complexity of the many-body wavefunction, which exists in a $3N$ -dimensional space for N electrons. To make the problem tractable while retaining reasonable accuracy, several well-established approximations are employed to reduce its computational complexity.

The Born-Oppenheimer approximation (Born and Oppenheimer, 1927) decouples nuclear and electronic motions by assuming that nuclei move much more slowly than electrons. This separation allows us to first solve the problem of electron motion for fixed positions of the nuclei, finding the lowest energy configuration or ground state of the electrons. This ground state energy as a function of the nuclei's positions, is called the adiabatic potential energy surface.

3.2.2 Concept of density functional theory

The field of DFT is built on two fundamental mathematical theorems known as Hohenberg-Kohn theorems (Hohenberg and Kohn, 1964). The first theorem states that “*the ground-state energy from the Schrodinger equation is a unique functional of the electron density*”. This establishes that all ground-state properties, including energy and wavefunction, are determined entirely by electron density. This theorem significantly reduces the complexity of the problem by shifting the focus from the many-body wavefunction, which depends on $3N$ variables, to the electron density, which depends only on three spatial coordinates. The second theorem states that

“The electron density that minimizes the energy of the overall functional is the true electron density corresponding to the full solution of the Schrodinger equation.” If the exact functional were known, the ground-state energy and corresponding electron density could be found variationally by minimizing this functional.

While the Hohenberg-Kohn theorems establish the existence of a functional that maps electron density to energy, they say nothing about what the functional is. To make the theory computationally practical, Kohn and Sham (Kohn and Sham, 1965) introduced a framework by mapping the original interacting many-electrons system to a fictitious system of non-interacting electrons that experience an effective potential. The set of equations for non-interacting electrons is so called Kohn-Sham equation:

$$\left[-\frac{\hbar^2}{2m}\nabla^2 + V_{eff}[\mathbf{n}(\mathbf{r})] \right] \psi_i^{KS}(\mathbf{r}) = \epsilon_i \psi_i^{KS}(\mathbf{r})$$

where $\psi_i^{KS}(\mathbf{r})$ are the single-electron wave functions (often called Kohn-Sham orbitals). The i is the band index (in general, the value of i is ranged from one to the number of occupied electron bands which is equal to a half of the total number of electrons). And ϵ_i is the corresponding energy of band index i . Note that these single-electron wave functions depend on only three spatial variables. The crucial part is the effective potential, $V_{eff}[\mathbf{n}(\mathbf{r})]$, which is constructed such that the ground state density obtained from these non-interacting orbitals is the same as the ground state density of original interacting many-electrons system. The $V_{eff}[\mathbf{n}(\mathbf{r})]$ consists of three main terms:

1. $V_{ext}[\mathbf{n}(\mathbf{r})]$: The potential due to the interaction between an electron and the atomic nuclei, which also appeared in the full Schrodinger equation.
2. $V_H[\mathbf{n}(\mathbf{r})]$: The Hartree potential, which accounts for Coulomb repulsion between electron being considered and the total electron density defined by all electrons in the problem.

$$V_H[\mathbf{n}(\mathbf{r})] = \frac{1}{2} \int \frac{n(\mathbf{r}')}{|\mathbf{r} - \mathbf{r}'|} d\mathbf{r}'$$

The Hartree potential includes an unphysical self-interaction, where an electron interacts with its own contribution to the total density.

3. $V_{xc}[\mathbf{n}(\mathbf{r})]$: The exchange-correlation potential, which incorporates all the quantum mechanical effects not captured by the nuclear and Hartree potentials, namely exchange and correlation contribution including unknown contribution. It is formally defined as the functional derivative of the exchange–correlation energy functional with respect to the electron density:

$$V_{xc}[\mathbf{n}(\mathbf{r})] = \frac{\delta E_{xc}[\mathbf{n}(\mathbf{r})]}{\delta n}$$

3.2.3 Exchange-correlation energy functional

A central complication in DFT is that the exact form of the exchange-correlation energy functional $E_{xc}[\mathbf{n}(\mathbf{r})]$ is unknown. Practical DFT calculations rely on approximations for $E_{xc}[\mathbf{n}(\mathbf{r})]$. The development of functionals that better represent nature remains an active research area. Two common classes of approximations are the Local Density Approximation (LDA) and the Generalized Gradient Approximation (GGA). LDA treats the exchange-correlation energy as a function of electron density, assuming homogeneous electron gas. In contrast, GGA improves accuracy for inhomogeneous systems by incorporating the gradient of electron density term. In this thesis, the Perdew–Burke–Ernzerhof (PBE) functional—a widely adopted GGA model—is used throughout all DFT calculations. PBE offers a good balance between computational efficiency and accuracy, especially for solid-state system. The formal definition and derivation of the PBE functional can be found in (Perdew et al., 1996).

3.2.4 Self-consistent field method

The Kohn–Sham equations are intrinsically self-consistent, as the effective potential $V_{eff}[\mathbf{n}(\mathbf{r})]$ depends on the electron density $\mathbf{n}(\mathbf{r})$, which is itself constructed from the Kohn–Sham orbitals $\psi_i(\mathbf{r})$. This circular dependency is resolved through an iterative process known as the Self-Consistent Field (SCF) method, which gradually refines the electron density until convergence is achieved. The overall SCF procedure is illustrated in **Figure 3.1**, highlighting the iterative loop used to obtain the ground-state electron density and total energy. This includes:

1. Set initial electron density $\mathbf{n}(\mathbf{r})$: Begin with a trial density, typically obtained from a superposition of atomic electron densities.

2. Construct effective potential $V_{eff}[\mathbf{n}(\mathbf{r})]$: Calculate the Hartree potential $V_H[\mathbf{n}(\mathbf{r})]$, the external potential $V_{ext}[\mathbf{n}(\mathbf{r})]$, and the exchange–correlation potential $V_{xc}[\mathbf{n}(\mathbf{r})]$ based on the current electron density.
3. Solve the Kohn–Sham equations: Use the effective potential to solve the Kohn–Sham equations and obtain a set of single-particle wavefunctions $\psi_i(\mathbf{r})$.
4. Calculate new electron density $\mathbf{n}'(\mathbf{r})$: Generate an updated electron density from the computed wavefunctions.
5. Check for convergence: Compare the new electron density $\mathbf{n}'(\mathbf{r})$ with the previous one $\mathbf{n}(\mathbf{r})$. If the densities are sufficiently close (within a specified tolerance), convergence is achieved.
6. If not converged, mix densities and repeat: Combine the previous and current densities to form a new trial density and return to step 2.
7. Once converged, compute total energy and properties: Use the self-consistent ground-state density to calculate the total energy, atomic forces, and other properties of interest.

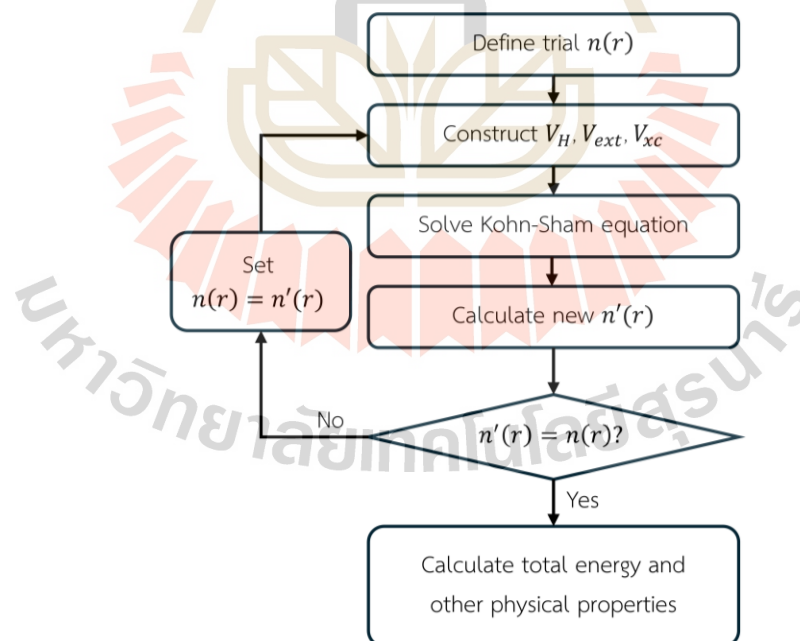


Figure 3.1 The scheme of self-consistent field iterations for solving the Kohn-Sham equation and obtaining total energy and other physical properties.

3.2.5 Pseudopotentials

In plane-wave-based DFT calculations, accurately describing the behavior of tightly bound core electrons poses a significant computational challenge. These core states exhibit rapid oscillations near the nucleus, which require an extremely large number of plane waves to represent properly. This drastically increases the computational cost. However, since chemical bonding and most material properties are governed primarily by the valence electrons, the core electrons can be treated using an effective approximation. This approach is known as the pseudopotential method, and it is based on the frozen-core approximation, where the core electrons are considered inert and their influence is incorporated into an effective potential acting on the valence electrons.

A pseudopotential replaces the strong nuclear potential and the core electron contributions with a smoother potential that simplifies the resulting wavefunctions. As shown in **Figure 3.2**, the true wavefunction ψ and the exact potential V exhibit rapid oscillations near the nucleus (i.e., for distances $r < r_c$, where r_c is the cutoff radius), while the pseudo-wavefunction ψ_{pseudo} and pseudopotential V_{pseudo} are constructed to be smooth and computationally efficient. Importantly, both the potential and wavefunction are required to match their all-electron counterparts beyond the cutoff radius ($r \geq r_c$) to ensure physical accuracy.

To be effective, a pseudopotential should satisfy several key criteria:

1. **Consistency:** The pseudo and exact wavefunctions and potentials must coincide beyond the cutoff radius.
2. **Smoothness:** The pseudo-wavefunction should eliminate strong oscillations within the core region to reduce basis set requirements.
3. **Transferability:** The pseudopotential must accurately reproduce valence behavior across different chemical environments.
4. **Continuity:** The pseudo and real wavefunctions must be continuous at $r = r_c$.
5. **Charge preservation:** The pseudo-wavefunction should retain the same charge distribution as the real wavefunction within the cutoff region.
6. **Relativistic corrections:** For heavier elements, relativistic effects should be incorporated into the pseudopotential generation.

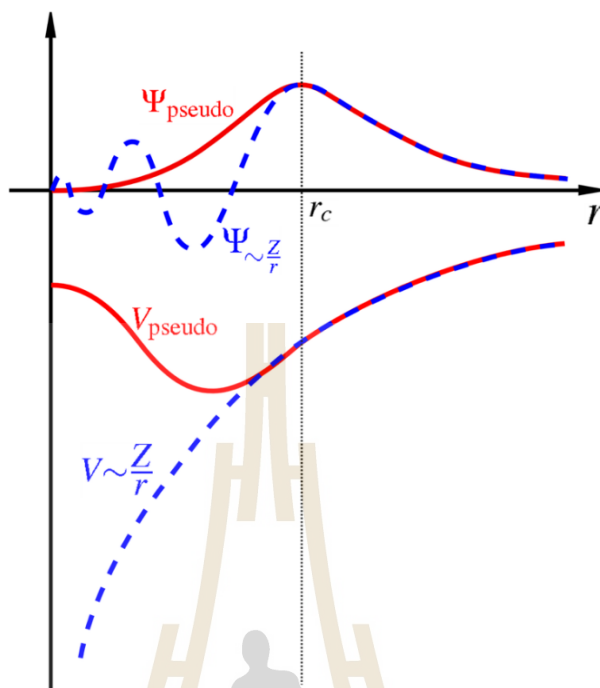


Figure 3.2 Schematic illustration of a real (blue) and a pseudo (red) potential and their corresponding wavefunctions. The cutoff radius r_c is the position where both values are matched (Payne et al., 1992).

In this thesis, we employed projector-augmented wave method (Blöchl, 1994; Kresse and Joubert, 1999) that retains near all-electron accuracy by reconstructing the full wavefunction in the core region from a pseudo-wavefunction and a set of atom-centered projectors. The projector-augmented wave method has become widely adopted in modern DFT codes due to its combination of accuracy and efficiency.

3.2.6 Dispersion correction: DFT-D3

Conventional DFT methods are known to underestimate long-range van der Waals (vdW) or dispersion interactions, which arise from correlated fluctuations in electron density. These weak and non-covalent interactions play a critical role in systems such as molecules, surface adsorption, and layered materials. Accurate treatment of dispersion typically requires high-level wavefunction-based methods that explicitly account for long-range electron correlation. However, the standard exchange-correlation functionals cannot capture this vdW interaction reliably, often leading to errors in predicted structures and binding energies.

To address the limitations of conventional DFT in capturing long-range dispersion interactions, several correction schemes have been developed. Among them, the DFT-D3 method, introduced by Grimme and co-workers (Grimme et al., 2010, 2011), is one of the most widely adopted due to its balance of accuracy and computational efficiency. DFT-D3 improves upon earlier approaches (DFT-D and DFT-D2) by adding a semi-empirical dispersion energy term to the total DFT energy. This correction accounts for pairwise interactions between atoms, enabling more reliable predictions across a broad range of systems e.g., from isolated molecules to periodic solids. The corrected total energy is given by:

$$E_{DFT-D3} = E_{DFT} + E_{disp}$$

$$E_{dis} = - \sum_{i < j} \sum_{n=6,8} \frac{C_n^{ij}}{R_{ij}^n} f_{damp}(R_{ij})$$

where R_{ij} is the interatomic distance between atom i and j . C_n^{ij} are dispersion coefficients (C_6 and C_8) that depend on the atomic species and their chemical environments. And $f_{damp}(R_{ij})$ is a damping function that smoothly attenuates short-range interactions to prevent double counting of electron correlation effects already included in the main functional. The damping function is expressed as:

$$f_{damp}(R_{ij}) = 1 - \exp\left(-\alpha(R_{ij} - R_s)^2\right)$$

where α is a damping parameter that controls the rate of decay and R_s is a cutoff radius beyond which the correction becomes negligible.

A key feature of DFT-D3 is the environment-dependent calculation of dispersion coefficients using fractional coordination numbers, which enhances accuracy and transferability across diverse bonding environments. It is computationally efficient and straightforward to implement in plane-wave DFT codes. It is broadly compatible with many exchange–correlation functionals, including PBE. In this thesis, DFT-D3 corrections are applied throughout the computational screening of MBenes to better capture metal carrier adsorption phenomena.

3.2.7 Geometry optimization

Geometry optimization is a procedure to find the lowest-energy structure of a system by minimizing its total energy with respect to atomic positions, i.e., the local minimum on potential energy surface. This corresponds to the equilibrium structure where the net forces on all atoms are ideally zero. In the context of DFT calculations, this is achieved by iteratively updating the positions of atoms until the net forces acting on them fall below a predefined threshold, indicating that the system has reached a local minimum. The forces acting on each atom are calculated based on the Hellmann–Feynman theorem (Feynman, 1939), which allows the force F_i on atom i to be evaluated directly from the DFT total energy as:

$$F_i = -\frac{\partial E_{tot}}{\partial R_i}$$

A typical geometry optimization process involves two nested loops: an inner SCF iteration for converging the electron density and an outer ionic relaxation loop for updating atomic configurations. The procedure is outlined schematically in **Figure 3.3**.

1. Start by specifying the initial geometry of the atomic structure, including atomic positions. This serves as the starting point for optimization.
2. Based on the initial configuration, initiate a trial electron density $n(\mathbf{r})$. This density is used to construct the effective potential $V_{eff} = V_H + V_{ext} + V_{xc}$. The Kohn–Sham equations are solved self-consistently to obtain a new electron density and repeated iteratively until convergence is achieved.
3. Once the electron density is converged, the Hellmann–Feynman forces F_i acting on each atom are computed using the resulting ground-state electron density.
4. Compare the magnitude of each atomic force F_i against a predefined force threshold F_{tol} (e.g., 0.01 eV/Å).
 - If all $F_i \leq F_{tol}$, the geometry is considered optimized, and the process terminates.
 - If any $F_i > F_{tol}$, proceed to the next step.

5. Adjust the atomic positions in the direction that minimizes the forces F_i . This is typically done using a gradient-based optimization algorithm, such as the conjugate gradient algorithm. These methods use information about the energy gradients to efficiently find the nearest local energy minimum.
6. After updating the atomic positions, a new SCF calculation is initiated for the updated geometry. Steps 2–5 are repeated until all atomic forces fall below the force threshold F_{tol} , resulting in an optimized configuration.

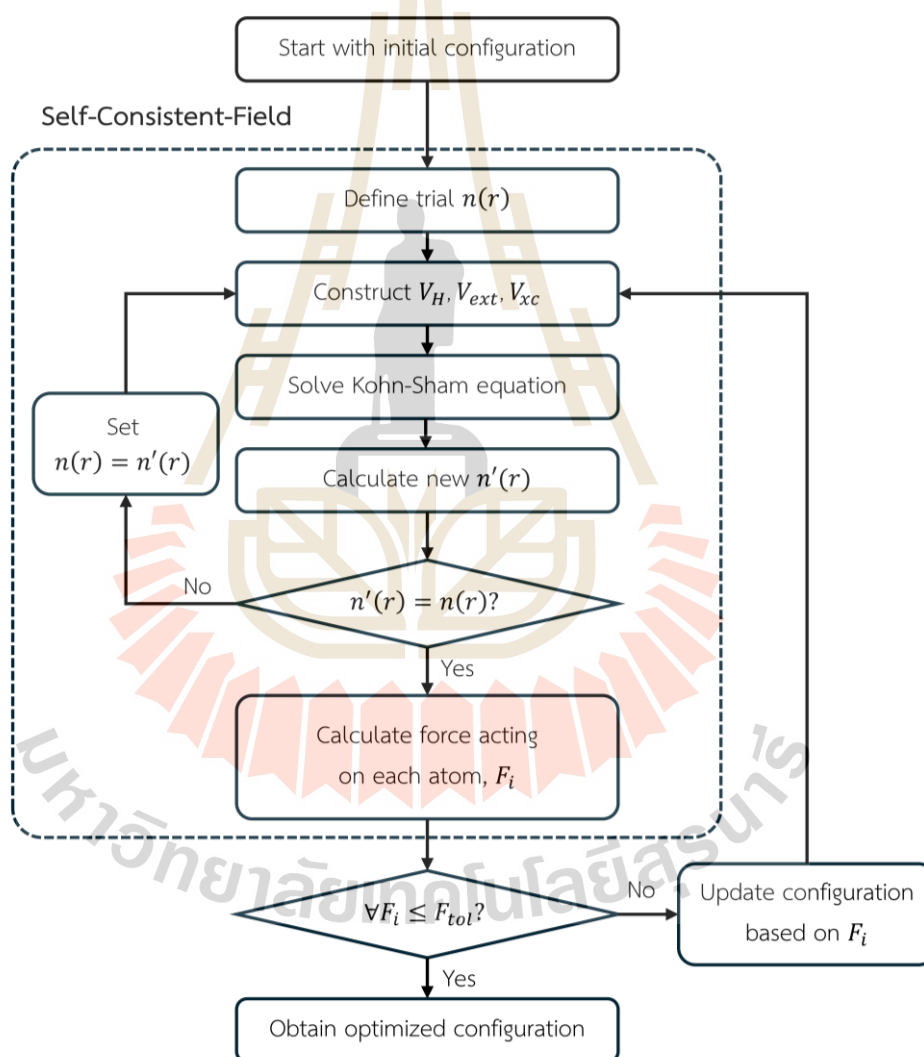


Figure 3.3 The scheme of configuration updating iterations for geometry optimization.

3.2.8 Phonon dispersion calculation

Phonon dispersion calculation is a fundamental tool for analyzing the vibrational and dynamical properties of crystalline solids. Phonons or quantized modes of lattice vibrations also determine thermal conductivity, heat capacity, and electron–phonon interactions of the material. In this thesis, phonon analysis was used to assess dynamical stability of crystal structures. The presence of imaginary frequencies (commonly plotted as negative values) in the phonon bandstructure plot indicates soft vibrational modes, which may lead to structural instabilities, lattice distortions, or phase transitions at 0 K.

Phonon calculations were carried out using finite displacement method, also known as the supercell method, as implemented in the open-source package Phonopy (Togo, 2023). The procedure begins by generating a periodic supercell, formed by repeating the primitive unit cell to account for long-range atomic interactions. Small displacements (typically ~ 0.01 Å) are then applied to atoms along coordinate directions. The resulting forces on all atoms are computed using DFT. These forces are used to numerically derive the interatomic force constants via finite differences. Finally, the dynamical matrix is constructed in reciprocal space and diagonalized at selected points to obtain the phonon dispersion curves and vibrational eigenmodes.

3.2.9 Climbing image nudged elastic band (CI-NEB) method

The climbing-image nudged elastic band (CI-NEB) method is a computational technique used to determine the minimum energy path (MEP) between two stable configurations, i.e., between the initial and final state of a diffusion or reaction process (Henkelman et al., 2000). In the context of battery materials, CI-NEB is widely employed to estimate the diffusion barrier of carrier species atom across electrode surface or within bulk electrodes. These barriers provide insight into the ionic conductivity and rate performance of electrode materials.

The standard nudge elastic band (NEB) method begins by interpolating a series of intermediate configurations, or images, between the initial and final states. These images are connected by artificial spring forces to form an elastic band, ensuring even spacing along the diffusion path. During the optimization process, the total force on each image is decomposed into two components: (i) the true interatomic force acting

perpendicular to the path, which guides the image toward the MEP, and (ii) the spring force acting along the path, which maintains uniform image spacing. The NEB optimization converges once the perpendicular forces on all intermediate images fall below a predefined threshold (e.g., 0.05 eV/\AA), yielding an approximate MEP. To ensure that one of the images is placed at the transition state, the CI-NEB method drives the highest-energy image uphill by removing its spring forces, allowing it to climb directly to the saddle point. The energy barrier is determined from the saddle point.

3.3 Machine learning

Machine learning (ML) is a subfield of artificial intelligence that enables computer algorithms to automatically learn patterns from data and make predictions or decisions without being explicitly programmed. In recent years, ML has become an essential tool across various domains, including materials science, where it accelerates the discovery and optimization of functional materials by capturing complex and non-linear relationships between input features and target properties.

ML problems are typically classified into two main categories: supervised and unsupervised learning. In supervised learning, the model is trained on labeled data, where both input features and corresponding target values are known. This category is further divided into regression and classification tasks. Regression focuses on predicting continuous numerical values, whereas classification involves assigning inputs into discrete categories. In this thesis, we focus exclusively on supervised regression tasks, aiming to predict continuous material properties relevant to anode performance.

The purpose of this section is to introduce the fundamental concepts of machine learning regression as applied in this thesis. Special attention is given to the concept of explainability for machine learning models, which plays a crucial role in scientific research where interpretability and physical understanding are essential. Rather than treating ML as a black box, these methods enable us to extract insights from trained models, helping to identify key descriptors that govern material performance. This aligns with the second objective of this thesis: to uncover meaningful structure–property relationships that can guide the rational design of high-performance MBenes for MIB anodes.

3.3.1 Regression models

Regression analysis is a fundamental approach that focuses on modelling the relationship between a continuous dependent variable (target) and one or more independent variables (features or descriptors). The ultimate goal is to learn a function that maps features to target, enabling accurate predictions for unseen data or uncovering hidden features-target relationships.

In supervised learning, regression models are trained on a dataset containing known features-target pairs. The model learns the underlying relationships by minimizing a loss function, such as mean absolute error (MAE), which quantifies the difference between predicted and actual values. After the training process, the model performance is evaluated using accuracy metrics such as mean absolute error (MAE), root mean squared error (RMSE) and R-squared (R^2), which together they assess prediction error and goodness of fit of the model. The choice of regression algorithm significantly affects model flexibility, interpretability, and robustness to overfitting. In this thesis, several regression models were explored, including linear regression, decision tree, and ensemble tree-based methods including random forest, gradient boosting, and XGBoost. **Figure 3.4** illustrates the conceptual mechanisms of linear regression, decision tree, random forest, and gradient boosting; XGBoost, built upon gradient boosting with additional enhancements, is not shown.

Linear regression is the simplest form of regression that assumes a linear relationship between the input features and the target output. It models the target output y as a weighted sum of the input features x_1, x_2, \dots, x_n , plus an intercept term. The mathematical form is:

$$y = \beta_0 + \beta_1 x_1 + \beta_2 x_2 + \dots + \beta_n x_n + \epsilon$$

where β_i are the coefficients and ϵ is the error term. These coefficients are typically estimated using the ordinary least squares (OLS) method, which minimizes the sum of squared residuals. Despite its simplicity, linear regression offers high interpretability and is useful for establishing baseline trends or identifying linear dependencies between features and target.

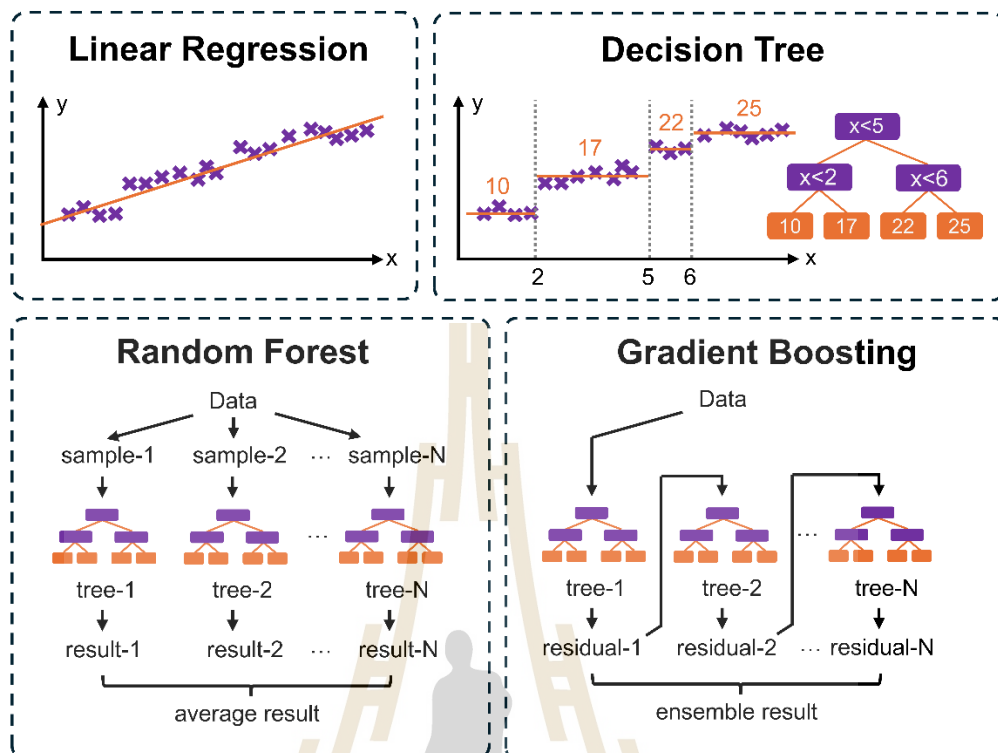


Figure 3.4 Illustration of regression model concepts: linear regression, decision tree, random forest, and gradient boosting, each showing how model builds predictions from data.

Decision tree regression is a non-parametric method that partitions the feature space into regions by recursively splitting the data according to feature thresholds. At each split, the algorithm selects the feature and threshold that minimizes loss metric with each resulting subset. Predictions are made by averaging the target values for all data points within each terminal subset (leaf node). The resulting model is interpretable as a set of conditional rules, but decision trees are prone to overfitting unless pruning techniques or maximum depth constraints are applied.

Random forest (Breiman, 2001) is an ensemble method that mitigates the overfitting tendency of individual decision trees by aggregating predictions from many independently trained trees. Each decision tree is trained on a bootstrap sample of data and uses a random subset of features at each split (bagging and feature sampling). The final prediction is typically the average of predictions from all trees. Random forests are robust to noise and perform well across a wide range of problems, though interpretability is reduced compared to a single decision tree.

Gradient boosting (Friedman, 2001) is another ensemble method that constructs decision trees sequentially, with each new tree trained to minimize the residual errors of the current ensemble. Unlike random forests, where trees are trained independently, gradient boosting iteratively refines the model by correcting the mistakes of its predecessors. Each tree is trained on the gradient of the loss function with respect to the prediction, and a learning rate controls how much each tree contributes to the final output. Gradient boosting often outperforms bagging methods in accuracy but is more sensitive to hyperparameter tuning and prone to overfitting if not regularized properly.

XGBoost (Extreme Gradient Boosting) (Chen and Guestrin, 2016) is an optimized and scalable implementation of gradient boosting that incorporates algorithmic enhancements and system-level optimizations. It includes regularization terms (L1 and L2) in the objective function to control model complexity and improve generalization. XGBoost also uses second-order gradient information (i.e., both gradients and Hessians) to speed up convergence, supports sparse data handling, and allows parallel computation during tree construction. These innovations make XGBoost highly efficient and accurate, particularly in high-dimensional, noisy, or imbalanced datasets.

3.3.2 Model evaluation

To assess the predictive performance of regression models, several standard metrics are used to quantify the discrepancy between predicted and actual values:

Mean Absolute Error (MAE) quantifies the average magnitude of prediction errors, providing a straightforward interpretation in the same units as the output target:

$$\text{MAE} = \frac{1}{n} \sum_{i=1}^n |y_i - \hat{y}_i|$$

Root Mean Squared Error (RMSE) penalizes larger errors more than MAE by squaring the residuals before averaging and then taking the square root:

$$\text{RMSE} = \sqrt{\frac{1}{n} \sum_{i=1}^n (y_i - \hat{y}_i)^2}$$

Coefficient of determination (R^2) evaluate the proportion of variance in the target output explained by the model, defined as:

$$R^2 = 1 - \frac{\sum_{i=1}^n (y_i - \hat{y}_i)^2}{\sum_{i=1}^n (y_i - \bar{y})^2}$$

In these equations: y_i is the actual observed value, \hat{y}_i is the predicted value of the regression model and \bar{y} is the average of all actual observed values, and n is the total numbers of data points. MAE reflects the average performance, while RMSE emphasizes the impact of large errors. R^2 provides a relative measure of model fit, with the value closer to 1 indicating better explanatory power.

3.3.3 Model interpretation

As ML models become increasingly integrated into scientific research, interpretability has become a critical concern, especially in materials science, where understanding the rationale behind a prediction is often as important as the prediction itself (Linardatos et al., 2021). In conventional regression tasks, model performance is often typically evaluated using metrics such as MAE, RMSE, or R^2 . While these metrics assess predictive accuracy, they offer no insight into the internal logic of the model. This black-box nature limits trust, hinders generalizability, and reduces the scientific value of many ML applications (Hassija et al., 2024).

Interpretable ML addresses this challenge by providing explanations for how features influence a model's prediction. These explanations are vital in scientific contexts, where model-derived insights must align with established domain knowledge or reveal new interpretable patterns that guide future experiments. Interpretable ML enables researchers to go beyond pure prediction and uncover the structure–property relationships that govern material behavior.

Some models are naturally interpretable by design. For example, decision trees offer transparency through a hierarchical set of rules that lead to each prediction and Linear regression, for instance, offers explicit coefficients for each feature, making it straightforward to quantify how each input contributes to the output. **Figure 3.5** illustrates two such examples: a decision tree and a linear model trained to predict

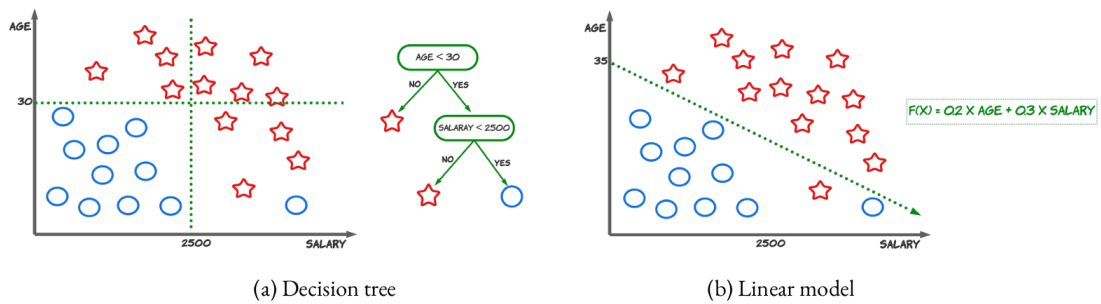


Figure 3.5 Illustration of (a) a decision tree and (b) a linear model used to predict loan approval outcomes based on applicant age and salary. Red stars indicate approved loan, while blue circles represent rejected applications (Delaunay, 2023).

loan approval based on applicant age and salary. In the decision tree (panel a), the decision path is explicit, young applicants with salaries below a certain threshold are rejected. In the linear model (panel b), the relative importance of age and salary is visible through the size of their respective coefficients (Delaunay, 2023). These models are useful not only because they make predictions, but because they do so in a way that is understandable to human users.

However, not all models provide this level of transparency. Ensemble methods like random forests, gradient boosting, and XGBoost aggregate the decisions of many individual models—often hundreds of decision trees—making it extremely difficult to understand how any single feature affects a particular prediction. Although these models offer strong predictive performance, they sacrifice interpretability. In many applications, such as energy materials design, medicine, or policy-making, deploying a highly accurate but opaque model can lead to missed insights, reduced trust, and ultimately suboptimal or even risky decisions.

To interpret black-box models, researchers often turn to post-hoc explanation techniques, which are applied after a complex model has been trained. These techniques aim to elucidate the model's decision-making process by analyzing the relationship between input features and output target predictions, typically by estimating how changes in individual features influence the predicted outcome. The most widely used post-hoc methods includes LIME (Local Interpretable Model-Agnostic Explanations) (Ribeiro et al., 2016), which approximates the complex model

locally around a specific prediction using a simple surrogate model such as linear regression or a shallow decision tree. Another widely used method is SHAP (Shapley Addition exPlanations) (Lundberg and Lee, 2017), which is the primary interpretability tool employed in this thesis and will be discussed in the following section.

3.3.4 SHAP technique

SHAP (SHapley Additive exPlanations) is a widely used technique to interpret ML model predictions by attributing the contribution of each feature to a specific prediction. Its foundation lies in cooperative game theory, specifically the concept of Shapley values developed by Lloyd Shapley. The main idea is to treat the model output as a “payout” that needs to be fairly distributed among the input features, which are considered as “players” in a game. SHAP provides an approach to assign credit to each feature, answering the question: “How much did each feature contribute to this prediction?”

To build an intuition for how SHAP works, consider a simple model that predicts house prices using two features: number of bedrooms and floor area. Suppose the baseline model output (i.e., average predicted price) is \$300,000. If using only the number of bedrooms increases the predicted price to \$400,000, and using only the floor area raises it to \$500,000, while using both together leads to \$600,000, SHAP would assign \$100,000 to the number of bedrooms and \$200,000 to the floor area. These values represent each feature's marginal contribution and add up to the total prediction increase of \$300,000. This example highlights how SHAP explains the output by decomposing the prediction into additive contributions from each input feature.

Mathematically, SHAP values for a feature j in an instance x to the prediction output are defined as:

$$\phi_j = \sum_{S \subseteq N \setminus \{j\}} \frac{|S|! (|N| - |S| - 1)!}{|N|!} [f_{S \cup \{j\}}(x) - f_S(x)]$$

- N is the full set of all features (i.e., feature index), for example $N = \{1, 2, \dots, p\}$ if the model has p features.
- $\{j\}$ is the set containing only the feature j the one which are calculating SHAP value.

- $\mathcal{S} \subseteq N \setminus \{j\}$ are all possible subsets of features excluding feature j . For each subset \mathcal{S} , we assess the contribution of adding feature j to that subset.
- $|\mathcal{S}|$ is the number of elements (features) in the subset \mathcal{S} .
- \mathcal{S} is a subset of features that does not contain j ,
- $f_{\mathcal{S}}(\mathbf{x})$ is the model output (prediction) when only the features in subset \mathcal{S} are known (i.e., other features are ‘unknown’ or marginalized out).
- $f_{\mathcal{S} \cup \{j\}}(\mathbf{x})$ is the model output when features in \mathcal{S} and also j are known.
- $f_{\mathcal{S} \cup \{j\}}(\mathbf{x}) - f_{\mathcal{S}}(\mathbf{x})$ is the marginal contribution of features j when added to subset \mathcal{S} .
- $\frac{|\mathcal{S}|!(|N|-|\mathcal{S}|-1)!}{|N|!}$ is a weighting term (Shapley weight), which ensures fairness by averaging over all possible feature orders. The weights depend on the size of \mathcal{S} and total number of features $|N|$.

This formula computes the average marginal contribution of feature j across all possible subsets of other features. The weighting term ensures fair attribution by considering the number of subsets a feature can appear in. SHAP values satisfy desirable properties such as efficiency (the sum of SHAP values equals the prediction difference from baseline), symmetry, and additivity, making them theoretically sound for feature attribution (Lundberg and Lee, 2017).

In practice, calculating exact SHAP values requires evaluating the model on all 2^N subsets of features, which becomes computationally infeasible for large N . Therefore, approximation methods are employed. For tree-based models, an efficient algorithm known as TreeSHAP enables exact SHAP value computation in polynomial time. For model-agnostic applications, methods such as KernelSHAP use Monte Carlo sampling to estimate SHAP values without relying on internal model structure.

While SHAP values are primarily used to explain individual predictions (local interpretability), they can be aggregated across many samples to evaluate global feature importance. This is typically done by computing the mean absolute SHAP value of each feature over the dataset:

$$\text{SHAP importance} = \frac{1}{M} \sum_{j=1}^M |\phi_{ij}|$$

This measure reflects how strongly feature j influences model predictions across the dataset, regardless of direction. It provides an intuitive, model-agnostic metric of global importance, enabling comparisons across different models or datasets.

In addition to numerical summaries, SHAP values can be visualized in multiple ways. Summary plots show feature rankings and distributions of SHAP values. Dependence plots reveal how SHAP values change with feature values, uncovering nonlinear trends or interactions. Force plots offer a breakdown of how each feature pushes the prediction above or below the baseline for a single instance.

In summary, SHAP offers a robust framework to explain both individual predictions and global model behavior. By decomposing model outputs into additive feature contributions, SHAP enhances interpretability, helping researchers understand how complex models make decisions, which is an essential step for transparent and trustworthy machine learning in scientific research.

3.4 Research methodology

3.4.1 Workflow

This section presents the computational methodology used to evaluate the electrochemical performance of M_2B_2 as anode materials for MIBs and to uncover material-property relationships. The workflow integrates DFT and interpretable ML into a framework for property prediction and feature analysis. The computational setup and model configurations for DFT calculations are detailed in Section 3.4.2. These DFT calculations were employed to optimize M_2B_2 structures for each composition and lattice phase, and to compute their intrinsic and anode-relevant properties, as described in Section 3.4.3. The resulting dataset enabled comparison of properties across different candidates, facilitating the identification of promising anode materials for various MIB systems. The representation of M_2B_2 systems using material features is presented in Section 3.4.4. Section 3.4.5 describes how interpretable ML models were used to uncover relationships between material features and anode properties. Together, these components form an integrated methodology for both predictive modeling and scientific interpretation of MBenes in the context of MIB applications.

3.4.2 Computational setup and model

All periodic model calculations in this thesis were done using DFT as implemented in Vienna Ab initio Simulation Package (VASP) (Kresse and Furthmüller, 1996a, 1996b; Kresse and Hafner, 1993). The projector-augmented wave method was employed to describe the core-valence interactions (Blöchl, 1994; Kresse and Joubert, 1999), using pseudopotentials based on the Perdew-Burke-Ernzerhof (PBE) exchange-correlation functional within the generalized gradient approximation (GGA) (Perdew et al., 1996). Minimal pseudopotentials were selected for all elements for fast screening. A plane-wave basis set with an energy cutoff of 500 eV was used to expand valence electron wavefunctions. Long-range dispersion interactions, particularly important for adsorption of carrier species on MBene surface, were accounted for using the DFT-D3 method of Grimme (Grimme et al., 2010). Electronic SCF convergence was set to 10^{-6} eV, and geometry optimizations were carried out with a convergence criterion of 0.01 eV/Å for residual atomic forces. Brillouin zone sampling used a Γ -centered $7 \times 7 \times 1$ Monkhorst-Pack k -point mesh (Monkhorst and Pack, 1976).

M_2B_2 MBene were modeled as a periodic monolayer using a 2×2 supercell, consisting of eight transition metal (M) and eight boron (B) atoms. Four crystal phases were examined: orthorhombic, hexagonal, trigonal, and tetragonal. A vacuum spacing of at least 20 Å was applied along the z-direction to eliminate spurious interlayer interactions. Initial geometries for Mo_2B_2 in all phases were reproduced from the literature (Bo et al., 2019) and used as templates. For other M_2B_2 , the desired metal element was introduced by substituting Mo atoms, followed by full relaxation of lattice parameters and atomic positions. For each composition, multiple magnetic configurations were tested, and the lowest-energy spin state was selected for further calculations.

Pre- and post-processing were facilitated using VASPKIT (Wang et al., 2021) and the Atomic Simulation Environment (ASE) (Larsen et al., 2017). Structural visualization were generated using the VESTA software package (Momma and Izumi, 2011).

3.4.3 Calculated material properties

This section describes how key intrinsic and anode-relevant properties of M_2B_2 monolayers were computed using DFT methods. These properties include structural

stability, electronic conductivity, theoretical capacity, OCV, and diffusion barrier, which are critical for evaluating the suitability of M_2B_2 as an anode material for MIBs.

Structural stability: cohesive energy and phonon dispersion

After full relaxation of the M_2B_2 monolayer structures, their energetic stability was determined by calculating the cohesive energy per atom. Cohesive energy reflects the energy required to disassemble a compound into its isolated atomic constituents and is commonly used as a measure of thermodynamic stability. A higher cohesive energy indicates a more stable structure, as it implies stronger binding between atoms. In this study, cohesive energy was computed for the model containing 8 M and 8 B atoms, using the following expression:

$$E_{\text{coh}} = (8E_M + 8E_B - E_{M_2B_2})/16$$

where E_M and E_B are the total energies of isolated M and B atoms, respectively, and $E_{M_2B_2}$ is the total energy of fully relaxed M_2B_2 monolayer in the supercell.

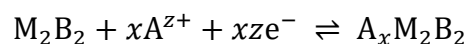
To assess dynamical stability, phonon dispersion curves were computed using the finite displacement method as implemented in the PHONOPY package (Baroni et al., 2001; Togo and Tanaka, 2015). Structures with no imaginary frequencies in their phonon spectra were considered dynamically stable.

Electronic conductivity: density of states

Electronic conductivity of the M_2B_2 monolayers was qualitatively assessed by calculating their density of states (DOS) using a dense $15 \times 15 \times 1$ k -point mesh. A finite DOS at the Fermi level indicates metallic behavior and suggests that the material can efficiently conduct electrons, which is generally desirable for fast charge transport.

Theoretical capacity and layer adsorption

The storage capacity of M_2B_2 monolayers was evaluated through modelling the layer-by-layer adsorption of carrier species ($A = \text{Li, Na, Mg, or Al}$) on both sides of the monolayers. This process models the reversible half-cell electrochemical reaction:



where z is the number of electrons transferred per carrier atom (1 for Li/Na, 2 for Mg, and 3 for Al). Here, x denotes the amount of carrier atoms on both sides. Specifically, x is 2, 4, and 6 correspond to the adsorption of 1, 2, and 3 layers, respectively.

To evaluate the energetic feasibility of adsorption, the average adsorption energy per carrier atom was calculated. This is defined as the energy difference between the adsorbed and non-adsorbed systems, normalized by the amount of carrier atoms. Mathematically, it is given by:

$$E_{\text{avg}} = \frac{E_{A_x M_2 B_2} - E_{M_2 B_2} - x E_A}{x}$$

where $E_{A_x M_2 B_2}$ is the total energy of $M_2 B_2$ with x adsorbed carrier species, $E_{M_2 B_2}$ is the total energy of the pristine monolayer, and E_A is the energy per atom of the carrier in its bulk metallic phase.

To identify how many layers of carriers can be stably accommodated, the consecutive adsorption energy was calculated. This quantity represents the energy required to adsorb an additional layer of carrier species and is defined as:

$$E_{\text{con}} = \frac{E_{A_{x_2} M_2 B_2} - E_{A_{x_1} M_2 B_2} - (x_2 - x_1) E_A}{(x_2 - x_1)}, \quad (x_2 > x_1)$$

where x_1 and x_2 represent the number of carriers before and after a new adsorption layer, respectively. A negative E_{con} indicates that the additional layer is energetically favorable. However, to account for thermal excitation, a threshold of -0.05 eV/atom was used, which is comparable to thermal energy of 0.03 eV at 300K. This criterion is used to determine the maximum number of adsorbed layers (n_{max}) for each composition, defined as the largest value of n such that all E_{con} values up to n satisfy the threshold condition. In this study, adsorption scenarios were examined up to three layers on each side of the monolayer.

The theoretical capacity of $M_2 B_2$ anode using carriers (A) was then estimated by the amount of charge containing in the anode normalized by total mass of the anode:

$$C = \frac{n_{\text{max}} \cdot z \cdot F}{m_{M_2 B_2} + n_{\text{max}} \cdot m_A}$$

where F is Faraday's constant of 26,801 mAh/mol. The $m_{M_2 B_2}$ and m_A are the molecular masses of $M_2 B_2$ and charge carriers, respectively.

Open-circuit voltage (OCV)

The OCV was estimated from Gibbs free energy differences between structures with successive carrier species contents (x). Following the DFT-based thermodynamic formulation, the average OCV over the range from x_1 to x_2 is given by:

$$\text{OCV} = -\frac{\Delta G}{(x_2 - x_1)ze}$$

where $\Delta G = \Delta E + P\Delta V - T\Delta S$ is the Gibbs free energy change, F is the Faraday constant. At room temperature, the entropic ($T\Delta S \approx 25 \text{ meV}$) and pressure-volume ($P\Delta V \approx 0.01 \text{ meV}$) contributions are negligible compared to internal energy changes, allowing for the commonly used approximation:

$$\text{OCV} \approx -\frac{\Delta E}{(x_2 - x_1)ze}$$

Thus, the calculated OCV represents an average voltage over the range from x_1 to x_2 , and can be expressed as:

$$\text{OCV} = -\frac{E_{A_{x_2}M_2B_2} - E_{A_{x_1}M_2B_2} - (x_2 - x_1)E_A}{(x_2 - x_1)ze} = -\frac{E_{\text{con}}}{ze}$$

Ionic conductivity: diffusion barrier

To assess the ionic conductivity of carrier species on M_2B_2 monolayer, the diffusion barrier of a single carrier atom was evaluated using CI-NEB method (Henkelman et al., 2000). Diffusion was modeled as surface migration between nearest-neighbor adsorption sites along inequivalent directions. Five intermediate images between endpoints were used to map the minimum energy pathway.

3.4.4 Material features

To uncover structure–property relationships of M_2B_2 anode materials, we constructed a comprehensive feature set encompassing elemental and structural descriptors. These features were used as input for ML model training. The features are grouped into three main categories:

Elemental features of the transition metal (M): These descriptors capture intrinsic chemical and physical properties of the M atoms forming the M_2B_2 lattice.

They include the metallic radius, electronegativity, cohesive energy, number of unpaired d-electrons, and total number of d-electrons. These parameters are closely related to bonding strength, electronegativity-driven charge transfer, and electronic structure, which can influence adsorption behavior and conductivity. The elemental features were fetched from *Mendeleev* python library (Mentel, 2014).

Elemental features of the carrier species (A): Features of carrier species were selected to capture the chemical behavior of the adsorbed carrier. These include the metallic radius, electronegativity, cohesive energy, first ionization energy, and number of valence electrons. These features may affect adsorption strength, diffusion barriers, and redox activity on the anode M_2B_2 surface.

Table 3.1 The elemental and structural parameters used as features for machine learning model training.

| Category | Feature name | Description |
|---------------------|-------------------|--|
| Elemental M | M_metallic_radius | Metallic radius of M |
| | M_EN | Electronegativity (Pauling scale) of M |
| | M_cohesive_energy | Cohesive energy of M |
| | M_ne_d | Number of valence d-electrons of M |
| | M_ne_unpair | Number of unpaired d-electrons of M |
| Elemental A | A_metallic_radius | Metallic radius of A |
| | A_EN | Electronegativity (Pauling scale) of A |
| | A_cohesive_energy | Cohesive energy of A |
| | A_IE | First ionization energy of A |
| | A_ne_valence | Number of valence electrons of A |
| Structural M_2B_2 | PC1 | First principal component from SOAP |
| | PC2 | Second principal component from SOAP |
| | PC3 | Third principal component from SOAP |

Structural features of M_2B_2 monolayers: To encode the atomic environment and geometry of M_2B_2 monolayers, the Smooth Overlap of Atomic Positions (SOAP) descriptor were employed (De et al., 2016). This descriptor captures radial and angular distributions of atoms around a local environment of different lattice phases:

orthorhombic, hexagonal, trigonal, and tetragonal. The SOAP features were computed using the dscribe Python package (Laakso et al., 2023), with a cutoff radius of 4.0 Å, maximum radial basis functions of 12, and maximum angular basis functions of 12. Principal component analysis (PCA) was subsequently applied to the SOAP vector to reduce dimensionality and extract the first three principal components (PC1, PC2, and PC3), which serve as compact and informative representations of the atomic structure for model input.

This feature set ensures that both chemical identity and atomic configuration are captured, providing a robust basis for training interpretable ML models aimed at predicting material properties.

3.4.5 Model construction and interpretation

To uncover the underlying relationships between materials features and anode performance of M_2B_2 MBenes, this thesis employed a ML framework focused on both predictive power and scientific interpretability. The design of the modeling strategy was guided by three concepts: (1) simplicity, by constructing models using minimal and informative feature subsets to redundancy between features and enhance clarity; (2) sufficient accuracy, by ensuring reliable predictions through rigorous evaluation; and (3) monotonic interpretation, by selecting models in which each feature exhibits a consistent, directional effect on the target property. In this thesis, five regression models were studied namely linear regression, decision tree, random forest, gradient boosting, and XGBoost.

The dataset used in this step consisted of DFT-computed target properties of M_2B_2 (in Section 3.4.3) and corresponding input features (in Section 3.4.4). Prior to modeling, outliers were removed to improve data robustness. The dataset was then randomly split into training and testing subsets in a 90:10 ratio, with stratified sampling applied to preserve the target distribution. All features were standardized using standard scaling, fitted on the training data and applied to the test data.

For ML models training, all valid combinations of selected features from the three feature categories (see Section 3.4.4) were systematically enumerated. To balance model simplicity and interpretability, one or two features were selected from each feature category. This enumeration strategy reduces model complexity and helps

mitigate redundancy and dilution of feature importance. For cohesive energy model, the features of A group were omitted from the combination.

For each enumerated feature subset, the regression models were trained and model hyperparameters were tuned using Optuna with 200 trials. The hyperparameter optimization was conducted with two simultaneous objectives: (1) minimizing the 10-fold cross-validation mean absolute error (CV-MAE) for predictive accuracy, and (2) maximizing the interpretability score, defined as the minimum absolute Spearman correlation between each feature and its corresponding SHAP value:

$$\text{interpretability} = \min_i |\rho_i|$$

where ρ_i is the Spearman correlation between the i^{th} feature and its SHAP value. This metric captures the monotonicity of the worst-behaving feature.

The models and metric results from all Optuna training trials across all feature subsets were aggregated. A Pareto frontier was constructed to visualize the trade-off between predictive accuracy (CV-MAE) and model interpretability score. The final model was selected as the one with the lowest CV-MAE among those satisfying the interpretability threshold. In this case, the interpretability score threshold was chosen to be 0.5, which is an empirical threshold that balance interpretation and accuracy.

This final model was then evaluated on the unseen test data using standard regression metrics: MAE, RMSE, and R^2 . Finally, to interpret the model, SHAP summary and dependence plots were generated. These visualizations revealed global and local feature effects, highlighting which features most strongly influence the target property and how they affect the predictions, thereby supporting scientific interpretation and rational design of MBenes for anode applications.

3.5 References

- Baroni, S., de Gironcoli, S., Dal Corso, A., and Giannozzi, P. (2001). Phonons and related crystal properties from density-functional perturbation theory. *Reviews of Modern Physics*, 73(2), 515–562.
- Blöchl, P. E. (1994). Projector augmented-wave method. *Physical Review B*, 50(24), 17953–17979.

- Bo, T., Liu, P.-F., Zhang, J., Wang, F., and Wang, B.-T. (2019). Tetragonal and trigonal Mo₂B₂ monolayers: two new low-dimensional materials for Li-ion and Na-ion batteries. *Physical Chemistry Chemical Physics*, 21(9), Article 9.
- Born, M., and Oppenheimer, R. (1927). Zur Quantentheorie der Molekeln. *Annalen Der Physik*, 389(20), 457–484.
- Breiman, L. (2001). Random Forests. *Machine Learning*, 45(1), 5–32.
- Chen, T., and Guestrin, C. (2016). XGBoost: A Scalable Tree Boosting System. *Proceedings of the 22nd ACM SIGKDD International Conference on Knowledge Discovery and Data Mining*, 785–794.
- De, S., Bartók, A. P., Csányi, G., and Ceriotti, M. (2016). Comparing molecules and solids across structural and alchemical space. *Physical Chemistry Chemical Physics*, 18(20), 13754–13769.
- Delaunay, J. (2023). *Explainability for machine learning models: from data adaptability to user perception* [Phdthesis, Université de Rennes].
- Feynman, R. P. (1939). Forces in Molecules. *Physical Review*, 56(4), 340–343.
- Friedman, J. H. (2001). Greedy function approximation: A gradient boosting machine. *The Annals of Statistics*, 29(5), 1189–1232.
- Grimme, S., Antony, J., Ehrlich, S., and Krieg, H. (2010). A consistent and accurate ab initio parametrization of density functional dispersion correction (DFT-D) for the 94 elements H-Pu. *The Journal of Chemical Physics*, 132(15), 154104.
- Grimme, S., Ehrlich, S., and Goerigk, L. (2011). Effect of the damping function in dispersion corrected density functional theory. *Journal of Computational Chemistry*, 32(7), 1456–1465.
- Hassija, V., Chamola, V., Mahapatra, A., Singal, A., Goel, D., Huang, K., Scardapane, S., Spinelli, I., Mahmud, M., and Hussain, A. (2024). Interpreting Black-Box Models: A Review on Explainable Artificial Intelligence. *Cognitive Computation*, 16(1), 45–74.
- Henkelman, G., Uberuaga, B. P., and Jónsson, H. (2000). Climbing image nudged elastic band method for finding saddle points and minimum energy paths. *Journal of Chemical Physics*, 113(22), 9901–9904. Scopus.

- Hohenberg, P., and Kohn, W. (1964). Inhomogeneous Electron Gas. *Physical Review*, 136(3B), B864–B871.
- Kohn, W., and Sham, L. J. (1965). Self-Consistent Equations Including Exchange and Correlation Effects. *Physical Review*, 140(4A), A1133–A1138.
- Kresse, G., and Furthmüller, J. (1996a). Efficiency of ab-initio total energy calculations for metals and semiconductors using a plane-wave basis set. *Computational Materials Science*, 6(1), 15–50.
- Kresse, G., and Furthmüller, J. (1996b). Efficient iterative schemes for ab initio total-energy calculations using a plane-wave basis set. *Physical Review B*, 54(16), 11169–11186.
- Kresse, G., and Hafner, J. (1993). Ab initio molecular dynamics for liquid metals. *Physical Review B*, 47(1), 558–561.
- Kresse, G., and Joubert, D. (1999). From ultrasoft pseudopotentials to the projector augmented-wave method. *Physical Review B*, 59(3), 1758–1775.
- Laakso, J., Himanen, L., Homm, H., Morooka, E. V., Jäger, M. O. J., Todorović, M., and Rinke, P. (2023). Updates to the DScribe library: New descriptors and derivatives. *The Journal of Chemical Physics*, 158(23), 234802.
- Larsen, A. H., Mortensen, J. J., Blomqvist, J., Castellì, I. E., Christensen, R., Dułak, M., Friis, J., Groves, M. N., Hammer, B., Hargus, C., Hermes, E. D., Jennings, P. C., Jensen, P. B., Kermode, J., Kitchin, J. R., Kolsbjerg, E. L., Kubal, J., Kaasbjerg, K., Lysgaard, S., ... Jacobsen, K. W. (2017). The atomic simulation environment—a Python library for working with atoms. *Journal of Physics: Condensed Matter*, 29(27), 273002.
- Linardatos, P., Papastefanopoulos, V., and Kotsiantis, S. (2021). Explainable AI: A Review of Machine Learning Interpretability Methods. *Entropy*, 23(1), Article 1.
- Lundberg, S. M., and Lee, S.-I. (2017). A Unified Approach to Interpreting Model Predictions. *Advances in Neural Information Processing Systems*, 30.
- Mentel, E. (2014). *Mendeleev - A Python resource for properties of chemical elements, ions and isotopes* (Version 0.17.0) [Computer software].

- Momma, K., and Izumi, F. (2011). VESTA 3 for three-dimensional visualization of crystal, volumetric and morphology data. *Journal of Applied Crystallography*, 44(6), 1272–1276.
- Monkhorst, H. J., and Pack, J. D. (1976). Special points for Brillouin-zone integrations. *Physical Review B*, 13(12), 5188–5192.
- Payne, M. C., Teter, M. P., Allan, D. C., Arias, T. A., and Joannopoulos, J. D. (1992). Iterative minimization techniques for ab initio total-energy calculations: molecular dynamics and conjugate gradients. *Reviews of Modern Physics*, 64(4), 1045–1097.
- Perdew, J. P., Burke, K., and Ernzerhof, M. (1996). Generalized Gradient Approximation Made Simple. *Physical Review Letters*, 77(18), 3865–3868.
- Ribeiro, M. T., Singh, S., and Guestrin, C. (2016). “Why Should I Trust You?”: Explaining the Predictions of Any Classifier. *Proceedings of the 22nd ACM SIGKDD International Conference on Knowledge Discovery and Data Mining*, 1135–1144.
- Sholl, D. S., and Steckel, J. A. (2009). *Density Functional Theory: A Practical Introduction* (1st ed.). Wiley.
- Togo, A. (2023). First-principles Phonon Calculations with Phonopy and Phono3py. *Journal of the Physical Society of Japan*, 92(1), 012001.
- Togo, A., and Tanaka, I. (2015). First principles phonon calculations in materials science. *Scripta Materialia*, 108, 1–5.
- Wang, V., Xu, N., Liu, J.-C., Tang, G., and Geng, W.-T. (2021). VASPKIT: A user-friendly interface facilitating high-throughput computing and analysis using VASP code. *Computer Physics Communications*, 267, 108033.

CHAPTER IV

RESULTS AND DISCUSSION

4.1 Overview

This chapter presents the results and discussion of the computational screening of M_2B_2 MBene as potential anode candidates for metal-ion batteries (MIBs). The screening covers 26 transition metals (M) across four crystal phases: orthorhombic (ort), hexagonal (hex), trigonal (tri), and tetragonal (tetr). Four charge carrier species are considered: Li, Na, Mg, and Al. The evaluation begins with intrinsic properties, including crystal structures, energetic and dynamical stability, and electronic behavior. Electrochemical performance is then assessed based on key metrics: theoretical capacity, open-circuit voltage (OCV), and diffusion barriers of carrier species. All properties are analyzed and compared to suggest promising candidates. Ultimately, this chapter fulfills the research objectives by systematically identifying and rationalizing promising MBenes, thereby contributing to the design of next-generation energy storage materials.

4.2 Geometry, stability, and electronic properties of M_2B_2

This section presents intrinsic properties of the screened M_2B_2 monolayers, including their crystal structure, cohesive energy, phonon dispersion, and electronic structures, as determined by DFT. These characteristics are crucial for evaluating structural stability and electronic conductivity as potential anode materials.

4.2.1 Crystal structure of M_2B_2

The crystal structures of M_2B_2 MBenes for various M were constructed from the prototype of Mo_2B_2 across four structural phases: ort, hex, tri, and tetr (details in Section 3.4.2). These phases significantly differ in their lattice symmetry, atomic arrangements, and coordination environments, as illustrated in **Figure 4.1** using Mo_2B_2 as a representative example.

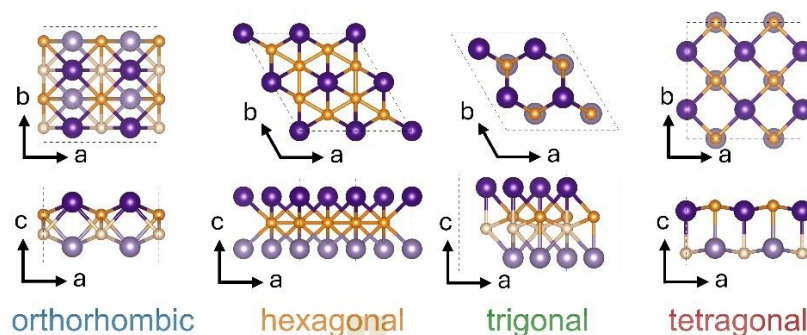


Figure 4.1: Optimized crystal structures of M_2B_2 MBenes in four distinct phases: orthorhombic, hexagonal, trigonal, and tetragonal. Top and side views are shown for each structure, using Mo_2B_2 as a representative example. Purple and orange spheres represent transition metal (M) and boron (B), respectively. Slight variations in colors shades are used for visual clarity.

Orthorhombic (ort): This phase possesses rectangular symmetry ($\gamma = 90^\circ$), with slightly different lattice constants a and b . B atoms form buckled chains extending along the b -direction and are connected by M atoms, forming internal layers with M atoms on the surface. Each M atom is connected to 6 B atoms, resulting in a coordination number of 6 (CN = 6). While each B atom is bonded to 2 B atoms within their buckled lines and to 6 M atoms (CN = 8).

Hexagonal (hex): This phase is defined by a hexagonal lattice ($\gamma = 120^\circ$), with equal lattice constants a and b . The B atoms are arranged in a flat hexagonal honeycomb-like structure. M atoms are positioned on top and bottom of the 6-fold hollow site of the B sheet, forming exposed layers. Each M atom forms bonds with 6 B atoms (CN = 6). Conversely, each B atom forms bonds with 6 M atoms and 3 neighboring B atoms within the B-sheet (CN = 9).

Trigonal (tri): This phase maintains the hexagonal lattice ($\gamma = 120^\circ$) but features differ due to the vertical buckling of the hexagonal B sheet. Instead of CN = 6, the M atoms are positioned on top of the lowered buckled B sites. Each M atom is bonded to another 4 B atoms (CN = 4). Correspondingly, each B atom is connected to 3 neighboring B atoms within the buckled sheet and to 4 exposed M atoms (CN = 7).

Tetragonal (tetr): This phase possesses rectangular symmetry ($\gamma = 90^\circ$), with equal lattice constants a and b . B and M atoms alternate in checker's board pattern.

Each M and B atom has CN of 5, exclusively forming bonds with atoms of the opposite type. Unlike the other phases, both B and M atoms are exposed to the surfaces, and there are no covalent B-B bonds present within this configuration.

To further analyze the diversity of M_2B_2 MBene structures across various compositions and crystal phases, the Smooth Overlap of Atomic Positions (SOAP) descriptor was employed to encode local atomic environments into high-dimensional numerical representations. By capturing both radial and angular distributions of neighboring atoms, SOAP effectively distinguishes subtle geometrical variations across a large structural dataset. To reduce the complexity of the high-dimensional SOAP descriptor space and enable efficient analysis, Principal Component Analysis (PCA) was applied. This process yields a set of orthogonal principal components ranked by explained variance. In this study, the first three components, PC1, PC2, and PC3, were selected. Although the exact physical meaning of each component is not straightforward, they serve as compact numerical encodings of structural information and are retained as input features in subsequent machine learning (ML) models.

To explore the structural information captured by the selected principal components, we examined their distributions and correlations with some geometric features. The following observation illustrates possible correlations between the components and structural characteristics. As shown in **Figure 4.2a**, the PC1-PC2 plot reveals clustering that corresponds to the four crystal phases. PC1 appears to separate rectangular ($\gamma = 90^\circ$) from hexagonal ($\gamma = 120^\circ$) lattices, while PC2 could be associated with the coordination number (CN) of the M. Higher CN phases (i.e., ort and hex) tend to occupy different regions than those with lower CN phases (i.e., tri and tetr). **Figure 4.2b** shows a negative correlation between PC3 and surface area, indicating that PC3 captures structural compactness. Similar trends are observed from lattice constants, M-B and M-M distances, and the metallic radius of M, as all of which are inherently related to surface area.

Thus, PC1, PC2, and PC3 serve as compact numerical descriptors of the local atomic environments derived from the high-dimensional SOAP representations. While these components show observable correlations with structural features such as lattice symmetry, coordination environment, and compactness, these interpretations

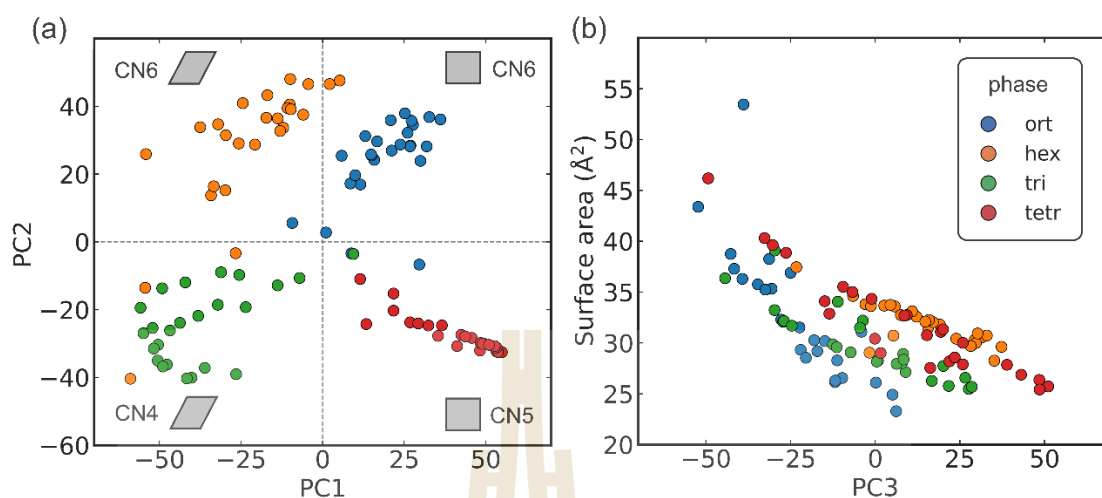


Figure 4.2 Principal component analysis (PCA) of SOAP-derived structural descriptors for M_2B_2 MBenes. (a) PC1 vs. PC2 projection showing phase-based clustering. PC1 primarily captures differences in lattice symmetry, separating rectangular (orthorhombic, tetragonal) and hexagonal (hexagonal, trigonal) systems, while PC2 reflects the coordination number (CN) of M atom, distinguishing low-CN (4–5) from high-CN (6) structures. (b) PC3 plotted against surface area, indicating variation in structural compactness.

are heuristic and do not imply definitive physical meaning or causality. The principal components primarily provide a reduced and tractable representation of structural variation, which will be used as input features in subsequent ML models to explore and predict structure–property relationships across the MBenes dataset.

4.2.2 Energetic stability: cohesive energy

Material stability is a key factor in determining the suitability of a compound as an anode material for MIBs. This section focuses on energetic stability, which serves as a fundamental criterion for the likelihood of successful material synthesis. A commonly used computational metric for this purpose is cohesive energy, which reflects the strength of atomic bonding within the compound. Materials with higher cohesive energy are generally more thermodynamically stable and are considered more promising for long-term cycling stability in battery applications.

The cohesive energies per atom of each M_2B_2 composition and phase was calculated using DFT, as described in Section 3.4.3. Two structures, i.e., tri- Ag_2B_2 and tri- Au_2B_2 , were excluded due to structural transformation observed during geometry optimization. As shown in **Figure 4.3**, the cohesive energies vary systematically across the 3d, 4d, and 5d transition metals series, exhibiting a characteristic M-shaped trend. Minor variations are observed among the four crystal phases. A detailed discussion of this trend is provided in a later section.

While cohesive energy alone does not guarantee synthesizability, it provides a meaningful thermodynamic reference. Among the experimentally reported M_2B_2 compounds, namely ort- Mo_2B_2 , ort- Cr_2B_2 , and hex- Ti_2B_2 , the cohesive energy of ort- Cr_2B_2 is the lowest and is thus used as a practical benchmark (indicated by the dashed line in **Figure 4.3a**). Compositions with higher cohesive energies may be considered more energetically favorable and may have higher potential to be synthesized under suitable conditions. However, this assumption should be interpreted with caution, as actual synthesizability also depends on kinetic barriers, reaction pathways, and synthesis environments. Additionally, the relatively small energy differences between phases suggest that metastable structures may be experimentally accessible with appropriate synthetic strategies and conditions.

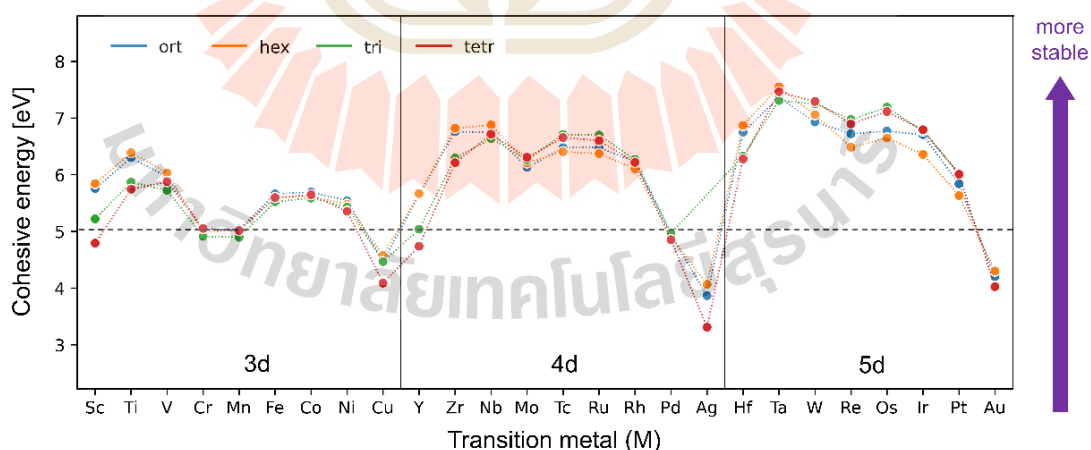


Figure 4.3 Cohesive energy per atom of M_2B_2 MBenes across 3d, 4d, and 5d transition metals (M) for different crystal phases. The dashed horizontal line marks the cohesive energy of ort- Cr_2B_2 , a compound successfully synthesized in prior work, which is used here as a practical benchmark to guide the assessment of synthesizability.

To assess the accuracy of our calculations, the cohesive energies were compared with previously reported values. For hex- M_2B_2 with $M = \text{Sc, Ti, V, Cr, Y, Zr, Nb, and Mo}$, our results are within ~ 0.1 eV/atom of those by He et al. (He et al., 2021), demonstrating strong consistency. Similarly, the values for tetr- Mo_2B_2 and tri- Mo_2B_2 (6.31 and 6.26 eV/atom) are in good agreement with those by Bo et al. (Bo et al., 2019) (6.49 and 6.40 eV/atom). Slightly larger discrepancies for ort- Mn_2B_2 and ort- Zr_2B_2 , compared to Jia et al. (Jia et al., 2019) and Z. Jiang et al. (Jiang et al., 2018), may arise from differences in computational settings. These comparisons support the reliability of our DFT calculations.

To gain deeper understanding of the factors influencing the cohesive energy of M_2B_2 , ML models were employed to identify key contributing features. Five regression models were trained using a combination of elemental features of M and structural features derived from SOAP principal components. The details of features and model training are written in Sections 3.4 and 3.5. As shown in **Figure 4.4a**, all five models demonstrated reasonable predictive performance, with Gradient Boosting emerging as the best-performing approach (MAE = 0.110 eV, $R^2 = 0.974$). The parity plot in **Figure 4.4b** shows that the predicted cohesive energies align closely with DFT-calculated values across the dataset. Linear Regression also performed well, slightly outperforming Random Forest and XGBoost, while the Decision Tree model lagged significantly. Due to its superior accuracy and ability to model complex structure-property relationships, Gradient Boosting was chosen for detailed interpretation.

To investigate the Gradient Boosting model and identify the key factors influencing the cohesive energy of M_2B_2 , SHAP analysis was conducted (see **Figure 4.4c**). The cohesive energy of constituent element M emerged as the most influential feature, with a SHAP importance score of 0.724, far exceeding that of the other selected features. These include PC2 (0.080), electronegativity (EN) of M (0.073), and PC3 (0.069). Although PC2 and PC3 contribute less than the cohesive energy of M , they still capture meaningful structural variations. These features help explain subtle differences in the cohesive energies of M_2B_2 compounds and reflect trends associated with crystal phase preferences.

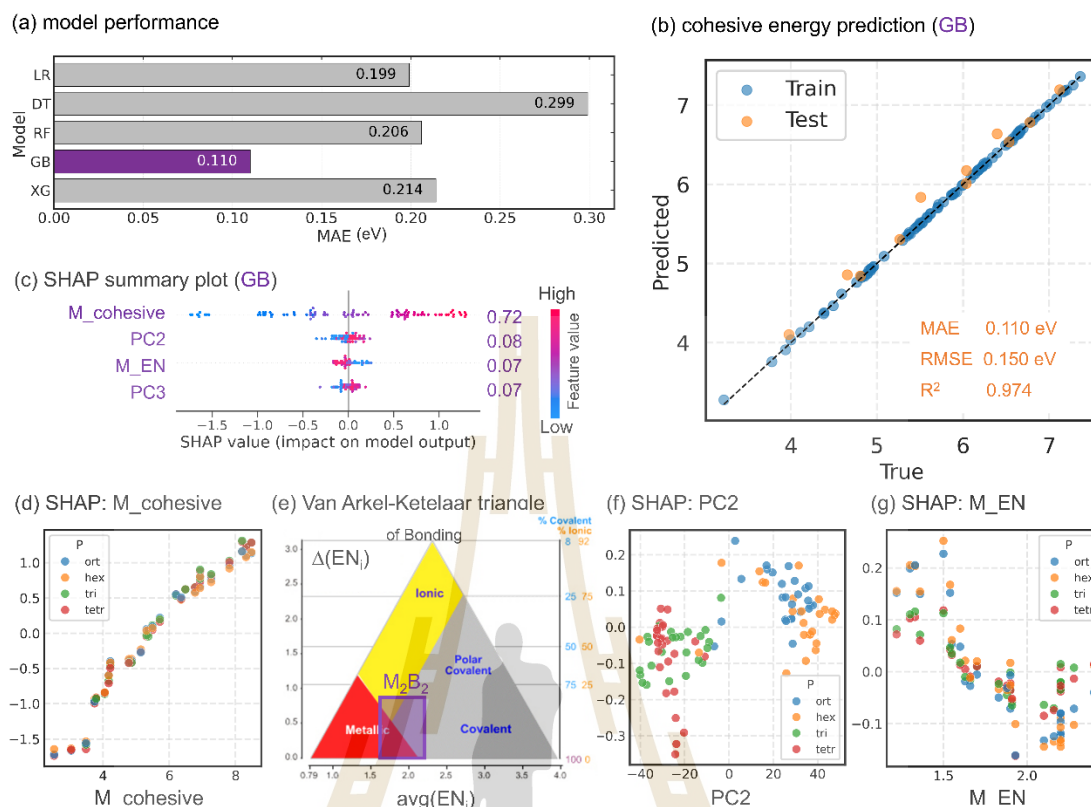


Figure 4.4 Machine learning prediction and SHAP-based interpretation of cohesive energy for M_2B_2 MBenes. (a) Model comparison showing Gradient Boosting (GB) as the best-performing regressor. (b) Parity plot of predicted vs. DFT-calculated cohesive energies using the GB model. (c) SHAP summary plot identifying the four selected features: cohesive energy of M (M_{cohesive}), PC2, PC3, and EN of M (M_{EN}). (d–g) SHAP dependence plots. (e) also includes the Van Arkel–Ketelaar triangle of bonding illustrating bonding types based on electronegativity (Jensen, 1995).

The strong contribution of cohesive energy of M is further supported by a clear and consistent positive correlation between the cohesive energy of M and their SHAP value (contribution on the predicted cohesive energy of M_2B_2), as shown in the dependence plot (Figure 4.4d). As we can see from Figure 4.3, cohesive energies of M_2B_2 MBene exhibit a characteristic M-shaped trend across the 3d, 4d, and 5d transition metal series, which is similar to cohesive energies of elemental M in their bulk state. It shows an initial increase among early transition metals, a dip near the middle of the series, a slight rise and a sharp decline among late transition metals. These findings indicate that the bonding characteristics in M_2B_2 compounds closely resemble those

in their corresponding pure transition metals. Moreover, these bond strengths and structural stability also vary systematically across the transition metal series, reflecting the influence of elemental character on cohesive energy.

Among various bonds in M_2B_2 structures, the dominant M-B bonds could play the main contribution in overall cohesive energy. We find that the characteristic of these M-B bonds is similar to that of the metallic type of bonding, as supported by the Van Arkel-Ketelaar triangle diagram (**Figure 4.4e**), where chemical bond type can be classified based on average and difference of electronegativity. Specifically, the electronegativity of B is 2.0, which is relatively high compared to most transition metals (ranging from 1.2 to 2.4), thereby resulting in moderate average and small difference and fall into metallic region or near the metallic-covalent boundary on the diagram as shown in **Figure 4.4e**. This can be implied that the bonding character in M_2B_2 shares similar features with metallic bonding in pure transition metals, supporting their M-shape characteristic trend of cohesive energies and their high correlation.

The cohesive energy of pure transition metals reflects the strength of metallic bonding. Across the 3d, 4d, and 5d series, cohesive energy generally follows a parabolic trend with respect to d-electron filling: it rises with the progressive occupation of bonding d-states, peaks near half-filled configurations, and declines as antibonding states become populated. This characteristic behavior is well explained by Friedel's rectangular d-band model, which links the evolution of bonding strength to the filling of bonding and antibonding orbitals (Friedel, 1954). Down a group, cohesive energies tend to increase from 3d to 5d elements due to greater orbital overlap, broader d-bands, and enhanced electron delocalization in heavier atoms (Boring and Smith, 2000). Notably, the 3d series deviates from the ideal parabolic shape due to strong magnetic exchange and electron correlation effects. Near half-filling, Hund's rule promotes spin alignment and local moment formation, which competes with metallic bonding and reduces cohesive energy. This effect is particularly pronounced in elements like Mn, resulting in an M-shaped curve rather than a smooth parabola. In contrast, the 4d and 5d metals exhibit more regular trends, as their broader d-bands suppress localization and mitigate magnetic anomalies (Didukh, 2018; Tomacruz et al., 2025).

In addition to elemental features, structural descriptors derived from SOAP, particularly PC2 and PC3, provide information on phase-dependent variations in cohesive energy across M_2B_2 compounds. While their influence is much smaller than the cohesive energy of the transition metal, they still capture the structural effect. PC2 reflects differences in local atomic coordination and shows a trend with cohesive energy. As shown in the SHAP dependence plot (see **Figure 4.4f**), structures with positive PC2 values, i.e., ort- and hex-phases, generally exhibit higher cohesive energies. These phases typically feature sixfold coordination of the M by B atoms, increasing the number of M–B bonds and thereby contributing to greater stability. In contrast, tri- and tetra-phases, associated with negative PC2 values and lower coordination numbers, tend to have lower cohesive energies. PC3, associated with lattice compactness, shows relatively minor importance and has no clear explanation with cohesive energy.

Although a detailed physical explanation of how crystal phase influences the cohesive energy of M_2B_2 remains unclear, distinct preference can be observed across the transition metal series. Early transition metals such as Sc, Ti, Y, Zr, and Hf tend to favor ort- and hex-phases based on higher cohesive energies. In contrast, for many mid-to-late transition metals, especially those in the 4d and 5d series, the tri- and tetra-phases become energetically more favorable, with the exceptions of Cu, Ag, and Au.

This variation in phase stability across M_2B_2 composition can be further examined by considering both structural coordination and the EN of M. SHAP analysis reveals a parabola-like trend in contribution of EN to cohesive energy, with minimum SHAP values occurring near the EN of B (see **Figure 4.4g**). For early transition metals with low EN, the large EN difference (ΔEN) relative to B promotes polar metallic interactions, where ort- and hex-phases with high CN of B and M, are preferred, as they maximize electrostatic bonding contributions. These phases also feature short, strong B–B bonds, especially in the hex-phase, further enhancing cohesion. However, in the tri-phase, the B–B bond is more diffuse and less contribute to overall cohesion. As the EN of M increases across the series, ΔEN decreases and both high EN, the M–B bonds become less polar and more covalent-like, though still within the metallic bonding regime. In this range, tri- and tetra-phases become more stable. Their geometries allow

more localized and directional M–B interactions, better accommodating the covalent component of bonding that emerges with higher EN metals.

In summary, the energetic stability of M_2B_2 MBenes, as evaluated by cohesive energy calculations, exhibits a characteristic M-shaped trend across the transition metal series. ML and SHAP analysis suggest that this trend is primarily driven by the cohesive energy of M, underscoring the dominant influence of elemental properties. Subtle phase-dependent variations are also observed and can be partially explained by differences in local coordination environments and EN, although the underlying physical mechanisms remain not fully resolved. These results highlight the potential of the less-studied trigonal and tetragonal phases, which have received much less attention compared to the more commonly investigated ort- and hex-phases, as promising structures for further exploration.

4.2.3 Dynamical stability: phonon dispersion

In addition to energetic stability, dynamical stability is important for assessing the structural stability of the materials. It reflects the ability of material to resist lattice vibrations without undergoing spontaneous structural distortions or phase transitions. This is typically evaluated via phonon dispersion calculations, revealing the vibrational modes of a crystal structure. The presence of imaginary frequencies (i.e., negative values) indicates dynamical instability, while their absence suggests dynamical stability.

Phonon band structures were calculated along high-symmetric paths in the Brillouin zone for various M_2B_2 compositions and crystal phases. As shown in **Figure 4.5a**, the phonon spectrum of ort- Mo_2B_2 as an example contains no imaginary modes, suggesting its dynamical stability. A broader overview of stability for all four M_2B_2 crystal phases is provided in **Figure 4.5b**, organized by transition metal in periodic table format across the 3d, 4d, and 5d series.

The observed dynamical stability trends generally correlate those of cohesive energy presented in Section 4.2.2. Late transition metals based M_2B_2 compounds, which have lower cohesive energies, are often dynamically unstable in all phases. For a given transition metal, the phase with the highest cohesive energy typically corresponds to a dynamically stable structure. For instance, Sc_2B_2 and Ti_2B_2 are dynamically stable in ort- and hex-phases but unstable in tri- and tetr-phases as both

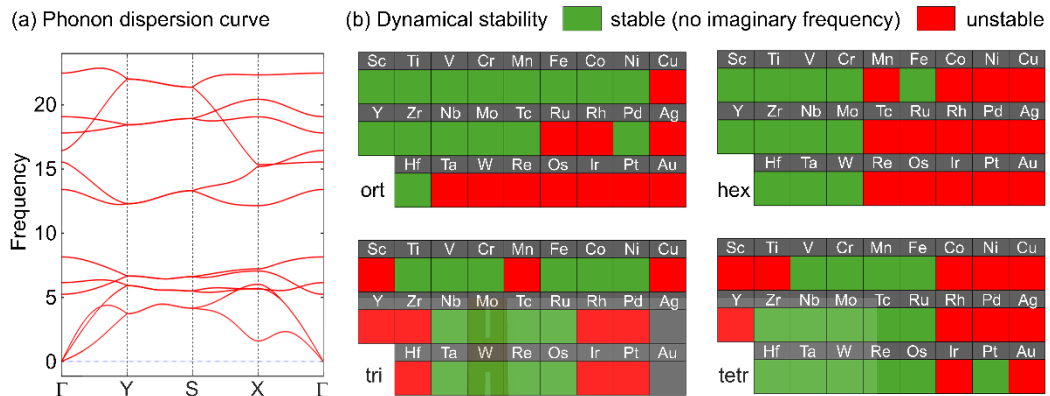


Figure 4.5 Dynamical stability of M_2B_2 MBenes evaluated using phonon dispersion calculations. (a) An example of phonon dispersion curve of ort- M_2B_2 , showing no imaginary frequencies and suggesting dynamical stability. (b) Dynamical stability summary for all investigated M_2B_2 compositions and phases, presented in periodic table format. Green squares indicate dynamically stable structures; red squares denote unstable structures.

featuring much lower cohesive energy. In contrast, Mo_2B_2 remains dynamically stable across all four phases, correlated with its uniformly high cohesive energies. Phases with higher cohesive energy are more likely to exhibit stable phonon modes, while low-cohesive-energy structures are prone to instability and phase transformation. These findings indicate a strong correlation between energetic and dynamical stabilities.

Our predictions also align well with prior theoretical studies. Dynamical stability of ort- M_2B_2 has been previously reported for several M including Mo, Sc, Ti, V, Cr, Mn, Fe, Co, Zr, Nb, Mo, and Hf (Guo et al., 2017; Jia et al., 2019; Jiang et al., 2018; Li et al., 2022; Z. Ma et al., 2020). For tri- and tetr- M_2B_2 , our results for Mo_2B_2 are consistent with those reported by (Bo et al., 2019; Jin and Schwingenschlögl, 2022). Similarly, the dynamical stability of hex- M_2B_2 for Zr, Y, and V has been reported in other studies (Gao et al., 2021; Wei et al., 2022; Yuan et al., 2019). A comprehensive screening of hex- M_2B_2 for 3d and 4d (He et al., 2021) also showed good agreement with our findings, with the exception of Fe and Pd. Overall, our results are aligned with existing literature.

In summary, phonon dispersion analysis provides a direct measure of dynamical stability. The dynamical stability generally correlated with cohesive energy such that M_2B_2 phase with higher cohesive energy are generally more resistant to lattice

distortion and phase transformation. For practical synthesis and application, candidate materials should exhibit both energetic and dynamical stability.

4.2.4 Electronic structure

High electronic conductivity is a desirable property for ideal anode materials, as it facilitates efficient charge transport during battery operation, thereby enhancing power density and rate performance. To evaluate this aspect for M_2B_2 MBenes, their electronic structures were analyzed using density of states (DOS) calculations at the PBE level of theory.

The projected DOS for *ort*- Mo_2B_2 exhibits significant hybridization between Mo and B atomic states, particularly in the energy window from -10 to -2 eV (see **Figure 4.6**). Near the Fermi level, the electronic states are predominantly contributed by Mo 4d orbitals, suggesting that these orbitals are primarily responsible for electronic conduction. The absence of a band gap indicates metallic behavior, implying that Mo_2B_2 can facilitate electron transport more effectively than semiconductors. While metallicity qualitatively suggests good electronic conductivity, a quantitative evaluation would be necessary to determine the actual conductive performance. However, such analyses are beyond the scope of this high-throughput screening.

The metallic character identified in *ort*- Mo_2B_2 is consistently observed across all M_2B_2 compositions and crystal phases examined. The projected DOS shows minimal variation between phases, indicating that crystal structure has little influence on the overall electronic character. Across the transition metal series, the primary difference is the more filling of d orbitals, which raises the Fermi level. These findings suggest that M_2B_2 possess favorable electronic conductivity, implying their potential as conductive anode materials.

Our findings at the PBE level are consistent with previous electronic structure studies of M_2B_2 (Bo et al., 2018; Guo et al., 2017; Y. Wang et al., 2024; Wei et al., 2022; Yuan et al., 2019). Moreover, selected cases further verified using hybrid functionals (HSE06) and spin-orbit coupling (SOC) also support the metallic nature of these materials, in alignment with the results derived from PBE level calculations (Guo et al., 2017; Y. Wang et al., 2024).

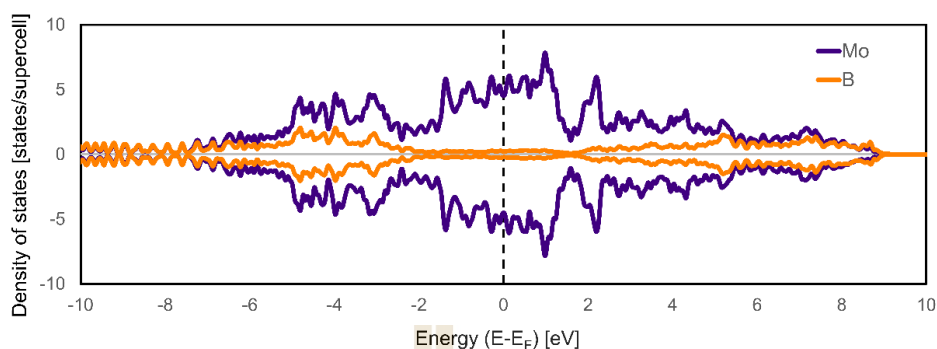


Figure 4.6 Projected density of states (PDOS) of ort-Mo₂B₂, representative of M₂B₂ MBenes. The finite density at the Fermi level suggests metallic character and implies good electronic conductivity.

4.3 Electrochemical properties

This section evaluates the electrochemical performance of M₂B₂ monolayers as potential anode materials of MIBs. Key descriptors, including adsorption of carrier species, theoretical capacity, OCV, and diffusion barrier of carrier atom, are evaluated to determine their effectiveness in supporting efficient charge storage and transport.

4.3.1 Adsorption of carrier species and theoretical capacity

An ideal anode material should exhibit a high theoretical capacity. Herein, the capacity of various M₂B₂ monolayers was estimated by evaluating the layer-by-layer adsorption of carrier species (Li, Na, Mg, and Al). The methodology for calculating adsorption energies, determining the maximum number of adsorbed layers (n_{max}), and computing theoretical capacity is detailed in Section 3.4.4.

To illustrate the approach, an example of Na adsorption on ort-Cr₂B₂ is shown in **Figure 4.7**. The adsorption process begins with a bare ort-Cr₂B₂ monolayer (denoted as 0L). In the first step, eight Na atoms are adsorbed symmetrically on both top and bottom surfaces, yielding the first layer adsorption (1L) with adsorption energy of -0.50 eV per Na atom. The subsequent second and third layers (2L and 3L) show consecutive adsorption energies of +0.02 and +0.03 eV, respectively. As the 2L exceeds the defined stability threshold (-0.05 eV), only the 1L is energetically favorable, and further adsorption is unfavorable. Therefore, the n_{max} for this Na adsorption is one. In contrast, when Li is used as the carrier on the ort-Cr₂B₂, the consecutive adsorption energies for

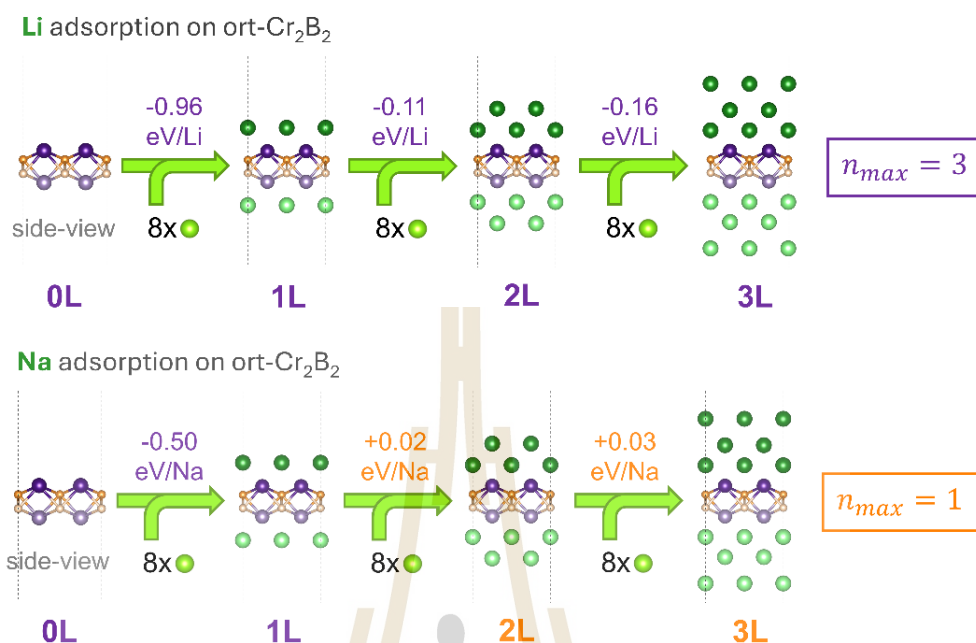


Figure 4.7 Layer-by-layer adsorption of Li and Na on representative ort-Cr₂B₂ MBene. The adsorption begins with the bare monolayer (0L), followed by the stepwise addition of carrier atoms on both sides of the surface to form the first (1L), second (2L), and third (3L) adsorption layers. The consecutive adsorption energy per atom is indicated at each step. The maximum number of adsorbed layers (n_{max}) determined by the adsorption energy threshold of -0.05 eV/atom.

the 1L, 2L, and 3L are -0.96 , -0.11 , and -0.16 eV, respectively. All of them are below the stability threshold, suggesting that up to three Li layers can be stably adsorbed or the n_{max} for this Li adsorption is three. In this study, adsorption was considered up to three layers, following a practical criterion commonly adopted in the literature (N. Ma et al., 2022). Although there is no strict physical limit, adding more layers may be unrealistic, as it would require an increasingly open space.

Beyond the representative case of ort-Cr₂B₂, the consecutive adsorption energies for the 1L, 2L, and 3L of various carrier species on representative phase ort-M₂B₂ are summarized in **Figure 4.8**. Overall, the 1L adsorption is substantially stronger than that of 2L and 3L—a trend consistently observed not only in the ort-phase but across all phases. This is primarily due to the direct interaction between carriers and exposed M or B atoms on M₂B₂ surface, resulting in larger adsorption energy and greater

variation across the transition metal series. In contrast, the 2L and 3L interact predominantly with previously adsorbed carriers rather than the M_2B_2 surface, leading to electrostatic screening and considerably weaker binding. In addition, 2L and 3L adsorption energies tend to be the same and show small variation across different M. This much weaker bind is consistent with previous report of Mg adsorption on M_2B (N. Ma et al., 2022).

The determination of n_{max} is governed by whether the consecutive adsorption energies of the 2L and 3L fall below the stability threshold. Thus, analyzing the adsorption behavior of these layers is essential. **Figure 4.8** summarizes the n_{max} across various M_2B_2 compositions and crystal phases for all considered carrier species. Among them, Al uniquely exhibits a clear distinction between the 2L and 3L adsorption energies unlike other carriers. This enhancement in 2L adsorption for Al likely stems from its higher ionic charge ($z = 3$), which promotes stronger interactions even with pre-adsorbed layers. Therefore, most compositions can adsorb Al at $n_{max} = 3$. The Mg also shows moderately strong adsorption. This enable adsorption up to $n_{max} = 3$ in most composition except some M_2B_2 involving M in 3d that limits lower n_{max} to 1 or 2. The Li displays slightly weaker the 2L and 3L adsorption, consistent with its lower ionic charge ($z = 1$), resulting in weakened surface interaction and n_{max} is limited to 1 or 2 in nearly half of the compositions. The Na, in contrast, shows the weakest adsorption among all carrier species. Its larger atomic radius in limited distancing from nearest neighbor leads to strong repulsion to its neighboring Na atoms, particularly in structure with tight lattice spacing. This effect is most pronounced in tri-phase, where Na-Na distance (e.g., 2.86 Å in tri- Mo_2B_2) is significantly shorter than in other phases (~3.04 - 3.07 Å for Mo_2B_2), amplifying repulsive interactions. As a result, Na adsorption is frequently limited to just a single layer.

The theoretical capacities of M_2B_2 monolayers were calculated based on the previously determined n_{max} values, following the methodology outlined in Section 3.4.4 and shown in this formula:

$$C = \frac{n_{max} \cdot z \cdot F}{m_{M_2B_2} + n_{max} \cdot m_A}$$

where F is Faraday's constant of 26,801 mAh/mol. The $m_{M_2B_2}$ and m_A are the molecular masses of M_2B_2 and charge carriers, respectively. The results for various carrier species across different compositions and crystal phases are presented in **Figure 4.9**. Since capacity is directly proportional to the number of electrons transferred per carrier (z), Al ($z = 3$) tends to exhibit the highest capacities, followed by Mg ($z = 2$), and then Li and Na ($z = 1$). For a given carrier species, capacity increases with n_{max} with composition achieving $n_{max} = 3$ showing particularly high values. Additionally, for compositions with equal n_{max} , gravimetric capacity is normalized by weight of the anode materials involving M, lighter M yields higher gravimetric capacity due to their lower mass contribution to the anode material.

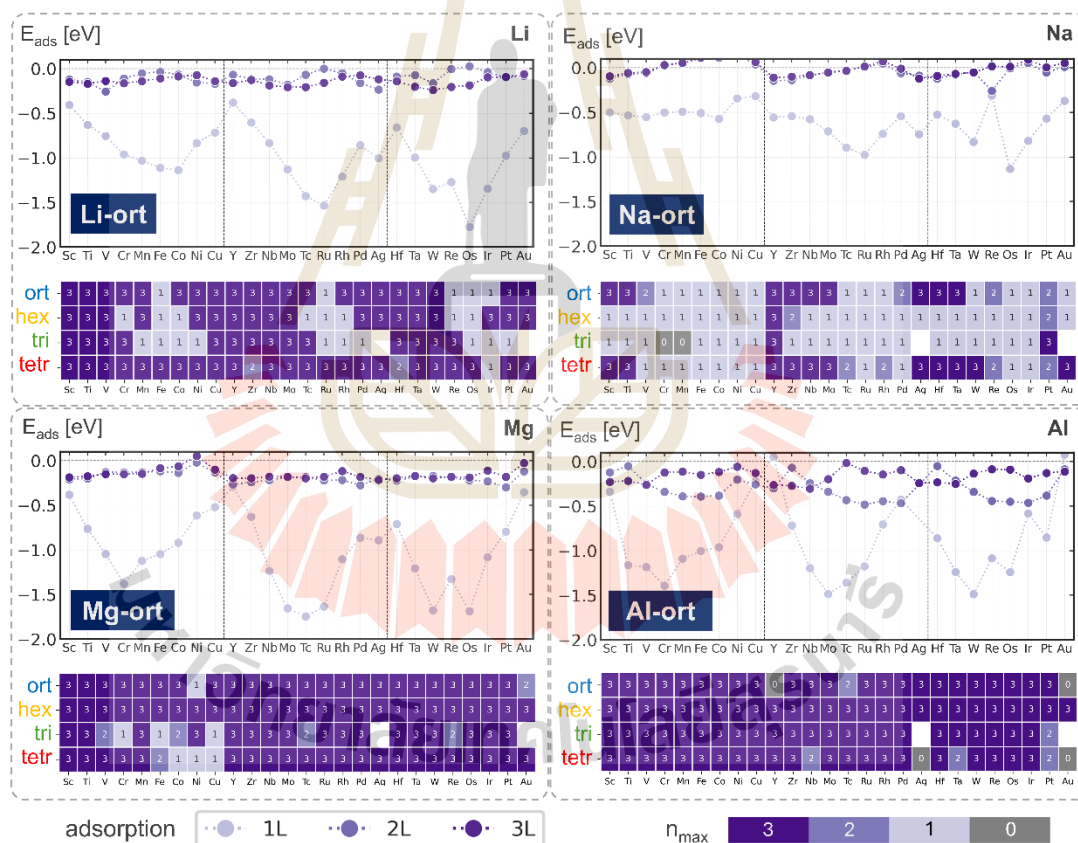


Figure 4.8 Consecutive adsorption energies (E_{ads}) of Li, Na, Mg, and Al on representative ort- M_2B_2 monolayers up to three layers (1L-3L). Heatmaps below show the maximum number of adsorbed layers (n_{max}) across all crystal phases (ort, hex, tri, tetr).



Figure 4.9 Gravimetric capacity and maximum number of adsorption layers (n_{max}) for Li, Na, Mg, and Al adsorption on M_2B_2 across different transition metals (M) and phases.

Validating our predicted theoretical capacities against literature values remains challenging due to methodological inconsistencies across different studies. Since capacity as well as n_{max} determination highly depends on how the stability of the 2L and 3L is evaluated. Herein, n_{max} is determined by applying a threshold of -0.05 eV/carrier for consecutive adsorption energy. However, other studies have adopted different approaches. Some assign n_{max} based on structural stability by observing atomic distortions in fixed-layer configurations (He et al., 2021; Y. Wang et al., 2024, p. 2), while others use thermodynamic criteria, where a positive adsorption energy signals instability (Bo et al., 2018; Jia et al., 2019). Furthermore, discrepancy in computational setups, such as vdW correction, may further influence the adsorption energy and n_{max} estimation. As a result, direct comparison with previously reported capacities may not be appropriate. For instance, our results predicted $n_{max}= 1$ for Li adsorption on *ort*-Fe₂B₂ due to the adsorption energy of the 2L is lines above our threshold. In contrast, some studies report two stable layers without significant structural distortions (Guo et al., 2017; Y. Wang et al., 2024), while another assumes only one (Liu et al., 2023). These variations in determination of n_{max} lead to differences in gravimetric capacities.

The theoretical capacities calculated in this work serve primarily as estimated descriptors for high-throughput screening. These values are based on simplified assumptions, including idealized layer-by-layer adsorption on monolayer M₂B₂ surfaces, and do not account for realistic factors such as thermal effect, kinetic effect, or morphological variations. As such, while the computed capacities provide a useful benchmark for comparative evaluation across compositions and phases, practical capacities achieved under real operating conditions may differ significantly.

4.3.2 Open-circuit voltage (OCV)

Another key property of anode materials is their OCV, which must lie within an appropriate range to ensure both electrochemical performance and safety. Low OCV can help maximize the full-cell voltage and energy density; however, if the OCV is too low, it may trigger unwanted side reaction with electrolyte, or promote metal dendrite growth, leading to safety risks. For LIB, the ideal OCV for anode material typically ranges from 0 to 1 versus Li/Li⁺. In this section, the OCV of various M₂B₂ monolayers are investigated by modeling the layer adsorption of different carrier species. The

computational methodology used for OCV determination is described in detail in Section 3.4.4.

To illustrate the OCV evaluation method, we present a representative case of Mg adsorption on *ort*-Mo₂B₂, as shown in **Figure 4.10**. The consecutive adsorption energies for the 1L, 2L, and 3L are -1.66, -0.18, -0.18 eV per Mg atom, respectively. Using equation ($OCV = -E_{con}/ze$), the corresponding average OCV values for each adsorption step (0L to 1L, 1L to 2L, and 2L to 3L) are calculated to be 0.83, 0.09, and 0.09 V, respectively. As expected, the 1L exhibits the highest OCV, reflecting the strongest interaction between Mg and the exposed Mo₂B₂ surface. In contrast, the 2L and 3L show significantly lower OCVs, as their adsorption is primarily influenced by interactions with previously adsorbed Mg atoms rather than direct bonding to the substrate. This sharp drop in OCV beyond the 1L is consistent across various compositions, crystal phases, and carrier species.

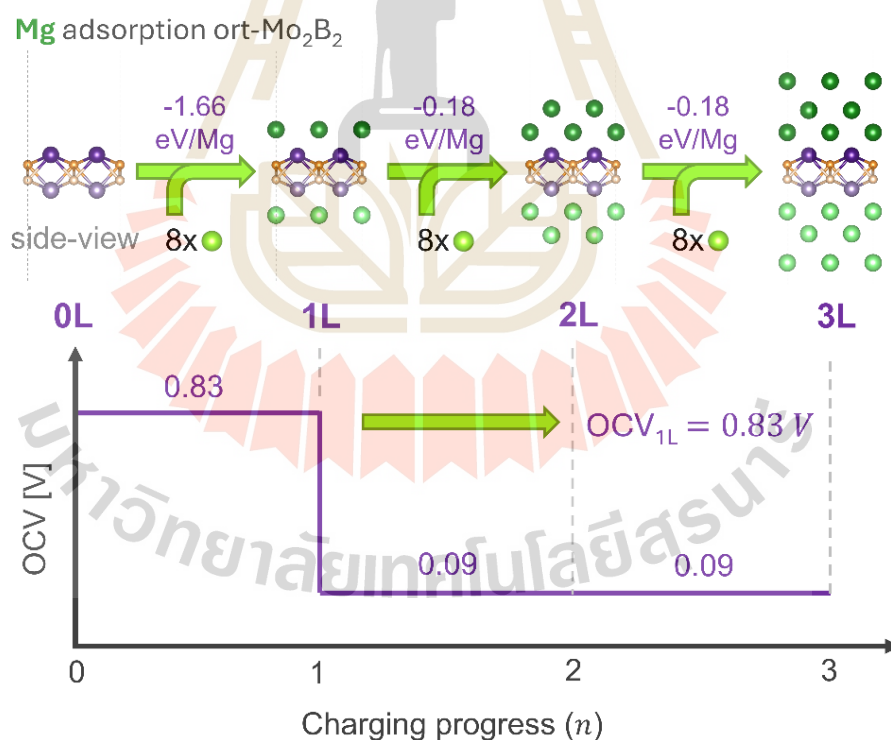


Figure 4.10 Open-circuit voltage (OCV) profile of Mg adsorption on representative *ort*-Mo₂B₂. The diagram illustrates consecutive adsorption energies from the bare surface (0L) to three adsorbed layers (3L), along with the corresponding average OCV values at each stage.

Given its sensitivity to the intrinsic interaction between the carrier species and the M_2B_2 surface, the OCV at 1L represents the upper bound of the voltage profile. It captures the strongest binding and the highest potential during the initial stage of charge/discharge. Therefore, the OCV at 1L serves as a key descriptor in this high-throughput screening.

The calculated OCV values at 1L adsorption, denoted as OCV, for all M_2B_2 compositions and crystal phases with various carrier species (Li, Na, Mg, and Al) are visualized in **Figure 4.11** and **Figure 4.12**. The distribution plot reveals distinct voltage profiles for each carrier type. Li shows the broadest distribution, extending up to 1.7 V with a peak centered around 0.7 V, reflecting a wide range of interaction strengths with the substrate. In contrast, Al exhibits a narrow distribution concentrated between 0.2–0.4 V, suggesting consistently low-voltage behavior. Na and Mg display intermediate voltage ranges, mostly centered around 0.3 – 0.6 V. These observed differences highlight the carrier species dependence of OCV and provide motivation for further investigation.

To gain deeper insight into the factors influencing the OCV, ML models were employed to identify and interpret key predictive features. Five regression algorithms were trained using a combination of elemental features of the carrier species (A), elemental features of the transition metal (M), and structural descriptors derived from SOAP principal components. Details of the input features and training procedures are provided in Sections 3.4 and 3.5. Among the models tested, Gradient Boosting delivered the best performance, achieving a mean absolute error (MAE) of 0.078 V and a coefficient of determination (R^2) of 0.849 (see **Figure 4.13a**). In contrast, simpler models such as Linear Regression and Decision Tree performed poorly, with MAEs of 0.114 V and 0.121 V, respectively. Random Forest (MAE = 0.094 V) also showed limited accuracy. XGBoost demonstrated comparable performance to Gradient Boosting, with an MAE of 0.080 V. The parity plot in **Figure 4.13b** confirms the strong agreement between predicted and DFT-calculated OCV values. Given its high predictive accuracy and robustness in capturing nonlinear structure–property relationships, Gradient Boosting was selected for further interpretability analysis.

OCV_{1L} [V]

| | Li | | | | | | | | | Na | | | | | | | | | Mg | | | | | | | | | Al | | | | | | | | |
|-----|------|------|------|------|------|------|------|------|------|------|------|------|------|------|------|------|------|------|------|------|------|------|------|------|------|------|------|------|------|------|------|------|------|------|------|------|
| | Sc | Ti | V | Cr | Mn | Fe | Co | Ni | Cu | Sc | Ti | V | Cr | Mn | Fe | Co | Ni | Cu | Sc | Ti | V | Cr | Mn | Fe | Co | Ni | Cu | Sc | Ti | V | Cr | Mn | Fe | Co | Ni | Cu |
| ort | 0.41 | 0.63 | 0.76 | 0.96 | 1.03 | 1.11 | 1.14 | 0.83 | 0.72 | 0.49 | 0.73 | 0.81 | 0.89 | 0.71 | 0.89 | 1.16 | 0.65 | 0.51 | 0.37 | 0.64 | 0.72 | 0.88 | 1.15 | 1.38 | 1.34 | 0.78 | 0.54 | 0.67 | 0.74 | 0.94 | 1.29 | 1.34 | 1.35 | 0.85 | 0.76 | |
| | Y | Zr | Nb | Mo | Tc | Ru | Rh | Pd | Ag | Y | Zr | Nb | Mo | Tc | Ru | Rh | Pd | Ag | Y | Zr | Nb | Mo | Tc | Ru | Rh | Pd | Ag | Y | Zr | Nb | Mo | Tc | Ru | Rh | Pd | Ag |
| | 0.38 | 0.60 | 0.83 | 1.13 | 1.43 | 1.54 | 1.21 | 0.86 | 1.01 | 0.37 | 0.64 | 0.72 | 0.88 | 1.15 | 1.38 | 1.34 | 0.78 | 0.54 | 0.64 | 0.72 | 0.88 | 1.15 | 1.38 | 1.34 | 0.78 | 0.54 | 0.67 | 0.74 | 0.94 | 1.29 | 1.34 | 1.35 | 0.85 | 0.76 | | |
| tri | Hf | Ta | W | Re | Os | Ir | Pt | Au | Hf | Ta | W | Re | Os | Ir | Pt | Au | Hf | Ta | W | Re | Os | Ir | Pt | Au | Hf | Ta | W | Re | Os | Ir | Pt | Au | | | | |
| | 0.66 | 1.00 | 1.35 | 1.27 | 1.77 | 1.35 | 0.98 | 0.70 | 0.67 | 0.74 | 0.94 | 1.29 | 1.34 | 1.35 | 0.85 | 0.76 | 0.67 | 0.74 | 0.94 | 1.29 | 1.34 | 1.35 | 0.85 | 0.76 | 0.67 | 0.74 | 0.94 | 1.29 | 1.34 | 1.35 | 0.85 | 0.76 | | | | |
| | 0.51 | 0.61 | 0.67 | 0.54 | 0.61 | 0.74 | 0.86 | 0.97 | 0.63 | 0.82 | 0.83 | 0.71 | 0.73 | 0.67 | 0.69 | 0.59 | 0.57 | 0.70 | 0.62 | 0.71 | 0.68 | 0.95 | 0.78 | 0.57 | 0.70 | 0.64 | 0.50 | 0.73 | 0.66 | 0.99 | 0.78 | 0.41 | 1.39 | 0.73 | 0.54 | |
| hex | Y | Zr | Nb | Mo | Tc | Ru | Rh | Pd | Ag | Y | Zr | Nb | Mo | Tc | Ru | Rh | Pd | Ag | Y | Zr | Nb | Mo | Tc | Ru | Rh | Pd | Ag | Y | Zr | Nb | Mo | Tc | Ru | Rh | Pd | Ag |
| | 0.45 | 0.55 | 0.57 | 0.55 | 0.55 | 0.71 | 0.87 | 1.01 | 0.62 | 0.71 | 0.68 | 0.95 | 0.78 | 0.57 | 0.70 | 0.64 | 0.50 | 0.62 | 0.71 | 0.68 | 0.95 | 0.78 | 0.57 | 0.70 | 0.64 | 0.50 | 0.62 | 0.71 | 0.68 | 0.95 | 0.78 | 0.57 | 0.70 | 0.64 | 0.50 | |
| | 0.53 | 0.64 | 0.62 | 0.62 | 0.82 | 0.95 | 0.89 | 0.73 | 0.66 | 0.99 | 0.78 | 0.41 | 1.39 | 0.73 | 0.54 | 0.73 | 0.66 | 0.99 | 0.78 | 0.41 | 1.39 | 0.73 | 0.54 | 0.73 | 0.66 | 0.99 | 0.78 | 0.41 | 1.39 | 0.73 | 0.54 | | | | | |
| ort | 0.50 | 0.54 | 0.55 | 0.50 | 0.49 | 0.51 | 0.57 | 0.34 | 0.32 | 0.41 | 0.46 | 0.50 | 0.43 | 0.31 | 0.43 | 0.72 | 0.39 | 0.30 | 0.43 | 0.47 | 0.52 | 0.56 | 0.70 | 0.89 | 1.01 | 0.55 | 0.28 | 0.43 | 0.50 | 0.55 | 0.67 | 0.67 | 0.89 | 0.56 | 0.38 | |
| | Y | Zr | Nb | Mo | Tc | Ru | Rh | Pd | Ag | Y | Zr | Nb | Mo | Tc | Ru | Rh | Pd | Ag | Y | Zr | Nb | Mo | Tc | Ru | Rh | Pd | Ag | Y | Zr | Nb | Mo | Tc | Ru | Rh | Pd | Ag |
| | 0.56 | 0.54 | 0.58 | 0.71 | 0.90 | 0.98 | 0.74 | 0.54 | 0.75 | 0.43 | 0.47 | 0.52 | 0.56 | 0.70 | 0.89 | 1.01 | 0.55 | 0.28 | 0.43 | 0.47 | 0.52 | 0.56 | 0.70 | 0.89 | 1.01 | 0.55 | 0.28 | 0.43 | 0.50 | 0.55 | 0.67 | 0.67 | 0.89 | 0.56 | 0.38 | |
| tri | Hf | Ta | W | Re | Os | Ir | Pt | Au | Hf | Ta | W | Re | Os | Ir | Pt | Au | Hf | Ta | W | Re | Os | Ir | Pt | Au | Hf | Ta | W | Re | Os | Ir | Pt | Au | | | | |
| | 0.53 | 0.63 | 0.83 | 0.31 | 1.13 | 0.82 | 0.57 | 0.37 | 0.43 | 0.50 | 0.55 | 0.67 | 0.67 | 0.89 | 0.56 | 0.38 | 0.43 | 0.50 | 0.55 | 0.67 | 0.67 | 0.89 | 0.56 | 0.38 | 0.43 | 0.50 | 0.55 | 0.67 | 0.67 | 0.89 | 0.56 | 0.38 | | | | |
| | 0.40 | 0.28 | 0.19 | 0.08 | 0.22 | 0.40 | 0.14 | 0.79 | 0.75 | 0.50 | 0.35 | 0.29 | 0.31 | 0.20 | 0.09 | 0.32 | 0.79 | 0.75 | 0.50 | 0.35 | 0.29 | 0.31 | 0.20 | 0.09 | 0.32 | 0.79 | 0.75 | 0.50 | 0.35 | 0.29 | 0.31 | 0.20 | 0.09 | 0.32 | | |
| hex | Y | Zr | Nb | Mo | Tc | Ru | Rh | Pd | Ag | Y | Zr | Nb | Mo | Tc | Ru | Rh | Pd | Ag | Y | Zr | Nb | Mo | Tc | Ru | Rh | Pd | Ag | Y | Zr | Nb | Mo | Tc | Ru | Rh | Pd | Ag |
| | 0.46 | 0.35 | 0.26 | 0.15 | 0.11 | 0.25 | 0.53 | 0.64 | 0.66 | 0.62 | 0.52 | 0.63 | 0.58 | 0.34 | 0.45 | 0.36 | 0.25 | 0.66 | 0.62 | 0.52 | 0.63 | 0.58 | 0.34 | 0.45 | 0.36 | 0.25 | 0.66 | 0.62 | 0.52 | 0.63 | 0.58 | 0.34 | 0.45 | 0.36 | 0.25 | |
| | 0.29 | 0.28 | 0.18 | 0.15 | 0.29 | 0.62 | 0.77 | 0.63 | 0.47 | 0.63 | 0.59 | 0.11 | 0.88 | 0.42 | 0.38 | 0.63 | 0.47 | 0.63 | 0.59 | 0.11 | 0.88 | 0.42 | 0.38 | 0.63 | 0.47 | 0.63 | 0.59 | 0.11 | 0.88 | 0.42 | 0.38 | | | | | |
| ort | 0.19 | 0.38 | 0.52 | 0.69 | 0.56 | 0.52 | 0.46 | 0.31 | 0.26 | 0.25 | 0.39 | 0.51 | 0.64 | 0.44 | 0.48 | 0.49 | 0.33 | 0.30 | 0.19 | 0.38 | 0.60 | 0.73 | 0.84 | 0.82 | 0.63 | 0.43 | 0.33 | 0.39 | 0.55 | 0.68 | 0.78 | 0.61 | 0.62 | 0.44 | 0.38 | |
| | Y | Zr | Nb | Mo | Tc | Ru | Rh | Pd | Ag | Y | Zr | Nb | Mo | Tc | Ru | Rh | Pd | Ag | Y | Zr | Nb | Mo | Tc | Ru | Rh | Pd | Ag | Y | Zr | Nb | Mo | Tc | Ru | Rh | Pd | Ag |
| | 0.15 | 0.31 | 0.62 | 0.83 | 0.87 | 0.82 | 0.55 | 0.43 | 0.45 | 0.19 | 0.38 | 0.60 | 0.73 | 0.84 | 0.82 | 0.63 | 0.43 | 0.33 | 0.19 | 0.38 | 0.60 | 0.73 | 0.84 | 0.82 | 0.63 | 0.43 | 0.33 | 0.39 | 0.55 | 0.68 | 0.78 | 0.61 | 0.62 | 0.44 | 0.38 | |
| tri | Hf | Ta | W | Re | Os | Ir | Pt | Au | Hf | Ta | W | Re | Os | Ir | Pt | Au | Hf | Ta | W | Re | Os | Ir | Pt | Au | Hf | Ta | W | Re | Os | Ir | Pt | Au | | | | |
| | 0.36 | 0.60 | 0.84 | 0.66 | 0.84 | 0.54 | 0.40 | 0.18 | 0.39 | 0.55 | 0.68 | 0.78 | 0.61 | 0.62 | 0.44 | 0.38 | 0.39 | 0.55 | 0.68 | 0.78 | 0.61 | 0.62 | 0.44 | 0.38 | 0.39 | 0.55 | 0.68 | 0.78 | 0.61 | 0.62 | 0.44 | 0.38 | | | | |
| | 0.24 | 0.28 | 0.29 | 0.33 | 0.26 | 0.35 | 0.43 | 0.36 | 0.22 | 0.34 | 0.45 | 0.39 | 0.38 | 0.17 | 0.17 | 0.12 | 0.16 | 0.33 | 0.34 | 0.45 | 0.39 | 0.38 | 0.17 | 0.17 | 0.12 | 0.16 | 0.33 | 0.34 | 0.45 | 0.39 | 0.38 | 0.17 | 0.17 | 0.12 | 0.16 | 0.33 |
| hex | Y | Zr | Nb | Mo | Tc | Ru | Rh | Pd | Ag | Y | Zr | Nb | Mo | Tc | Ru | Rh | Pd | Ag | Y | Zr | Nb | Mo | Tc | Ru | Rh | Pd | Ag | Y | Zr | Nb | Mo | Tc | Ru | Rh | Pd | Ag |
| | 0.19 | 0.28 | 0.43 | 0.41 | 0.45 | 0.58 | 0.64 | 0.48 | 0.25 | 0.40 | 0.57 | 0.47 | 0.31 | 0.26 | 0.41 | 0.32 | 0.28 | 0.25 | 0.40 | 0.57 | 0.47 | 0.31 | 0.26 | 0.41 | 0.32 | 0.28 | 0.25 | 0.40 | 0.57 | 0.47 | 0.31 | 0.26 | 0.41 | 0.32 | 0.28 | |
| | 0.30 | 0.37 | 0.37 | 0.42 | 0.55 | 0.66 | 0.46 | 0.43 | 0.47 | 0.35 | 0.27 | 0.19 | 0.27 | 0.35 | 0.27 | 0.43 | 0.47 | 0.35 | 0.27 | 0.19 | 0.27 | 0.35 | 0.27 | 0.43 | 0.47 | 0.35 | 0.27 | 0.19 | 0.27 | 0.35 | 0.27 | | | | | |
| ort | 0.11 | 0.39 | 0.39 | 0.46 | 0.36 | 0.33 | 0.32 | 0.20 | 0.07 | 0.17 | 0.39 | 0.44 | 0.42 | 0.32 | 0.33 | 0.32 | 0.18 | 0.11 | 0.05 | 0.31 | 0.38 | 0.42 | 0.46 | 0.41 | 0.28 | 0.18 | 0.10 | 0.33 | 0.37 | 0.39 | 0.48 | 0.39 | 0.32 | 0.22 | 0.18 | |
| | Y | Zr | Nb | Mo | Tc | Ru | Rh | Pd | Ag | Y | Zr | Nb | Mo | Tc | Ru | Rh | Pd | Ag | Y | Zr | Nb | Mo | Tc | Ru | Rh | Pd | Ag | Y | Zr | Nb | Mo | Tc | Ru | Rh | Pd | Ag |
| | 0.24 | 0.40 | 0.50 | 0.45 | 0.39 | 0.24 | 0.14 | 0.05 | 0.31 | 0.38 | 0.42 | 0.46 | 0.41 | 0.28 | 0.18 | 0.10 | 0.05 | 0.31 | 0.38 | 0.42 | 0.46 | 0.41 | 0.28 | 0.18 | 0.10 | 0.33 | 0.37 | 0.39 | 0.48 | 0.39 | 0.32 | 0.22 | 0.18 | | | |
| tri | Hf | Ta | W | Re | Os | Ir | Pt | Au | Hf | Ta | W | Re | Os | Ir | Pt | Au | Hf | Ta | W | Re | Os | Ir | Pt | Au | Hf | Ta | W | Re | Os | Ir | Pt | Au | | | | |
| | 0.29 | 0.41 | 0.50 | 0.36 | 0.41 | 0.19 | 0.28 | 0.33 | 0.37 | 0.39 | 0.48 | 0.39 | 0.32 | 0.22 | 0.18 | 0.33 | 0.37 | 0.39 | 0.48 | 0.39 | 0.32 | 0.22 | 0.18 | 0.33 | 0.37 | 0.39 | 0.48 | 0.39 | 0.32 | 0.22 | 0.18 | | | | | |
| | 0.16 | 0.34 | 0.45 | 0.44 | 0.40 | 0.42 | 0.39 | 0.31 | 0.23 | 0.18 | 0.29 | 0.21 | 0.25 | 0.20 | 0.21 | 0.19 | 0.20 | 0.21 | 0.11 | 0.25 | 0.23 | 0.20 | 0.22 | 0.22 | 0.14 | 0.07 | 0.26 | 0.20 | 0.19 | 0.25 | 0.19 | 0.18 | 0.05 | | | |
| hex | Y | Zr | Nb | Mo | Tc | Ru | Rh | Pd | Ag | Y | Zr | Nb | Mo | Tc | Ru | Rh | Pd | Ag | Y | Zr | Nb | Mo | Tc | Ru | Rh | Pd | Ag | Y | Zr | Nb | Mo | Tc | Ru | Rh | Pd | Ag |
| | 0.04 | 0.22 | 0.38 | 0.41 | 0.38 | 0.38 | 0.27 | 0.22 | 0.11 | 0.25 | 0.23 | 0.20 | 0.22 | 0.22 | 0.14 | 0.07 | 0.11 | 0.25 | 0.23 | 0.20 | 0.22 | 0.22 | 0.14 | 0.07 | 0.11 | 0.25 | 0.23 | 0.20 | 0.22 | 0.22 | 0.14 | 0.07 | | | | |
| | 0.26 | 0.41 | 0.38 | 0.35 | 0.37 | 0.28 | 0.05 | 0.26 | 0.20 | 0.19 | 0.25 | 0.19 | 0.18 | 0.05 | 0.26 | 0.20 | 0.19 | 0.25 | 0.19 | 0.18 | 0.05 | 0.26 | 0.20 | 0.19 | 0.25 | 0.19 | 0.18 | 0.05 | | | | | | | | |

Figure 4.11 Open-circuit voltage (OCV) values corresponding to the first layer adsorption of Li, Na, Mg, and Al on various M_2B_2 MBenes.

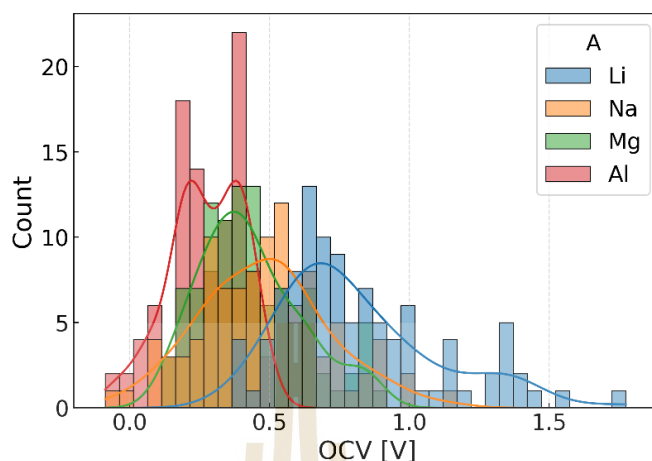


Figure 4.12 Distribution of open-circuit voltage (OCV) values at first-layer adsorption on M_2B_2 MBenes, grouped by carrier species ($A = \text{Li, Na, Mg, Al}$).

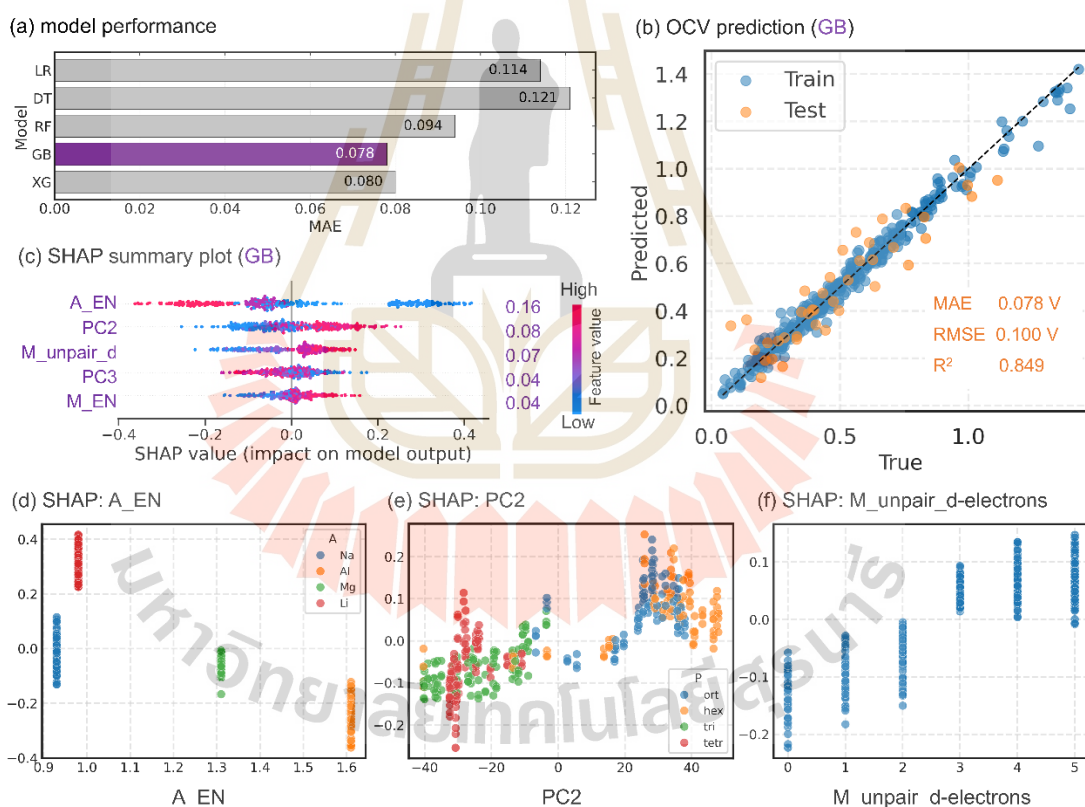


Figure 4.13 Machine learning prediction and SHAP-based interpretation of open-circuit voltage (OCV) values at first-layer adsorption on various M_2B_2 . (a) Model comparison showing Gradient Boosting (GB) as the best-performing regressor. (b) Parity plot of predicted vs. DFT-calculated OCV values using the GB model. (c) SHAP summary plot identifying the five selected features: EN of the carrier (A_EN), PC2, number of unpaired d-electrons of M, PC3, and EN of M (M_EN). (d–f) SHAP dependence plots.

To better understand the factors governing the OCV, SHAP analysis was applied to the trained Gradient Boosting model. Among all five selected features, the EN of A (A_EN) emerged as the most influential, with a SHAP importance of 0.16 as shown in **Figure 4.13c**. Other contributors include PC2 (0.08), the number of unpaired d electrons of M (0.07), PC3 (0.04), and the EN of M (0.04). In the following discussion, we examine how these features influence the predicted OCV in relation to the carrier species, crystal phase, and the constituent transition metal.

In the case of carrier species (A), the SHAP analysis reveals an inverse correlation between EN and OCV: carriers with higher EN, such as Al, tend to exhibit lower OCVs. However, this trend cannot be directly interpreted from interaction alone, since OCV is defined as the adsorption energy normalized by the number of electrons transferred (z), i.e., $OCV \propto |E_{ads}|/z$. As z significantly influences OCV, we investigated both the absolute interaction energy and its normalization by z to gain a clearer understanding.

Adsorption of carrier species on a 2D monolayer is an inherently complex process involving multiple interacting phenomena. Previous studies have introduced theoretical frameworks to describe this adsorption by decomposing the total adsorption energy into distinct contributions that reflect different physical origins (Chaney et al., 2021; Dou and Fyta, 2020; Gong et al., 2021). Building on these frameworks, we adapted and simplified the approach by resolving the total adsorption energy ($E_{adsorption}$) into four contributing components, as illustrated in **Figure 4.14a**.

The first component is cohesive energy ($E_{cohesive}$), which accounts for the dissociation of the carrier in bulk phase into isolated atoms. The second component is lateral interaction energy ($E_{lateral}$), arising from interactions between carrier atoms arranged according to the adsorption configuration. This includes both repulsive forces at too short distances and cohesive interaction at too long distances. Deviations from optimal interatomic distance introduce an energy penalty. The third component is distortion energy ($E_{distort}$), representing the elastic energy associated with the structural relaxation of the M_2B_2 in response to adsorption. Finally, the most complex component is coupling energy ($E_{coupling}$), which captures the direct interaction between each carrier atom and the monolayer surface. This term reflects the coupling interactions that arise from different bonding mechanisms. In our case, the bonding

character may appear to lie in the metallic regime, encompassing charge redistribution, electronic screening, and orbital hybridization.

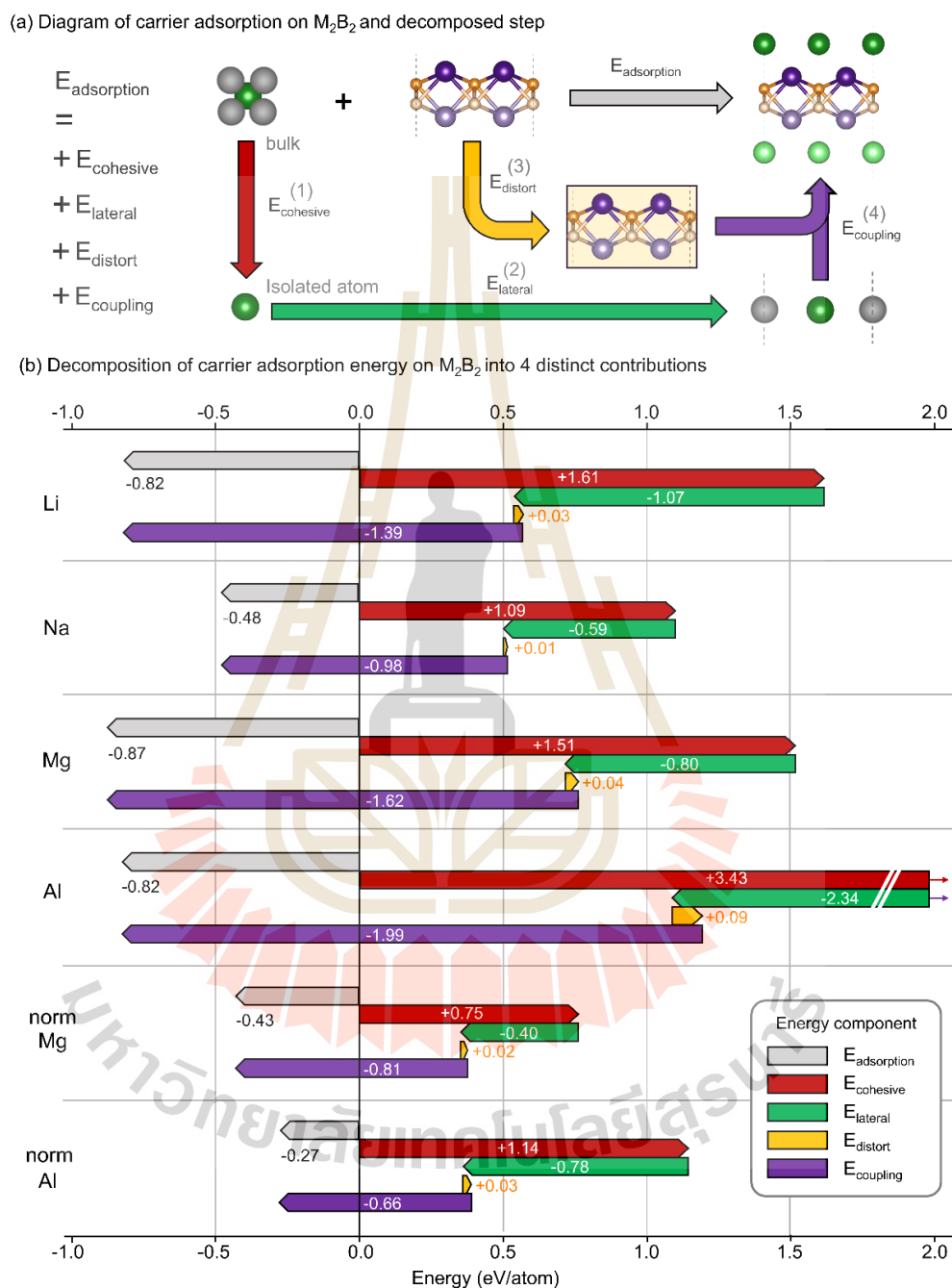


Figure 4.14 Decomposed adsorption energy components for different carriers on M_2B_2 .

(a) Schematic of adsorption energy ($E_{\text{adsorption}}$) split into four components: cohesive (E_{cohesive}), lateral interaction (E_{lateral}), distortion (E_{distort}), and coupling (E_{coupling}) energies. (b) Averaged component energies (eV/atom) for Li, Na, Mg, and Al. The averaged energies normalized by z are shown for Mg and Al directly compared to OCV.

For each charge carrier adsorbed onto M_2B_2 in different structural phases, we explicitly calculated $E_{cohesive}$, $E_{lateral}$, and $E_{distort}$ using DFT-based reaction energies, following the decomposition diagram shown in **Figure 4.14b**. The remaining component, $E_{coupling}$, was obtained as a residual by subtracting the sum of the other three components from the total adsorption energy.

To further investigate the impact of carrier species on each component of the total adsorption energy. The average total and component energies across all crystal phases and transition metals for each carrier species are used as a representative and shown in **Figure 4.14b**. Our results reveal several notable trends. Although the total adsorption energy does not exhibit a clear monotonic dependence on the charge carrier, the underlying components do. Al exhibits the strongest $E_{cohesive} + E_{lateral}$ followed by Mg, Li, and Na. This trend reflects the fundamental nature of metallic bonding, where adsorption involves the energy cost of detaching carrier atoms from their bulk state and rearranging them into the adsorption configuration. The observed order (Al > Mg > Li > Na) corresponds well with classical metallic bond strength, as described by the electron sea model. A parallel trend is observed in $E_{coupling}$, with Al exhibiting the strongest interaction with the surface. This is attributed to its higher valence electron count and smaller ionic radius, which enhance electrostatic attraction to surface atoms, as supported by Shannon ionic radii order Al (0.39 Å) < Mg (0.57 Å) < Li (0.59 Å) < Na (0.99 Å) at coordination number of four (Ahrens, 1952). We also find that the $E_{distort}$ are negligible across all species, suggesting that the coupling term and carrier reorganizing term play the main role in overall adsorption energetics.

Although adsorption energy is a critical descriptor, it does not directly correspond to OCV, as the latter depends on the adsorption energy normalized by z . In **Figure 4.14b**, normalization significantly changes the trend: despite Al and Mg showing stronger absolute adsorption energies, their high valency (Al: $z = 3$, Mg: $z = 2$) reduces their effective contribution to OCV. Consequently, the normalized interaction strength and OCV follows the trend: Li > Na > Mg > Al. From SHAP analysis, this is correlated with EN of carriers where: carriers with higher EN, such as Al, tend to exhibit lower OCVs. We hypothesize that the apparent correlation may arise because EN is intrinsically related to z , which acts as the normalization factor in the OCV calculation.

To investigate the influence of crystal phase on OCV, the distribution of OCV values across all carriers and phases is presented in **Figure 4.15a**. For a given carrier species, the ort- and hex- M_2B_2 generally result in higher OCVs compared to the tri- and tetr- M_2B_2 . This observation is consistent with the SHAP dependence plot of PC2 (see **Figure 4.13e**), where structures associated with positive PC2 values, primarily ort- and hex- M_2B_2 , correspond to higher OCVs. Although the physical meaning of PC2 is not fully understood, the trend may reflect differences in coordination number of M, leading to differences in coupling interaction at the adsorption sites.

To further analyze this phase dependence, we focus on the lateral interaction energy between carrier atoms arranged in adsorption configuration, which is strongly influenced by lattice parameters and phase. In **Figure 4.15b**, M_2B_2 monolayers exhibit two main adsorption patterns: rectangular arrangements (ort- and tetr-phases), and hexagonal arrangements (hex- and tri-phases). These configurations dictate the distance between carrier atoms (A–A distance), which vary with both crystal phase and atomic radius of the transition metal. The boxplots summarize a deviation of these A–A distances for each crystal phase. The median A–A distance within each phase was primarily used as the representative value in our discussion. The tri-phase tends to have the shortest A–A distances, while hex and ort structures are more moderate.

To assess the impact of these distances on OCV, we calculated normalized lateral interaction energies ($E_{lateral}/z$) for all carriers, using the hexagonal arrangement as a reference due to its higher stability and packing factor (see **Figure 4.15b**). For Li and Mg, the lateral interaction energy shows little variation across phases, suggesting that OCV differences are primarily governed by other contributions such as coupling energy. In contrast, Na exhibits the highest lateral energy penalty, particularly in the tri phase, where the Na–Na distance is much shorter than its equilibrium spacing. This leads to strong repulsive interactions, destabilizing adsorption layer, and significantly lowers the resulting OCV. Al shows an opposite trend. Its small atomic radius results in an equilibrium Al–Al spacing shorter than those observed in all phases, reducing lateral cohesion and increasing energy penalties. However, in the tri phase, the Al–Al distance is relatively closer to its equilibrium spacing compared to other phases, which reduces the lateral interaction and results in relatively higher OCV.

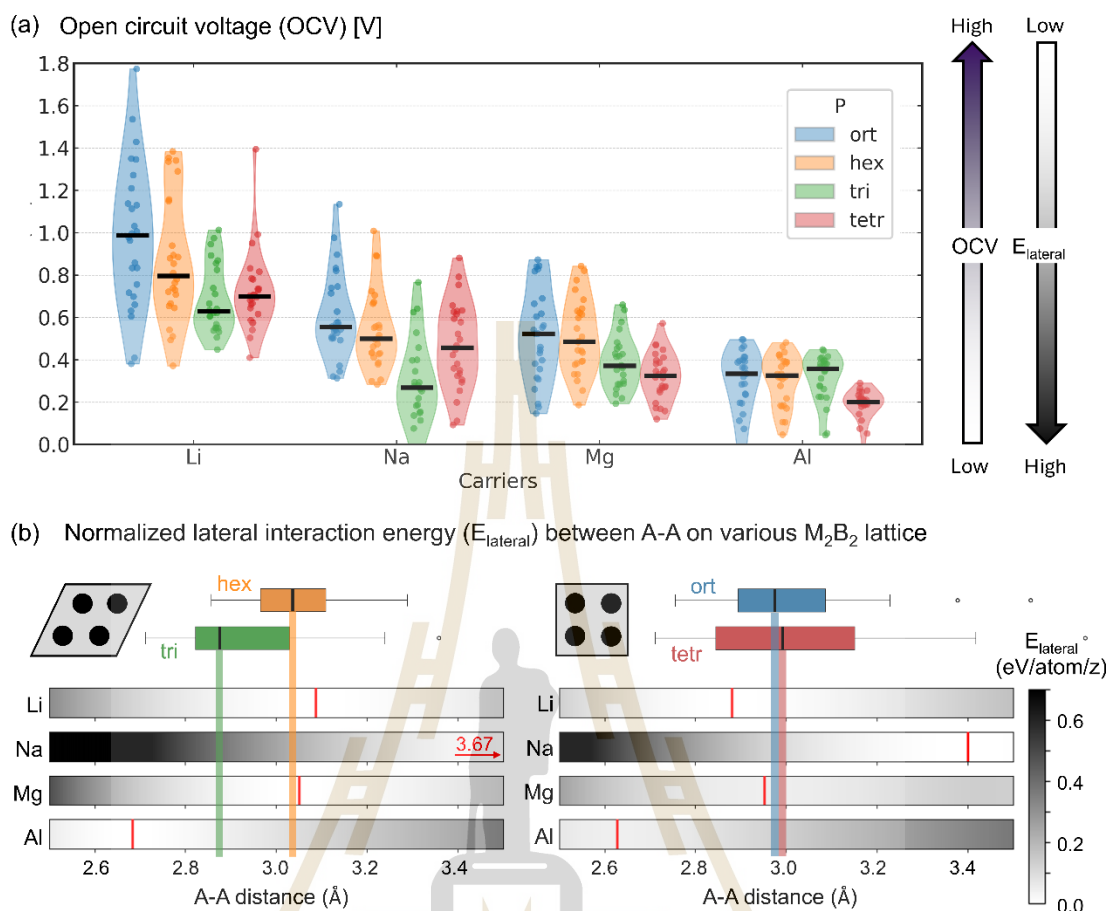


Figure 4.15 Phase dependent on lateral interaction energies of various carrier species (a) Violin plots of open-circuit voltage (OCV) distributions for Li, Na, and Mg, Al across four M_2B_2 phases. Median is represented as a black line. (b) Normalized lateral interaction energy ($E_{lateral}/z$) as a function of A-A distance for hexagonal (hex, tri) and rectangular (ort, tetr) adsorption configurations. Gray bars show the energy landscape for each carrier species, referenced to the hexagonal arrangement (set to 0). Box plots represent the A-A distance distributions within each phase, with the median as a representative value. In the ort-phase, A-A distances are averaged along the a and b directions to account for lattice anisotropy. Lower normalized $E_{lateral}$ generally indicate stronger adsorption and correspond to higher OCV.

In addition, the influence of the M on OCV was also discussed. Based on SHAP analysis, the OCV generally shows a positive correlation with the number of unpaired d-electrons and, to some extent, the EN of M. This trend reflects the role of M in modulating the coupling energy between the M_2B_2 substrate and the adsorbed carriers.

Although the underlying physical mechanism is not entirely clear, a higher number of unpaired d-electrons of M may enhance electronic interactions at the adsorption site, potentially leading to stronger coupling or bond formation, leading to higher OCV values.

It is important to note that the predicted OCV values in this study are intended to provide general trends for high-throughput screening rather than exact agreement with experimental measurements. Even among computational studies, direct comparison between our calculated OCV values and those reported in the literature is challenging due to methodological differences across studies. OCV is highly sensitive to how adsorption of carrier species is modeled, particularly the concentration intervals or step of adding carrier atoms. In this work, carrier atoms were added layer-by-layer on both sides of the monolayer simultaneously. In contrast, other studies may adopt different intervals, such as one-sided layer-by-layer or even atom-by-atom addition, leading to discrepancies in the resulting OCV values. In fact, atom-by-atom adsorption model might be more realistic and appropriate for a detailed study, but it is beyond the scope of this screening work. Furthermore, variations in computational settings such as the vdW correction can significantly affect both adsorption energy and OCV profile. For example, our predicted OCV for Li adsorption on ort-Fe₂B₂ is 1.11 V, whereas previously reported values range from 0.33, 1.08, and 4.7 V (Liu et al., 2023; Sun et al., 2017; Y. Wang et al., 2024). This wide variation underscores the sensitivity of OCV predictions to modeling parameters not only for Li adsorption on ort-Fe₂B₂ but across other systems.

4.3.3 Ionic conductivity: diffusion barriers and pathways

Beyond charge carrier storage capacity, efficient carrier transport is critical for achieving a better charge-discharge rate, leading to high performance MIBs. The rate capability of an anode material is closely governed by its ionic conductivity, which in turn depends on the diffusion of carrier species, i.e., Li, Na, Mg, and Al, across the surface of the M₂B₂ monolayer. To assess this kinetic aspect, we modeled the diffusion of a single carrier atom on the surface of each M₂B₂ composition and crystal phase using the CINEB method as detailed in Section 3.4.3.

For each crystal phase, inequivalent diffusion pathways were systematically evaluated based on symmetry considerations and the locations of the most stable adsorption sites (**Figure 4.16**). Diffusion was modeled as carrier migration between adjacent adsorption sites along distinct crystallographic directions. In the *ort*-phase, carriers preferentially adsorb at hollow sites coordinated by four M atoms, with two possible diffusion paths along the *a*- and *b*-directions, labeled P1 and P2, respectively. Typically, the direction with the lower diffusion barrier dominates, leading to quasi-one-dimensional transport unless both barriers are comparable. The lower value was taken as the effective diffusion barrier. In hex- and tri- phases, the preferred adsorption site is the hollow position coordinated by three M atoms. Diffusion occurs through a hexagonally connected network of hollow sites (P1), allowing 2D transport. In the tetr-

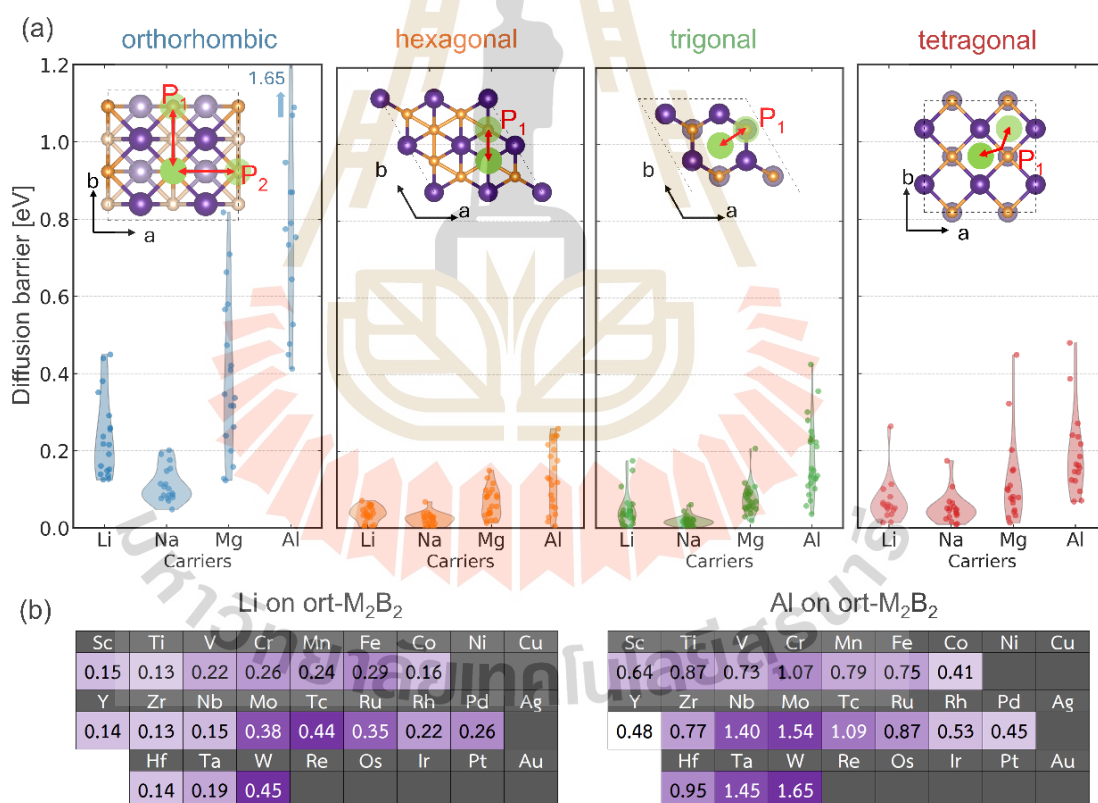


Figure 4.16 Diffusion barriers of Li, Na, Mg, and Al on M₂B₂ monolayers. (a) Violin plots of effective diffusion barriers across four crystal phases, with insets showing representative diffusion pathways (P₁, P₂). (b) Periodic table maps of diffusion barriers for Li and Al diffusion on *ort*-M₂B₂, highlighting transition metal dependence.

phase, diffusion was modeled along the diagonal path (P1) between neighboring hollow sites, which defines a representative 2D transport network. These effective diffusion pathways capture the intrinsic carrier mobility characteristics of each M_2B_2 phase. In all cases, the diffusion barrier serves as a quantitative descriptor of transport of carrier species on M_2B_2 monolayer. These barriers are presented as violin plots in **Figure 4.16**, highlighting the distribution for each carrier species and crystal phase combination. Lower diffusion barriers are indicative of more rapid carrier transport and are thus favorable for high-rate battery applications.

The results revealed a clear dependence on crystal phase. The high diffusion barriers in *ort*- M_2B_2 can be attributed to a strong initial-state bonding environment. In the initial adsorption state, the carrier atom is coordinated to four M and one B atom, with a particularly strong and short carrier-B bond that provides significant stabilization. During diffusion, the carrier must break this stable configuration and move into a less favorable transition state, where it is coordinated to only two M atoms. This different coordination led to high diffusion barrier. In contrast, the other phases feature more gradual changes in coordination, similar coordination between initial and transition states, supporting much lower diffusion barriers.

Carrier species significantly influences the behavior of diffusion on M_2B_2 monolayers, especially on the *ort*- M_2B_2 . As depicted in **Figure 4.16a**, the overall distribution of diffusion barriers generally follows the trend $Al > Mg > Li > Na$, which could be understood by again the interaction between carrier species and M on surface similar to the discussion on coupling energy. Al, with the highest charge ($z = 3$) and relatively small radius, exhibit the strongest interaction with the surface. This results in a higher stable initial state, leading to a deeper adsorption well and a corresponding higher diffusion barrier. Mg ($z = 2$) also interacts strongly, resulting in moderate barriers. In contrast, Li and Na ($z = 1$) display weaker interactions with the surface, showing shallower potential wells and lower diffusion barriers. Between them, Na with larger atomic radius and lower electron density, reduces its polarizing ability and surface interaction, leading to even lower diffusion barriers compared to Li.

The influence of the M on diffusion barriers was further investigated, particularly for the *ort*- M_2B_2 where comparatively higher barriers were observed. As shown in **Figure**

4.16b, the diffusion barriers for both Li and Al exhibit a nonmonotonic trend across transition metal series. Specifically, intermediate M, such as Cr, Mn, and Fe, tend to produce higher diffusion barriers, while early M (e.g., Sc, Ti) and late M (e.g., Ni, Cu) result in lower diffusion barriers. This trend appears to correlate with the number of unpaired d-electrons of the M. The higher diffusion barriers observed for transition metals in the middle of the d-block may be attributed to strengthen the interaction between the carrier species and M of M_2B_2 similar to the explanation of layer adsorption. This results in deeper adsorption wells and consequently higher energy barriers for diffusion.

Some data points are missing in **Figure 4.16** due to structural distortions observed during single-atom adsorption. These distortions indicate instability in the adsorption configuration, though the underlying causes remain unclear and warrant further investigation.

To validate our findings, our predicted pathway of carrier atom diffusion on M_2B_2 is in good agreement with previous calculations. For instance, our results indicate that the Li atom predominantly diffuses along *a*-direction of the *ort*- Fe_2B_2 crystal, consistent with earlier studies. (Guo et al., 2017; Liu et al., 2023; Y. Wang et al., 2024). The associated diffusion energy barrier of 0.29 eV falls within the range of reported values, which are 0.24 eV (Guo et al., 2017; Liu et al., 2023) and 0.37 eV (Y. Wang et al., 2024). Similarly, our predicted diffusion barriers of Li atom on other *ort*- M_2B_2 show slight deviations or equivalence to previously reported values, as detailed in **Table 4.1**, with discrepancies typically within 0.1 eV. These differences may stem from variations in computational parameters, such as the application of vdW corrections. For the *hex*- M_2B_2 phase, our predictions can be compared with systematic screening conducted by (He et al., 2021). The diffusion barriers for *hex*- M_2B_2 , with M = Sc, Ti, V, Zr, Nb, and Mo are 0.003, 0.006, 0.014, 0.008, 0.036, and 0.049 eV, respectively, which align closely with the values of 0.003, 0.004, 0.017, 0.004, 0.033, and 0.038 eV reported by (He et al., 2021), This similarity could be attributed to comparable computational setups, e.g. the use of DFT-D3 vdW correction and the same supercell size.

In summary, the diffusion behavior of single carrier atom on M_2B_2 monolayers was systematically investigated to evaluate their ionic conductivity. The calculated

barriers reveal clear trends governed by the carrier species, crystal phases, and M, serving as key descriptors for this high-throughput screening. It should be noted, however, that the values were obtained under the assumption of dilute carrier concentration and do not account for factors such as inter-carrier interactions, surface reconstructions, thermal effects, or morphological variations, which may influence diffusion under realistic operating conditions.

Table 4.1 Comparison of Li diffusion barriers (in eV) on *ort*-M₂B₂ from this study and literature values: i) (Guo et al., 2017), ii) (Jia et al., 2019), iii) (J. Wang et al., 2019), iv) (Li et al., 2022), v) (Liu et al., 2023), and vi) (Y. Wang et al., 2024).

| M | This work | i) | ii) | iii) | iv) | v) | vi) |
|----|-----------|------|------|------|------|------|------|
| Sc | 0.08 | | | | 0.11 | | |
| Ti | 0.13 | | | 0.11 | 0.11 | | |
| V | 0.22 | | 0.22 | | 0.26 | | |
| Cr | 0.26 | | 0.28 | | | | 0.44 |
| Mn | 0.24 | | 0.29 | | | | 0.37 |
| Fe | 0.29 | 0.24 | | | | 0.24 | 0.37 |
| Mo | 0.38 | 0.27 | | | | | |

4.4 Promising M₂B₂ anode candidates

To systematically identify promising M₂B₂ monolayers as anode materials for MIBs, we evaluated their structural, electronic, and electrochemical properties based on the data presented in previous sections. calculated in the previous sections. An ideal anode must meet three key requirements: (1) energetic and dynamic stability, (2) high electronic and ionic conductivity, and (3) favorable electrochemical performance in terms of capacity and voltage. In this section, we integrate these aspects into a comprehensive selection workflow by first applying a set of pre-screening criteria, followed by a comparative analysis of OCV and gravimetric capacity.

The initial screening focused on eliminating monolayers that lack structural or electronic feasibility. Only M₂B₂ compositions satisfying all of the following criteria were considered viable for further electrochemical evaluation:

- **Cohesive energy > 4.5 eV/atom**, to ensure sufficient energetic stability and chemical bonding strength. This threshold was chosen to be slightly below the cohesive energy of $\text{ort-Cr}_2\text{B}_2$, one of the experimentally synthesized MBenes with the lowest reported cohesive energy.
- **No imaginary phonon modes**, indicating dynamic stability of the lattice under small perturbations.
- **Metallic-like electronic structure**, as determined by a no-gap density of states at the Fermi level, to guarantee fast electron transport during charge/discharge cycles.
- **Diffusion barrier < 0.3 eV**, to ensure efficient mobility of adsorbed metal carriers on the surface, enabling high charge–discharge rates. This cutoff was selected to be slightly below the reported diffusion barrier of Li in graphite (0.31 eV) (Persson et al., 2010).

These pre-screening criteria serve as foundational filters to ensure that only structurally and electronically viable M_2B_2 candidates are retained for subsequent evaluation of their electrochemical performance, specifically in terms of OCV and capacity.

Based on the pre-screening criteria, several M_2B_2 monolayers were excluded. Generally, Cu, Ag, and Au were eliminated due to insufficient cohesive energy. In terms of dynamic stability, many late M, especially those from the Co group onward, exhibited imaginary phonon modes and were excluded. Additionally, several early M in tri- and tetra-phases also failed phonon stability. No exclusions were made based on electronic conductivity as all monolayers exhibited metallic character. Most hex-, tri-, and tetra-phases passed the diffusion barrier criterion across all carriers, while ort-phase showed carrier-dependence: Na generally passed, Li was acceptable for 3d and 4d–5d metals with low d-electron counts, and Al was mostly excluded. In addition, Tc compositions were also eliminated due to their radioactivity.

To assess the electrochemical performance of the viable M_2B_2 monolayers, we compared their gravimetric capacity and OCV across four carrier species. These two properties serve as key indicators of anode performance, where high capacity reflects strong charge-storage potential, and low OCV is desirable for achieving a high overall cell voltage when paired with common cathode materials. The calculated results are

summarized in **Figure 4.17**, which plots capacity versus OCV landscape for all candidates. The ideal anode materials lie in the upper-left region of each plot, exhibiting high capacity and low OCV, which together contribute to high energy density and favorable battery performance.

For Li-ion batteries, several candidates clearly occupy the ideal region, particularly *ort-Sc*₂B₂, *hex-Sc*₂B₂, *tri-Cr*₂B₂, *tri-Ti*₂B₂, and *ort-Ti*₂B₂. These systems achieve high capacities around 1000 mAh/g, primarily due to their low molecular weights and ability to adsorb up to three layers of Li ($n_{max} = 3$). Their OCVs fall within a practical range of 0.4–0.6 V, supporting safe operation while maintaining strong cell voltage. In contrast, *ort-Y*₂B₂ and *hex-Y*₂B₂ exhibit slightly lower capacities (~600 mAh/g) due to the higher atomic mass but retain low OCV values.

For Na-ion batteries, the number of viable candidates is more limited due to weaker interactions with Na, resulting in a low number of adsorbed layers (often $n_{max} = 1$). Additionally, the higher atomic mass of Na contributes to reduced gravimetric capacity. Among the viable options, *ort-Sc*₂B₂, *ort-Ti*₂B₂, and *hex-Y*₂B₂ exhibit high

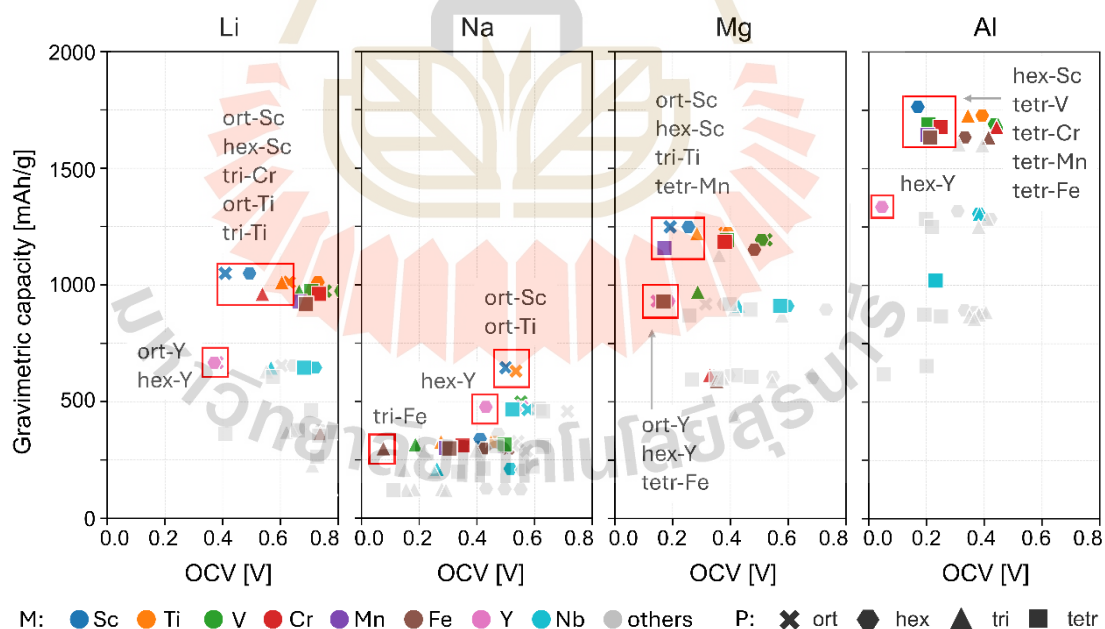


Figure 4.17 Gravimetric capacity versus open-circuit voltage (OCV) for M_2B_2 monolayers evaluated as anode materials for Li-, Na-, Mg-, and Al-ion batteries. An optimal anode should exhibit both high specific capacity and low OCV to ensure high energy density. Promising candidates are highlighted by red rectangles.

capacities ($\sim 500 - 600$ mAh/g) and low OCVs (~ 0.5 V). Notably, tri-V₂B₂ and tri-Fe₂B₂ provide very low OCVs (~ 0.1 V), which is favorable for cell voltage, but their capacities are lower due to limited adsorption layers.

For Mg-ion batteries, top candidates: ort-Sc₂B₂, hex-Sc₂B₂, tri-Ti₂B₂, and tetr-Mn₂B₂ offer high capacities (1000–1300 mAh/g) and low OCVs (0.2-0.3 V). These systems benefit from the divalent nature of Mg. Y-based compounds show slightly lower capacity, despite maintaining comparable OCVs.

For Al-ion batteries, the most promising candidates include hex-Sc₂B₂, tetr-V₂B₂, tetr-Cr₂B₂, tetr-Mn₂B₂, and tetr-Fe₂B₂, offering high capacities up to ~ 1600 mAh/g, enabled by Al trivalence, and low OCVs around 0.2 V. As Al-ion systems typically have low cathode potential, hex-Y₂B₂ with exceptionally low OCVs may also be attractive despite a trade-off in capacity.

The promising M₂B₂ anode candidates generally fall into two groups. Group one includes ort- and hex-phases of Sc, Ti, and Y. These compounds exhibit low OCVs due to their low number of unpaired d-electrons, leading to weaker coupling with carriers. Their capacity benefits from high n_{max} (up to 3 layers) and low atomic mass (especially Sc and Ti). Their high cohesive energy reflects good structural stability among other phases. Although Sc-M₂B₂ offer excellent performance, their cost may limit scalability. Ti and Y provide a better trade-off between performance and availability.

Group two consists of tri- and tetr-phases of V, Cr, Mn, and Fe. These compounds show moderate to low OCVs, attributed to weaker interaction phases and strong lateral repulsion, especially for Na. Despite their higher atomic mass and lower n_{max} , they offer low diffusion barriers and high structural stability (particularly tetr-phase). Additionally, Mn- and Fe-M₂B₂ are especially cost-effective, enhancing their appeal for practical applications. Notably, these phases remain largely unexplored, presenting a promising direction for future theoretical and experimental research.

Compared with commercial anode material based on graphite and Ti₃C₂ MXene benchmark in **Table 4.2**, our selected M₂B₂ MBenes reveals substantial performance advantages for LIB applications. The significant improvement lies in gravimetric capacity: most M₂B₂ compounds offer values exceeding 900 mAh/g, far surpassing the 372 mAh/g of graphite and 320 mAh/g of Ti₃C₂. In terms of OCV, materials such as ort-

Sc₂B₂, hex-Sc₂B₂, hex-Y₂B₂, and tri-Cr₂B₂ exhibit lower OCVs relative to Ti₃C₂, supporting better operating cell voltage. Although other selected M₂B₂ compounds show OCV in the range of 0.6 to 0.7 V, their values remain competitive to 0.62 V of Ti₃C₂. Diffusion barriers further highlight the kinetic superiority of M₂B₂ systems; all exhibit faster Li mobility than graphite, and most also outperform Ti₃C₂, especially in hex-M₂B₂ with ultralow diffusion barrier. These combined properties, high capacity, efficient voltage range, and fast ion transport, establish M₂B₂ monolayers as highly promising anode materials with advantages over traditional graphite and Ti₃C₂ MXene.

Table 4.2: Performance comparison of selected M₂B₂ monolayers with commercial graphite and Ti₃C₂ MXene benchmark as Li-ion battery anodes.

| Material | OCV (V) | Capacity (mAh/g) | Diffusion barrier (eV) | Reference |
|--------------------------------------|---------|------------------|------------------------|------------------------|
| Graphite | ~0.2 | 372 | 0.31 | (Persson et al., 2010) |
| Ti ₃ C ₂ MXene | 0.62 | 320 | 0.07 | (Tang et al., 2012) |
| ort-Sc ₂ B ₂ | 0.41 | 1050 | 0.148 | This work |
| hex-Sc ₂ B ₂ | 0.49 | 1050 | 0.003 | This work |
| tri-Cr ₂ B ₂ | 0.54 | 962 | 0.038 | This work |
| tri-Ti ₂ B ₂ | 0.61 | 1011 | 0.005 | This work |
| tri-V ₂ B ₂ | 0.67 | 974 | 0.024 | This work |
| tetr-Mn ₂ B ₂ | 0.67 | 929 | 0.056 | This work |
| tetr-Fe ₂ B ₂ | 0.69 | 919 | 0.066 | This work |
| hex-Y ₂ B ₂ | 0.37 | 667 | 0.004 | This work |

4.5 References

- Ahrens, L. H. (1952). The use of ionization potentials Part 1. Ionic radii of the elements. *Geochimica et Cosmochimica Acta*, 2(3), 155–169.
- Bo, T., Liu, P.-F., Xu, J., Zhang, J., Chen, Y., Eriksson, O., Wang, F., and Wang, B.-T. (2018). Hexagonal Ti₂B₂ monolayer: a promising anode material offering high rate capability for Li-ion and Na-ion batteries. *Physical Chemistry Chemical Physics*, 20(34), Article 34.

- Bo, T., Liu, P.-F., Zhang, J., Wang, F., and Wang, B.-T. (2019). Tetragonal and trigonal Mo₂B₂ monolayers: two new low-dimensional materials for Li-ion and Na-ion batteries. *Physical Chemistry Chemical Physics*, 21(9), Article 9.
- Boring, A. M., and Smith, J. L. (2000). *Plutonium Condensed-Matter Physics*. 26.
- Chaney, G., Ibrahim, A., Ersan, F., Çakır, D., and Ataca, C. (2021). Comprehensive Study of Lithium Adsorption and Diffusion on Janus Mo/WXY (X, Y = S, Se, Te) Using First-Principles and Machine Learning Approaches. *ACS Applied Materials & Interfaces*, 13(30), 36388–36406.
- Didukh. (2018). 3d-electrons contribution to cohesive energy of 3d-metals. *Condensed Matter Physics*, 21(1), 13701.
- Dou, M., and Fyta, M. (2020). Lithium adsorption on 2D transition metal dichalcogenides: towards a descriptor for machine learned materials design. *Journal of Materials Chemistry A*, 8(44), 23511–23518.
- Friedel, J. (1954). Electronic structure of primary solid solutions in metals. *Advances in Physics*, 3(12), 446–507.
- Gao, S., Hao, J., Zhang, X., Li, L., Zhang, C., Wu, L., Ma, X., Lu, P., and Liu, G. (2021). Two dimension transition metal boride Y₂B₂ as a promising anode in Li-ion and Na-ion batteries. *Computational Materials Science*, 200, 110776.
- Gong, S., Wang, S., Zhu, T., Chen, X., Yang, Z., Buehler, M. J., Shao-Horn, Y., and Grossman, J. C. (2021). Screening and Understanding Li Adsorption on Two-Dimensional Metallic Materials by Learning Physics and Physics-Simplified Learning. *JACS Au*, 1(11), 1904–1914.
- Guo, Z., Zhou, J., and Sun, Z. (2017). New two-dimensional transition metal borides for Li ion batteries and electrocatalysis. *Journal of Materials Chemistry A*, 5(45), Article 45.
- He, Q., Li, Z., Xiao, W., Zhang, C., and Zhao, Y. (2021). Computational investigation of 2D 3d/4d hexagonal transition metal borides for metal-ion batteries. *Electrochimica Acta*, 384, 138404.
- Jensen, W. B. (1995). A Quantitative van Arkel Diagram. *Journal of Chemical Education*, 72(5), 395.

- Jia, J., Li, B., Duan, S., Cui, Z., and Gao, H. (2019). Monolayer MBenes: prediction of anode materials for high-performance lithium/sodium ion batteries. *Nanoscale*, *11*(42), Article 42.
- Jiang, Z., Wang, P., Jiang, X., and Zhao, J. (2018). MBene (MnB): a new type of 2D metallic ferromagnet with high Curie temperature. *Nanoscale Horizons*, *3*(3), Article 3.
- Jin, J., and Schwingenschlögl, U. (2022). Exploration of two-dimensional molybdenum-borides and potential applications. *Npj 2D Materials and Applications*, *6*(1), Article 1.
- Li, Y., Zhao, T., Li, L., Huang, R., and Wen, Y. (2022). Computational evaluation of ScB and TiB MBenes as promising anode materials for high-performance metal-ion batteries. *Physical Review Materials*, *6*(4), Article 4.
- Liu, Y., Wang, H., Fu, Y., Li, D., Wei, M., Wu, Q., and Hu, Q. (2023). Functionalized two-dimensional iron boride compounds as novel electrode materials in Li-ion batteries. *Physical Chemistry Chemical Physics*, *25*(34), 23133–23140.
- Ma, N., Wang, T., Li, N., Li, Y., and Fan, J. (2022). New phases of MBenes M₂B (M = Sc, Ti, and V) as high-capacity electrode materials for rechargeable magnesium ion batteries. *Applied Surface Science*, *571*, 151275.
- Ma, Z., Sun, F., Dou, M., Yao, Q., Liu, Y., and Wu, F. (2020). Are transition-metal borides promising for Na ion batteries? A first-principles study on transition-metal boride monolayer. *Physics Letters A*, *384*(14), Article 14.
- Persson, K., Sethuraman, V. A., Hardwick, L. J., Hinuma, Y., Meng, Y. S., van der Ven, A., Srinivasan, V., Kostecki, R., and Ceder, G. (2010). Lithium Diffusion in Graphitic Carbon. *The Journal of Physical Chemistry Letters*, *1*(8), 1176–1180.
- Sun, X., Liu, X., Yin, J., Yu, J., Li, Y., Hang, Y., Zhou, X., Yu, M., Li, J., Tai, G., and Guo, W. (2017). Two-Dimensional Boron Crystals: Structural Stability, Tunable Properties, Fabrications and Applications. *Advanced Functional Materials*, *27*(19), 1603300.
- Tang, Q., Zhou, Z., and Shen, P. (2012). Are MXenes Promising Anode Materials for Li Ion Batteries? Computational Studies on Electronic Properties and Li Storage Capability of Ti₃C₂ and Ti₃C₂X₂ (X = F, OH) Monolayer. *Journal of the American Chemical Society*, *134*(40), 16909–16916.

- Tomacruz, J. G. T., Castro, M. T., Remolona, M. F. M., Padama, A. A. B., and Ocon, J. D. (2025). Atomic Adsorption Energies Prediction on Bimetallic Transition Metal Surfaces Using an Interpretable Machine Learning-Accelerated Density Functional Theory Approach. *ChemistryOpen*, 14(4), e202400124.
- Wang, J., Ye, T.-N., Gong, Y., Wu, J., Miao, N., Tada, T., and Hosono, H. (2019). Discovery of hexagonal ternary phase Ti_2InB_2 and its evolution to layered boride TiB . *Nature Communications*, 10(1), 2284.
- Wang, Y., Wang, S., Song, N., Wu, X., Xu, J., Luo, S., Xu, B., and Wang, F. (2024). On two-dimensional metal borides (MBenes) as anode materials for metal-ion batteries: A first-principles study. *Computational Materials Science*, 233, 112710.
- Wei, F., Xu, S., Li, J., Yuan, S., Jia, B., Gao, S., Liu, G., and Lu, P. (2022). Computational Investigation of Two-Dimensional Vanadium Boride Compounds for Na-Ion Batteries. *ACS Omega*, 7(17), Article 17.
- Yuan, G., Bo, T., Qi, X., Liu, P.-F., Huang, Z., and Wang, B.-T. (2019). Monolayer Zr_2B_2 : A promising two-dimensional anode material for Li-ion batteries. *Applied Surface Science*, 480, 448–453.



CHAPTER V

CONCLUSIONS

This thesis presents a systematic computational screening of M_2B_2 MBene monolayers, where M represents any of the 26 transition metals and structures span four crystal phases: orthorhombic, hexagonal, trigonal, and tetragonal. The objective was to explore their potential as anode materials for Li-ion, Na-ion, Mg-ion, and Al-ion batteries using density functional theory. Interpretable machine learning models were employed to investigate structure–property relationships.

The intrinsic properties of M_2B_2 revealed an M-shaped cohesive energy trend across the d-block, consistent with that of pure transition metals. SHAP analysis identified the cohesive energy of M as the dominant factor, while phase-dependent variations were minor, influenced by local coordination and electronegativity. Dynamical stability, assessed via phonon dispersion, supported the cohesive energy trend. Density of states analysis showed that all M_2B_2 exhibit metallic character, enabling efficient electron transport.

The electrochemical properties of M_2B_2 were investigated through modeling of carrier adsorption and mobility. Layer-by-layer adsorption of carriers were explored up to three layers. First-layer adsorption is significantly stronger due to direct surface interaction, while the overall capacity is determined by whether subsequent layer adsorption energies fall below the stability threshold. Na is typically limited to one stable layer, whereas Al often achieves up to three.

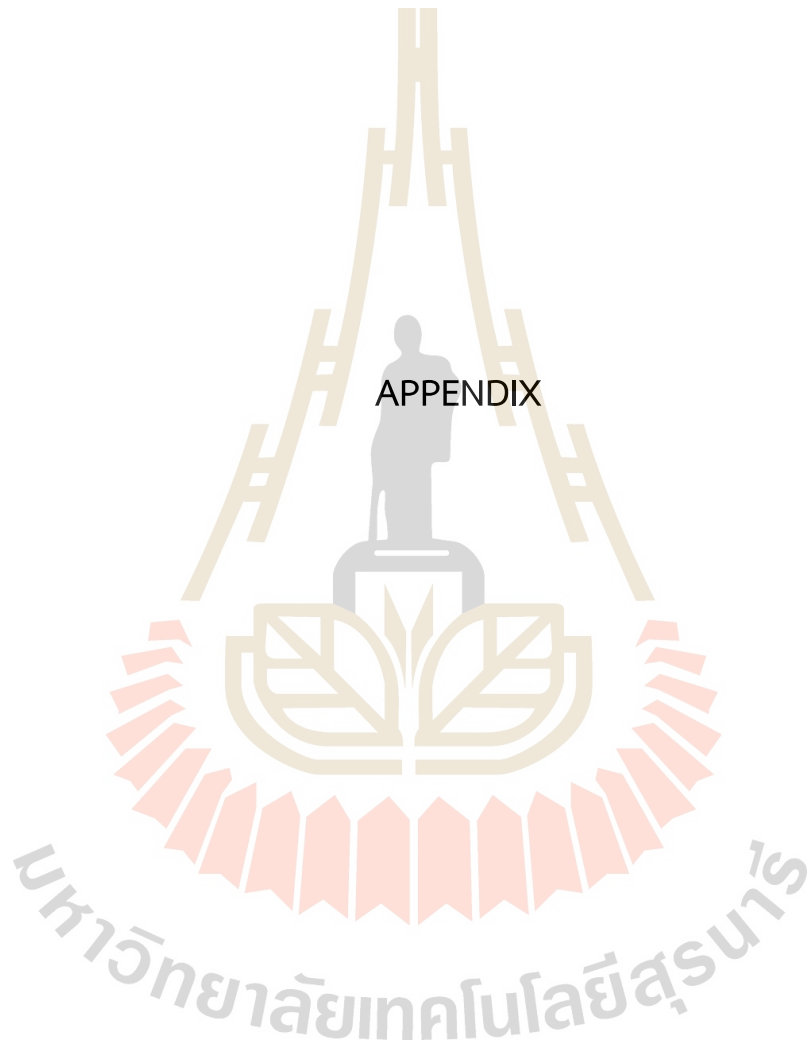
The open-circuit voltage (OCV) was calculated from first-layer adsorption energy normalized by carrier valency (z). An ML model trained on carrier and substrate features revealed three key factors influencing OCV: (1) carrier type, with z setting the trend $Li > Na > Mg > Al$; (2) crystal phase and lattice constant, affecting carrier–carrier spacing and lateral repulsion, particularly penalizing Na in compact trigonal phases; (3) the number of unpaired d-electrons, modulating M–carrier coupling strength; and (4) trigonal and tetragonal phases tend to yield lower OCVs.

Diffusion barrier trends showed that hexagonal, trigonal, and tetragonal phases generally exhibit lower barriers due to shorter hopping distances. In contrast, orthorhombic phases, influenced by local coordination and strong B–carrier interactions, often presented more constrained paths. Na consistently showed the lowest barriers due to weak surface binding, while Al exhibited the highest due to strong coupling.

From the constructed homogeneous dataset, we applied pre-screening based on cohesive energy, phonon stability, electronic conductivity, and diffusion barriers, which narrowed the candidates by half, retaining only those with structural stability and good transport properties. Further evaluation of electrochemical performance, specifically OCV and capacity, revealed two promising groups of anode materials. The first includes orthorhombic and hexagonal phases of Sc, Ti, and Y, which combine low OCVs with high capacities, particularly for Sc and Ti due to their low atomic mass. The second group consists of trigonal and tetragonal phases of V, Cr, Mn, and Fe, which, despite slightly lower capacities, exhibit low diffusion barriers suitable for fast-charging applications and occasionally moderate-to-low OCVs. Notably, Mn and Fe are cost-effective. Moreover, the structural phases in this group remain underexplored, offering opportunities for further study.

In conclusion, this thesis highlights the potential of M_2B_2 MBenes as anode materials for metal-ion batteries and presents a set of promising candidates with high capacity, suitable voltage, and favorable structural and transport properties. The integration of interpretable machine learning revealed key material–property relationships and important descriptors, providing rational guidelines for the design of high-performance anode materials.

APPENDIX



APPENDIX

PUBLICATION AND PRESENTATIONS

A.1 List of publications

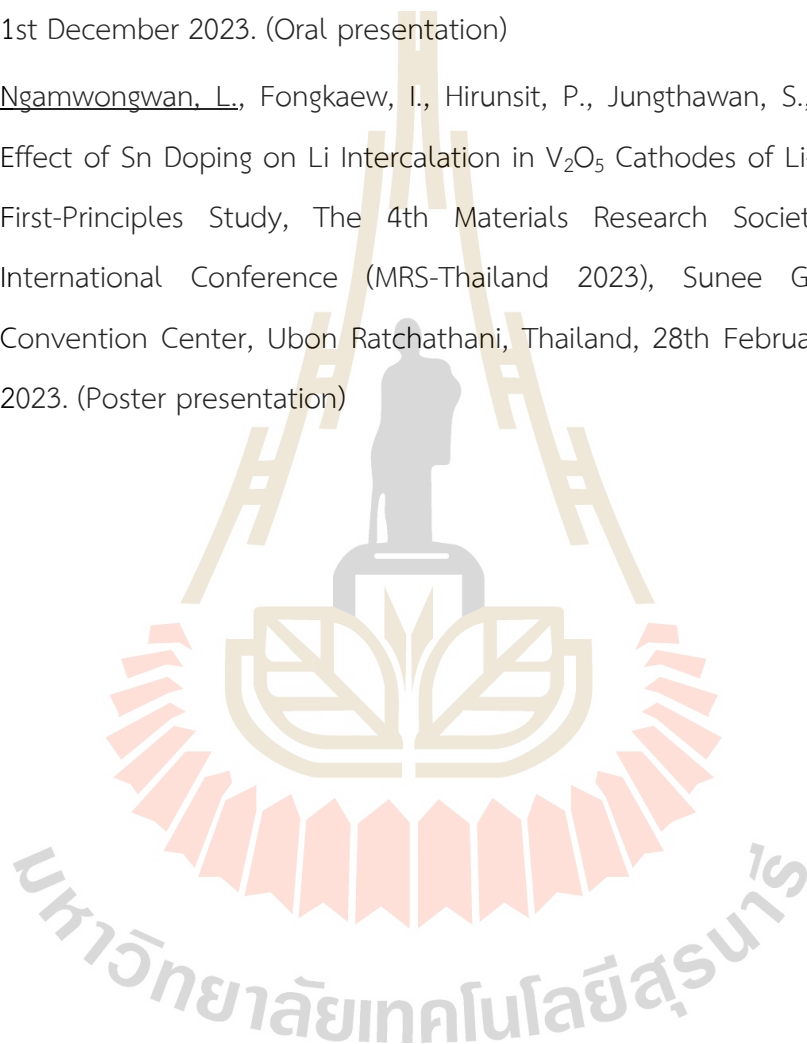
- Ngamwongwan, L.; Chotsawat, M.; Junkaew, A.; Artrith, N.; Fongkaew, I.; Suthirakun, S. Computational Screening of MBenes as Anode Materials of Metal-Ion Batteries. (*Manuscript in preparation*).
- Chotsawat, M., Ngamwongwan, L., Kaewraung, W., Untarabut, P., Jungthawan, S., Junkaew, A., Suthirakun, S. (2025). Tuning Hydrogen Adsorption in B_4CN_3 Monolayers: The Role of Metal Decoration and Vacancy Defects. *ACS Applied Materials & Interfaces*, 17(22), 32316–32328.
- Chotsawat, M., Ngamwongwan, L., Fongkaew, I., Junkaew, A., Suthirakun, S. (2025). Exploring Mo_2B MBene as a high-capacity anode material for multi-valent metal-ion batteries: Insights from first-principles calculations. *Colloids and Surfaces A: Physicochemical and Engineering Aspects*, 704, 135531.
- Chotsawat, M., Ngamwongwan, L., Falun, P., Jungthawan, S., Junkaew, A., Suthirakun, S. (2024). First-principles screening of metal-decorated biphenylene as efficient hydrogen storage materials. *International Journal of Hydrogen Energy*, 81, 573–581.
- Tharat, B., Ngamwongwan, L., Seehamongkol, T., Rungtaweeworanit, B., Nonkumwong, J., Nonkumwong, J., Suthirakun, S., Faungnawakij, K., Chanlek, N., Plucksacholatarn, A., Nimsaila, W., Prommin, C., Junkaew, A. (2024). Hydroxy and surface oxygen effects on 5-hydroxymethylfurfural oxidation to 2,5-furandicarboxylic acid on β - MnO_2 : DFT, microkinetic and experiment studies. *Nanoscale*, 16(2), 678–690.

- Falun, P., Ngamwongwan, L., Singesen, S., Chotsawat, M., Komen, P., Junkaew, A., Suthirakun, S. (2024). Enhancing V_2O_5 cathode performance through heterostructure engineering with the $Ti_3C_2O_2$ MXene: A computational study. *The Journal of Physical Chemistry C*, 128(26), 10774–10783.
- Untarabut, P., Singesen, S., Ngamwongwan, L., Fongkaew, I., Junkaew, A., Suthirakun, S. (2023). Unraveling the role of hydrogen insertion in enhancing the electrochemical performance of the V_2O_5 cathode for Mg-ion batteries: A first-principles study. *ACS Applied Energy Materials*, 6(17), 8666–8676.
- Ngamwongwan, L., Fongkaew, I., Phonsuksawang, P., Siritanon, T., Hirunsit, P., Jungthawan, S., Suthirakun, S. (2023). On the origin of ion intercalation and conductivity enhancement in Sn-doped V_2O_5 cathodes of Li-ion batteries: A computational study. *The Journal of Physical Chemistry C*, 127(24), 11526–11535.
- Singesen, S., Untarabut, P., Kaewraung, W., Ngamwongwan, L., Prasongkit, J., Suthirakun, S. (2024). Strain and external electric field engineering of S-terminated MXene on selective and sensitive detection of N-containing compound gases: A computational study. *Langmuir*, 40(43), 22693–22704.
- Singesen, S., Watwiangkham, A., Ngamwongwan, L., Fongkaew, I., Jungthawan, S., Suthirakun, S. (2023). Defect engineering of green phosphorene nanosheets for detecting volatile organic compounds: A computational approach. *ACS Applied Nano Materials*, 6(2), 1496–1506.
- Rodenburg, H. P., Mutschke, A., Ngamwongwan, L., Gulino, V., Kyriakou, V., Kunkel, N., Artrith, N., Ngene, P. (2023). Mixed hydride-electronic conductivity in Rb_2CaH_4 and Cs_2CaH_4 . *Solid State Ionics*, 403, 116384.
- Waehayee, A., Ngamwongwan, L., Kafizas, A., Chankhanittha, T., Butburee, T., Nakajima, H., Wannapaiboon, S., Pornsuwan, S., Suthirakun, S., Siritanon, T. (2025). Enhanced photocatalytic efficiency of Bi_2MoO_6 for water and p-nitroaniline reduction via iodate (I^{5+}) substitution: Implications of small polaron formation. *Chemical Engineering Journal*, 519, 165082.

- Waehayee, A., Phonsuksawang, P., Falun, P., Ngamwongwan, L., Choklap, T., Prachanat, J., Chankhanittha, T., Butburee, T., Suthirakun, S., Siritanon, T. (2024). Enhancing Z-scheme {001}/{110} junction in BiOCl with {110} surface oxygen vacancies for photocatalytic degradation of Rhodamine B and tetracycline. *Journal of Alloys and Compounds*, 997, 174915.
- Chankhunthod, N., Junploy, P., Suthirakun, S., Ngamwongwan, L., Phomma, C., Ruchusartsawat, R., Siyasukh, A., Yanu, P., Kijjanapanich, P., Yimklan, S., Rujiwatra, A., Brydson, R. D., Chimupala, Y. (2023). Ecofriendly alkali metal cations diffusion improves fabrication of mixed-phase titania polymorphs on fixed substrate by chemical vapor deposition (CVD) for photocatalytic applications. *Environmental Research*, 239, 117347.
- Jiamprasertboon, A., Sertwatsana, S., Ngamwongwan, L., Sangkhun, W., Waehayee, A., Phonsuksawang, P., Bootchanont, A., Nijpanich, S., Busayaporn, W., Nakajima, H., Suthirakun, S., Butburee, T., Siritanon, T. (2023). Controllable synthesis of nanostructured bismuth vanadate thin films as an efficient catalyst for photoelectrochemical water splitting. *New Journal of Chemistry*, 47(31), 14758–14767.
- Sailuam, W., Saisopa, T., Fongkaew, I., Ngamwongwan, L., Eknapakul, T., Seawsakul, K., Horprathum, M., Amonpattaratkit, A., Chanlek, N., Songsiriritthigul, P., Limpijumnong, S., Yimnirun, R., Jiamprasertboon, A., Bootchanont, A. (2023). Correlation of conductivity enhancement and Al-site defects in nanocolumnar ZnO films under vacuum annealing by experimental and calculations. *Applied Surface Science*, 613, 155985.

A.2 List of presentations

- Ngamwongwan, L., Chotsawat, M., Fongkaew, I., Junkaew, A., Suthirakun, S., A Systematic Investigation of MBene Anodes for Metal Ion Batteries: A First-Principles Study, The 8th International Conference on Nanotechnology – NanoThailand 2023, Dusit Thani Pattaya, Chonburi, Thailand, 29th November – 1st December 2023. (Oral presentation)
- Ngamwongwan, L., Fongkaew, I., Hirunsit, P., Jungthawan, S., Suthirakun, S., Effect of Sn Doping on Li Intercalation in V_2O_5 Cathodes of Li-ion Batteries: A First-Principles Study, The 4th Materials Research Society of Thailand International Conference (MRS-Thailand 2023), Sunee Grand Hotel & Convention Center, Ubon Ratchathani, Thailand, 28th February – 4th March 2023. (Poster presentation)



CURRICULUM VITAE

Lappawat Ngamwongwan was born on February 15, 1995, in Bangkok, Thailand. He received his Bachelor of Science in Physics (first-class honors with gold medal) in 2017 from the Department of Physics, Faculty of Science, Khon Kaen University. Since 2014, he has been awarded a scholarship from the Development and Promotion of Science and Technology Talents Project (DPST, Thailand). During his senior year, he began research in computational materials science, applying density functional theory (DFT) to investigate battery-related materials under the supervision of Asst. Prof. Dr. Thanayut Kaewmaraya and Assoc. Prof. Dr. Nonglak Meethong.

In 2018, he pursued a Master's degree at the School of Physics, Suranaree University of Technology, supported by the DPST scholarship. His research, supervised by Asst. Prof. Dr. Suwit Suthirakun and Assoc. Prof. Dr. Sirichok Jungthawan, focused on the theoretical modeling of energy materials using first-principles calculations.

Following his master's degree, he joined the Materials Chemistry and Catalysis group at the Debye Institute for Nanomaterials Science, Utrecht University, Netherlands, where he worked under the supervision of Asst. Prof. Dr. Nongnuch Artrith on the development of machine learning interatomic potentials trained from DFT data.

In 2022, he returned to the School of Physics at Suranaree University of Technology to begin his Ph.D. studies under the supervision of Assoc. Prof. Dr. Suwit Suthirakun, with co-advisors Asst. Prof. Dr. Ittipon Fongkaew and Asst. Prof. Dr. Nongnuch Artrith. His doctoral research focuses on the computational screening of MBenes as anode materials, combining density functional theory and interpretable machine learning approaches. He has contributed to several collaborative publications with both computational researchers and experimental collaborators and has participated in international conferences during the course of his doctoral studies.

His technical expertise centers on density functional theory calculations using the VASP package for advanced energy materials discovery.